論文 / 著書情報
Article / Book Information

題目(和文)	磁気的フラストレーションを有するクロムスピネル化合物およびパイロクロアチタン酸化物におけるスピン－格子結合に関する熱力学的研究
Title(English)	Thermodynamic Studies of Spin-Lattice Effects in Magnetically Frustrated Chromium Spinels and Titanium Pyrochlores
著者(和文)	気谷卓
Author(English)	Suguru Kitani
出典(和文)	学位:博士（理学）, 学位授与機関:東京工業大学, 報告番号:甲第9733号, 授与年月日:2015年3月26日, 学位の種別:課程博士, 審査員:川路　均,大坂　武男,菅野　了次,松下　伸広,平山　雅章
Citation(English)	Degree:, Conferring organization: Tokyo Institute of Technology, Report number:甲第9733号, Conferred date:2015/3/26, Degree Type:Course doctor, Examiner:,,,,
学位種別(和文)	博士論文
Type(English)	Doctoral Thesis

Doctoral Thesis

Thermodynamic Studies of Spin-Lattice Effects in Magnetically Frustrated Chromium Spinels and Titanium Pyrochlores

Suguru Kitani

Department of Electronic Chemistry,

Interdisciplinary Graduate School of Science and Engineering,

Tokyo Institute of Technology

2015

Supervisor Professor Hitoshi Kawaji

Contents

Chapter 1
Introduction

1.1 Magnetic Frustration

The term “frustration” generally refers to the state that it is impossible for all requirements to satisfy each other. The frustration often appears in our lives, as you would have experienced. Such frustrated state often induces unexpected situations to relieve a frustration. Similar states can, interestingly, be found in nature too. When a material includes a frustration, the ground state will not achieve a stable state. Instead, strong fluctuation emerges at low temperatures, and it is usually very sensitive for perturbations. The strong fluctuation and perturbations are coupled with one another, which creates an exotic ground state. Thus, the frustration in the material science have been attracted much attention as an excellent playground in which to discover new states and properties.

Magnetic materials are probably most typical and appropriate systems to study frustration effects. The most accessible example of the magnetic frustration is the antiferromagnetic Ising model, where the spins can orient up or down. It is worthwhile to start from considering the behavior of an *unfrustrated* case. Let the Ising spins with only the nearest neighbor exchange interaction J_1 arrange on the vertices of the square lattice, as illustrated in Fig. 1.1(a). In this situation, all spins can antiparallelly align without any problem. Then, consider the antiferromagnetic Ising spins on a triangular lattice as shown in Fig. 1.1(b). As opposed to the square lattice, spins cannot align antiparallel to each other, resulting in the frustration. It is called “Geometrical

frustration". The earliest theoretical study on the geometrical frustration was performed for two-dimensional triangular lattice by Wannier in 1950 [1]. and for pyrochlore lattice, three-dimensional frustrated system, by Anderson in 1956 [2]. They suggested that these spin systems show no phase transition down to the lowest temperature, and hence the ground state is macroscopically degenerated. In other words, the ground state of antiferromagnetic materials with such "frustratable" lattice is to be a spin-liquid state, in where spins strongly fluctuate without any transitions to long-range ordering.

And now, it is instructive to reconsider whether the square lattice model has a possible way to cause a magnetic frustration. Let the spins have an additional exchange interaction from next nearest neighbor (diagonal position) J_2 besides nearest-neighbor J_1, which is so-called the J_1-J_2 model as illustrated in Fig. 1.2. The ground state of this model depends on the ratio J_1/J_2. For $J_1 > 2J_2 > 0$, neighboring spins are antiparallel, resulting in ferromagnetic alignment of spins at the diagonal position. For $2J_2 > J_1 > 0$, spins are antiferromagnetically aligned with next nearest neighbors. These cases are weakly frustrated. On the other hand, for $J_1=2J_2$, the two states mentioned above are degenerated, leading to a strong frustration [3]. Such frustration from the competition between the exchange interactions is called "bond frustration".

The candidate materials for the spin-liquid state have been found in geometrically frustrated systems of two-dimensional triangular lattice [4], and kagome lattice [5], and three-dimensional hyper-kagome lattice [6], and pyrochlore lattice [7]. Recent studies have discovered geometrical frustration in cluster magnet [8], quasi-crystal [9], and organic materials [10], which attract much attention due to their characteristic properties that the conventional materials do not possess. In a system with the bond frustration, it has also been shown an exotic ground state as in the geometrically frustrated systems.

Besides the J_1-J_2 model, the bond frustration has been known to arise in the Plaquette lattice, checkerboard lattice, and Shastry-Sutherland lattice, which are based on the square lattice. Further, it has been discovered that the bond frustration is appeared in the spin-ladder system [11], diamond lattice [12], and honeycomb lattice [13], which exhibit spin-liquid-like state.

1.2 Magnetic Systems with Pyrochlore lattice

The name "pyrochlore lattice" originates from a characteristic lattice in the mineral pyrochlore, $(Na,Ca)_2Nb_2O_6(OH,F)$, the structure of which was first reported by von Gaertner in 1930 [14]. Figure 1.3 shows a pyrochlore lattice, which forms a corner-sharing tetrahedral network. As in the triangular lattice, if the magnetic moments are located on the vertices of each tetrahedron and exchange interaction between all moments are equal, strong geometrical frustration will emerge. This geometry is of theoretical and experimental interest.

In real compound, there are several crystal structures having a pyrochlore lattice. The representative is pyrochlore compounds $A_2B_2X_7$, where the *A* and *B* sites separately form the pyrochlore lattice as presented in Fig. 1.4. The *A*-sites are eight coordinated and located within distorted cubes, and the *B*-sites are six coordinated and are located within octahedron. The *A* and *B* ions are represented by metal cations and the *X* is mostly oxygen. It is known that the pyrochlore compound tolerates for the anion and cation vacancies. Hence, some defect pyrochlore can be present with the composition $A_2B_2X_6X_{1-x}$ ($0<x<1$) or AB_2X_6. The latter is recently referred as β-pyrochlore, getting attention due to the unconventional superconductivity induced by the rattling motion of the *A* ion [15].

Another typical compound which has the pyrochlore lattice is spinel AB_2X_4 shown in Fig. 1.4. The *B*-sites form the pyrochlore lattice, while the sub-lattice of the *A*-site is the diamond lattice, as opposed to the pyrochlore compounds. The *A*-sites are four coordinated and located within tetrahedron, and the *B*-sites are six coordinated and are located within octahedron. The *A* and *B* sites are occupied by metal cations and *X* is available to oxygen and chalcogen. Both pyrochlore and spinel belong to the cubic space group $Fd\text{-}3m$.

A lot of studies have been discovered the effect of magnetic frustration in these compounds. As discussed in the previous section, the pyrochlore lattice can lead to the spin-liquid state. However, most of them undergo a magnetic phase transition with a complex ordering or fall into a glassy state of spins. It is because the frustrated state is highly unstable, and the macroscopic degeneracy can be easily lifted by a weak perturbation, such as further exchange interaction, dipole-dipole interaction, site dilution, single-ion anisotropy, Dzyaloshinskii-Moriya interaction, quantum fluctuation, and spin-lattice coupling.

1.3 Spin-Lattice Coupling

In a pyrochlore antiferromagnet, the spin-lattice coupling often plays an important role for lifting the macroscopic degeneracy caused by the frustration. It means that the system is stabilized by distorting the lattice. However, there is, of course, a need to pay the cost of the elastic energy to distort the lattice. The simplest situation is the bond-phonon model [16], where the bond length in the pyrochlore lattice can independently expand or contract, and the energy gain through the spin-lattice coupling is proportional to the change of the bond length. From the elastic energy, this simple

model derives a biquadratic term in the spin Hamiltonian, which shows that the lattice distortion induced by the spin-lattice coupling always minimize the energy of the system.

The effect of the spin-lattice coupling has been observed in real systems. The most extensively studied materials are probably the chromium spinel oxides ACr_2O_4 (A=Zn, Cd, and Hg). Here $ZnCr_2O_4$ is illustrated as a representative [17]. In $ZnCr_2O_4$, magnetic Cr^{3+} ions form a pyrochlore lattice, and a strong antiferromagnetic interaction is present between them, indicating the negative Curie-Weiss temperature of -390 K. Hence, the strong frustration is induced. The paramagnetic phase remains well below the Curie-Weiss temperature. The system finally undergoes a magnetostructural transition from a cubic paramagnetic phase to a tetragonal antiferromagnetic phase with a complex spin order. As the cooperative phenomenon directly evokes the coupling between spin and lattice degrees of freedom, the theoretical model including the spin-lattice coupling was phenomenologically in good agreement with several experimental results related to the tetragonal distortion. It is noted that there is still no theory to simultaneously describe the observed lattice distortion and spin structure. To shed light on the microscopic mechanism, the any additional interactions have been considered to be required.

The idea of the spin-lattice coupling is further applied to the peculiar magnetization behavior at high magnetic fields of the chromium oxides [18]. When an external magnetic field is applied, they show a first-order transition following a half-magnetization plateau and lattice distortion. An interesting point is that despite the chromates have different ground states, their magnetic structures turn out to be the same under high magnetic fields, suggesting that a universal effect of the spin-lattice coupling

is lying on the chromium spinels.

Besides the magnetic frustration, there are several routes to establish the spin-lattice coupling. One of recent interest is the multiferroic material, because the spin-lattice coupling deeply relates with the mechanism of the multiferroicity. When spins form a spiral configuration, *i.e.*, symmetry lowering of spin system, the lattice symmetry is reduced through the inverse effect of the Dzyaloshinskii-Moriya interaction, resulting in an electric polarization [19]. In addition, recent theoretical development of the spin-lattice coupling has explained anomalous spin-glass behaviors observed in pyrochlore magnets [20]. The spin-glass transition temperature generally depends on the randomness. However, in the spinel oxide $ZnCr_2O_4$ and pyrochlore oxide $Y_2Mo_2O_7$, the element substation does not induce the change in the transition temperature, although the randomness must be changed. For this puzzling behavior, the Heisenberg model with assuming the coupling between spin and local lattice distortion provides a quantitative explanation. As described in this section, the spin-lattice coupling is now widely appeared in the material with novel physical properties.

1.4 Thermodynamic relations

In the study of the spin-lattice coupled system, heat capacity and thermal expansion measurements can be of crucial importance for considering the spin behavior in not only the macroscopic sense but also the microscopic sense. What makes it possible is that microscopic properties of a solid are thermodynamically related to the heat capacity and thermal expansion. Heat capacity at constant volume denoted as C_V is defined as the quantity of the internal energy E required to increase the temperature T of a unit quantity of a substance,

$$C_V = \left(\frac{\partial E}{\partial T}\right)_V. \tag{1.1}$$

Here E is related to the partition function Z of system, given as

$$E = kT^2 \left(\frac{\partial \ln Z}{\partial T}\right), \tag{1.2}$$

$$Z = \sum_i \exp\left(-\frac{E_i}{kT}\right), \tag{1.3}$$

where $\sum_i$ over all levels of the system, and E_i is an energy of the various possible levels originated from such as lattice vibrations, electric conduction, magnetic moment, and lattice disorder. If the energies individually depend on the respective characteristic energy scales, *i.e.*, $E_i = E_{\text{lat}} + E_{\text{elec}} + \cdots$, substituting Eq. (1.3) into Eq. (1.2) suggests that the internal energy is decomposed into several energy contributions, and hence the heat capacity too. Therefore, the appropriate subtraction of a certain contribution in the heat capacity from the measured heat capacity can provide the information of only the interested system.

Volumetric thermal expansion coefficient β is defined as

$$\beta = \frac{1}{V}\left(\frac{\partial V}{\partial T}\right)_P. \tag{1.4}$$

The corresponding quantity for changes in one direction is called as linear thermal expansion coefficient α written as

$$\alpha = \frac{1}{L}\left(\frac{\partial L}{\partial T}\right)_P, \tag{1.5}$$

where L is the length on a side. In the isotropic material, the relation $\beta = 3\alpha$ holds.

The microscopic theory for the thermal expansion of solid was established by Mie and Grüneisen [21], based on the consideration that the thermal expansion is induced by a volume dependence of the anharmonicity of the interatomic potential. This idea led to the particularly important finding that the ratio of the thermal expansion coefficient to

heat capacity is effectively constant as a function of temperature, so called "Grüneisen parameter γ". It is widely known as the following expression:

$$\gamma = \frac{\beta B_T V}{C_V} = -\frac{\partial \ln E^*}{\partial \ln V}, \quad (1.6)$$

where B_T is the isothermal compressibility, and E^* is the relevant energy scale. The original model in Grüneisen's work is based on Einstein model, where the crystal lattice has only the same vibrational frequency v. In this case, the characteristic energy scale is the Einstein temperature $\theta_E = hv/k$, and hence $\gamma = -\partial \ln v / \partial \ln V$. Similar discussion can be applied for any model with a single characteristic temperature, for example, electronic, magnetic, and other non-vibrational contributions. Because the total thermal expansion is small in most solids, the ratio is expected to vary only slightly with changing temperature. Thus, the whole behavior of the thermal expansion coefficient will generally mimic that of the heat capacity, and typically $\gamma \sim 1$. One of the notable exceptions is the case that the system exhibits negative thermal expansion. Unlike the isothermal compressibility and heat capacity, the thermal expansion coefficient can be either positive or negative. Equation (1.5) then results in the negative value for γ. Hence, an understanding of the origin of the negative Grüneisen parameter will contribute to clarify the mechanism of negative thermal expansion. As in this way, assessing the γ value often provides a useful insight on exotic properties.

Other important thermodynamic relations include information about the pressure dependence of the phase transition, which allow a discussion about the phase stability. Because of the difficulty in physical property measurements at low-temperature and high-pressure, the indirect way using the thermodynamic relation is convenient and rather accurate. The pressure effect for the first-order transition can be written as

$$\frac{dT_C}{dp} = \frac{\Delta V}{\Delta S}, \tag{1.8}$$

where T_C is the transition temperature, and ΔV and ΔS denote the change in volume and entropy at the transition. This relationship is called the Clausius-Clapeyron relation. On the other hand, the pressure effect for the second-order transition can be written as

$$\frac{dT_C}{dp} = T_C V_m \frac{\Delta \beta}{\Delta C_p}, \tag{1.9}$$

where V_m is the molar volume, and $\Delta\beta$=3$\Delta\alpha$ and ΔC_p are the jump in volume thermal expansion coefficient and heat capacity at T_C, respectively. Equation (1.9) is called the Ehrenfest equation. These relations enable us to obtain the pressure dependence of the transition temperature without applying pressure. Applying pressure is effectively equivalent to isotropic volume change. Thus, if the system has a strong coupling between lattice and other degrees of freedom, dT_c/dp will be a large value.

1.5 Outline of this thesis

The driving force of this doctoral study is to understand the lattice behavior in pyrochlore-based magnets with the strong spin-lattice coupling using heat capacity and thermal expansion measurements. Assuming the presence of the strong spin-lattice coupling, detailed study on the thermal expansion behavior should provide not only insights into lattice properties but also deeper understanding of spin properties as seen in the previous section. Most of frustrated compounds are extensively investigated through microscopic studies, *e.g.*, x-ray and neutron scattering experiments. On the other hand, the lattice has been assumed to be a passive bystander. I will demonstrate that the investigated systems, chromium spinels ACr_2X_4 (*A*=Cd, Co, and *X*=O, S) and titanium pyrochlores $R_2Ti_2O_7$ (*R*=Tb, Dy, and Ho), possess the characteristic thermal

expansion behavior originated definitely from their spin properties.

In chapter 2, the experimental background, basic knowledge and condition are described. For heat capacity measurements, the thermal relaxation method has mainly been employed, and the quasi-adiabatic method has been used for the low-temperature heat capacity of the terbium titanates, $Tb_2Ti_2O_7$. These two methods are suitable for the measurement at low-temperature and on a few milligram sample. For thermal expansion measurements, the capacitance method has been applied. Because of the surprisingly high relative resolution ($\Delta l/l \sim 10^{-10}$), which is the highest among the dilatometers, tiny lattice change can be detected. For magnetization measurements, a superconducting quantum interference device (SQUID) magnetometer from Quantum Design Inc. was used.

In chapter 3, spin-glass-like behavior in ferromagnetic spinel $CdCr_2S_4$ is presented. This compound has been considered to be a typical three-dimensional Heisenberg ferromagnet, and hence there is no frustration. However, recent studies show several interesting behaviors below the ferromagnetic transition temperature, such as multiferroicity, colossal magnetocapacitive effect, and negative thermal expansion. These observations suggest the need to reinvestigate the basic properties of the ferromagnetic phase. From the systematic thermodynamic investigation, the presence of the local lattice distortion will be indicated, and the relevant magnetic structure will be discussed.

In chapter 4, the spin-lattice coupling effect in strongly geometrically frustrated spinel $CdCr_2O_4$ is studied. This system is reminiscent of $ZnCr_2O_4$, as introduced in section 1.4. Due to the strong frustration arising from the antiferromagnetic interaction between Cr^{3+} spins, the system undergoes a magnetic transition with a structural

transition well below a Curie-Weiss temperature. Interestingly, a spin-liquid-like state with the low-energy excitations of antiferromagnetic hexagonal spin cluster was observed in the paramagnetic phase. This study will show the peculiar thermal expansion behavior induced by the spin behavior. In addition, a different transition behavior in $CdCr_2O_4$ and $ZnCr_2O_4$ will be considered through the pressure dependence of the transition temperature.

In chapter 5, the lattice behavior of the conical spin state in spinel oxide $CoCr_2O_4$ is investigated. In an early study on the spinel magnet, Lyons *et al.* theoretically suggested that any magnetic ground state of $CoCr_2O_4$ becomes unstable due to the frustration between Cr-Cr and Co-Cr exchange interactions. Indeed, a complex sequence of magnetic transitions is observed. Of particular interest is deserved on a conical spin state, where the multiferroicity is emerged. The multiferroic mechanism has been attributed to the inverse Dzyaloshinskii-Moriya interaction, where a spiral magnetic structure induces the reduction of lattice symmetry, resulting in polarization. Using thermodynamic relations, the stability of each phase, especially for the conical spin state expected to have strong spin-lattice coupling, will be investigated

In chapter 6, the role of the lattice in spin-liquid material $Tb_2Ti_2O_7$ is discussed. The magnetic Tb^{3+} ion has an antiferromagnetic interaction with a Curie-Weiss temperature Θ_{CW} = -19 K. However, $Tb_2Ti_2O_7$ does not show any conventional long-range order down to 20 mK. For clues about the lack of the phase transition, the low-lying first CEF excited state, which is separated by only 18 K from the ground state doublet, is considered to play an important role. Additionally, recent studies impose the presence of the spin-lattice effect, as indicated in several experiments. From the analysis of the heat capacity and thermal expansion coefficient, it will be shown that the thermal

expansion behavior can be explained by the lattice vibration and CEF excitation, and hence the spin liquid ground state might be established with little relation with a spin-lattice coupling.

In chapter 7, the lattice behavior related to the spin-ice state in $Dy_2Ti_2O_7$ and $Ho_2Ti_2O_7$ is studied. Due to the strong crystal-field anisotropy, the Dy^{3+} and Ho^{3+} ions behave as an Ising spin with the cubic <111> anisotropy. The effective interaction resulted from the balance between the nearest-neighbor exchange interaction and dipolar-dipolar interaction between spins is weak ferromagnetic, indicating a small positive Curie-Weiss temperature Θ_{CW} ~ 0.5 K and 1.9 K for $Dy_2Ti_2O_7$ and $Ho_2Ti_2O_7$, respectively. This situation induces highly frustrated ground states with “two-in two-out” spin configuration on each tetrahedron. Because the arrangement of spins is reminiscent of the proton positions in water ice, these compounds are called as spin ice. From thermal expansion measurements, an anomalous thermal expansion in $Dy_2Ti_2O_7$ and $Ho_2Ti_2O_7$ will be shown, and its relationship with a spin ice state will be argued.

Finally, in chapter 8, summary and concluding remarks will be presented.

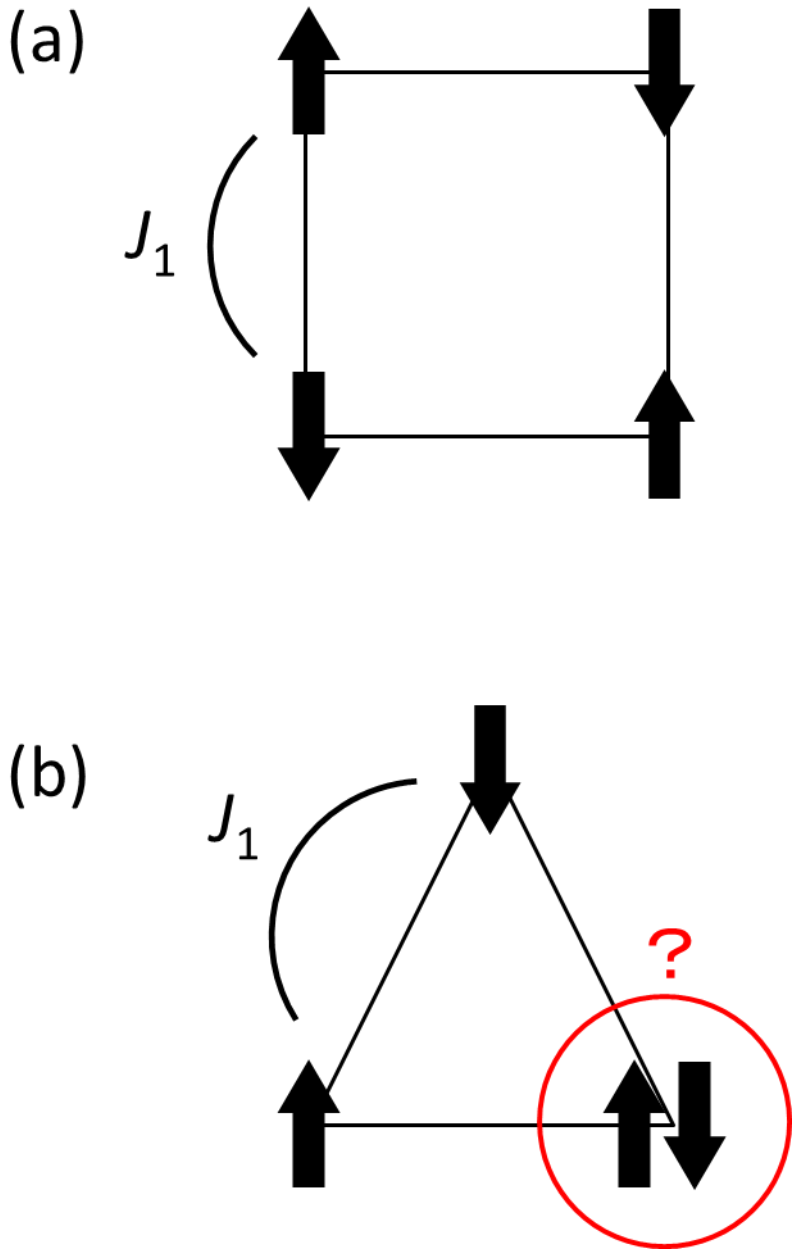

Fig. 1.1. (a) Antiferromagnetic Ising spins on the square lattice. No frustration occurs in this situation. (b) Antiferromagnetic Ising spins on the triangular lattice. Any one spin cannot take a stable orientation, resulting in the geometrical frustration.

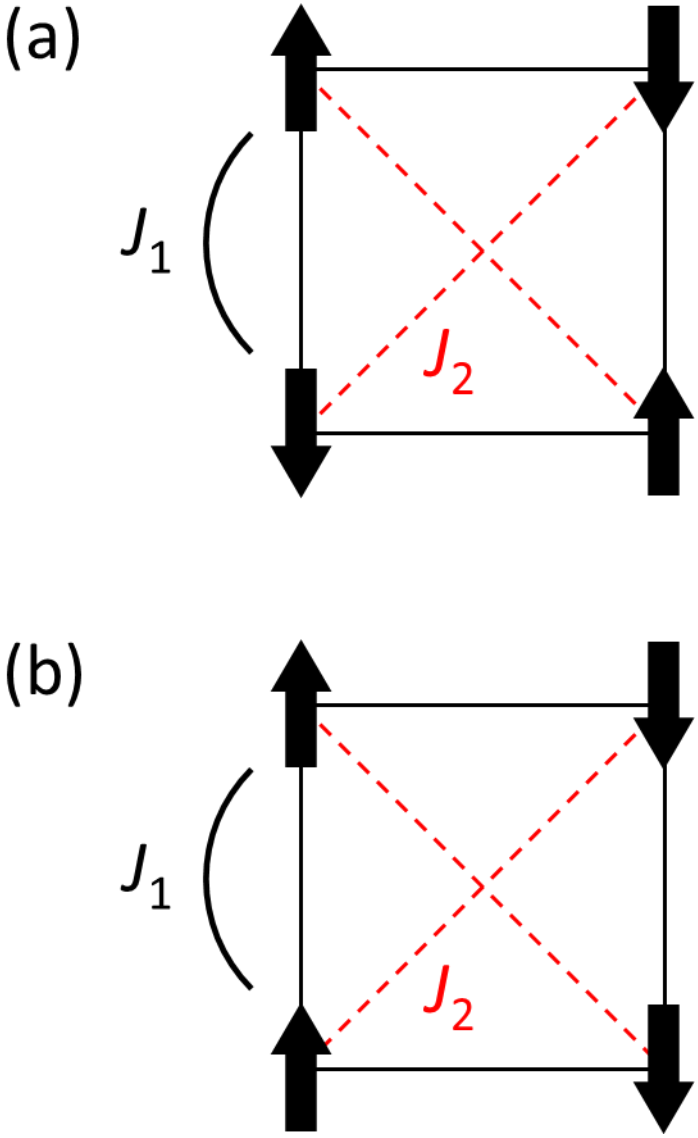

Fig. 1.2. J_1-J_2 model. (a) For $J_1 > 2J_2 > 0$. (b) For $2J_2 > J_1 > 0$.

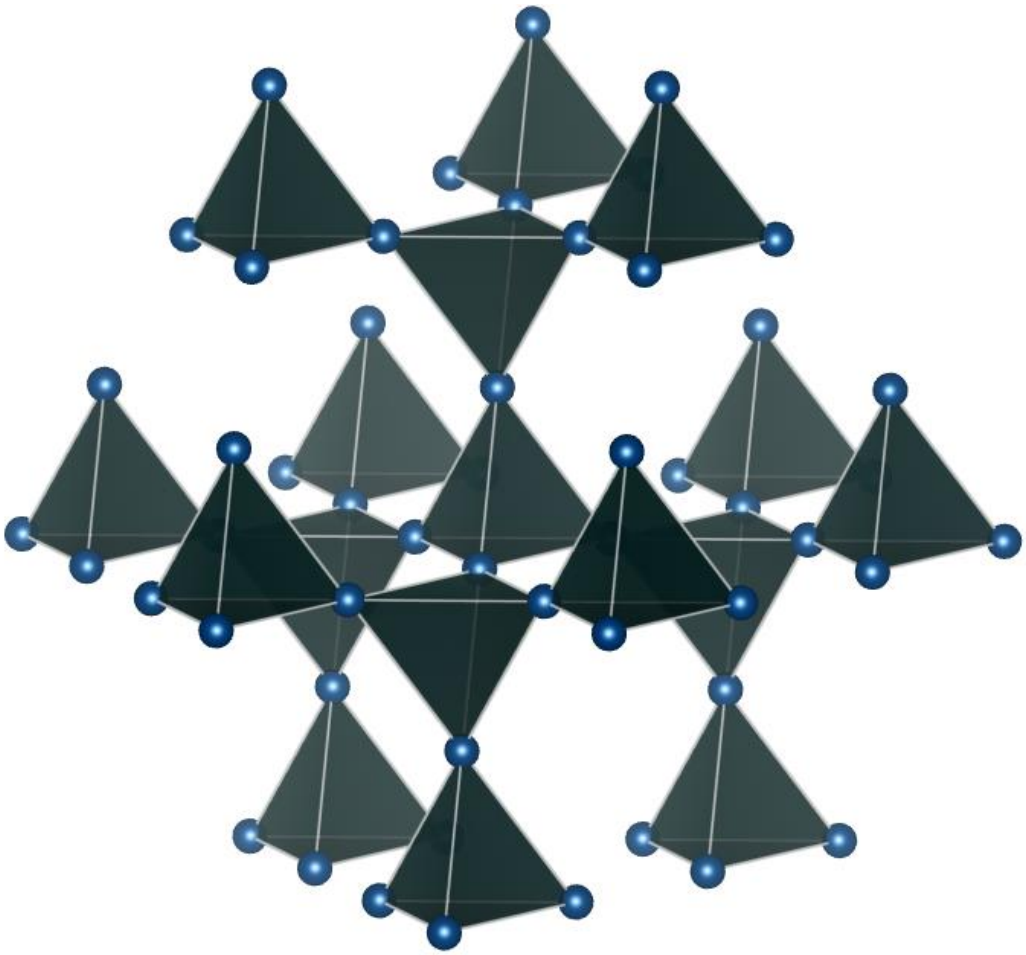

Fig. 1.3. Structure of pyrochlore lattice. The network of tetrahedral is formed.

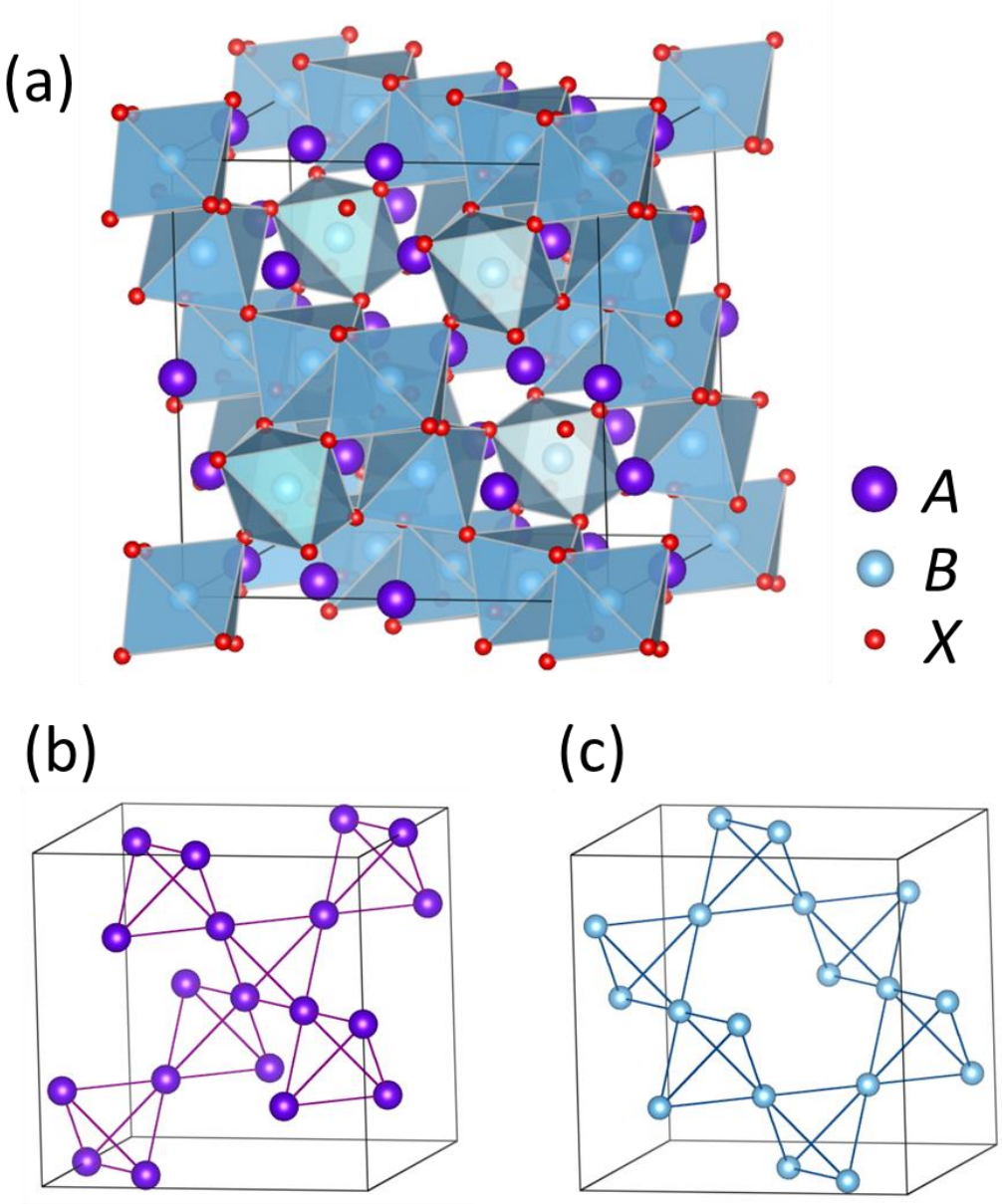

Fig. 1.4. (a) The structure of pyrochlore, where the *A*-sites are eight coordinated and located within distorted cubes, and the *B*-sites are six coordinated and are located within octahedron. (b), (c) The sub-lattice of the *A*-site and *B*-site, respectively. Both sub-lattices form the pyrochlore lattice.

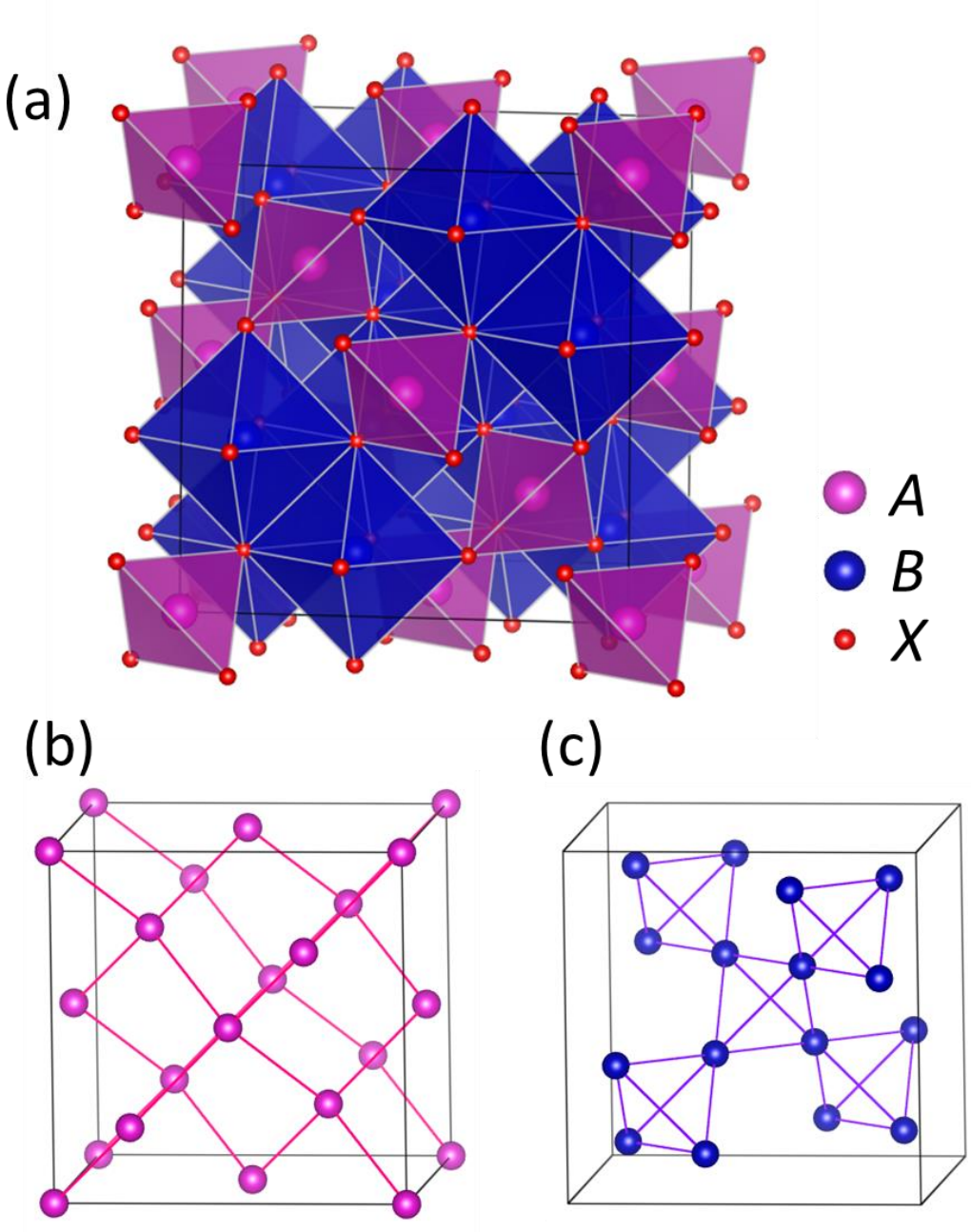

Fig. 1.5. (a) The structure of spinel, where the *A*-sites are four coordinated and located within tetrahedron, and the *B*-sites are six coordinated and are located within octahedron. (b) The sub-lattice of the *A*-site, forming the diamond lattice. (c) The sub-lattice of the *B*-site, forming the pyrochlore lattice.

References

[1] G. H. Wannier, Phys. Rev. **79**, 357 (1950).

[2] P. W. Anderson, Phys. Rev. **102**, 1008 (1956).

[3] P. Chandra, and B. Doucot, Phys. Rev. B **38**, 9335(R) (1988).

[4] S. Nakatsuji, Y. Nambu, H. Tonomura, O. Sakai, S. Jonas, C. Broholm, H. Tsunetsugu, Y. Qiu, and Y. Maeno, Science **309**, 1697 (2005).

[5] T.-H. Han, J. S. Helton, S. Chu, D. G. Nocera, J. A. Rodrigues-Rivera, C. Broholm, and Y. S. Lee, Nature (London) 492, 406 (2012).

[6] Y. Okamoto, M. Nohara, H. Aruga-Katori, and H. Takagi, Phys. Rev. Lett. **99**, 137207 (2007).

[7] J. S. Gardner, S. R. Dunsiger, B. D. Gaulin, M. J. P. Gingras, J. E. Greedan, R. F. Kiefl, M. D. Lumsden, W. A. MacFarlane, N. P. Raju, J. E. Sonier, I. Swainson, and Z. Tun, Phys. Rev. Lett. **82**, 1012 (1999).

[8] J. P. Sheckelton, J. R. Neilson, D. G. Soltan, and T. M. McQueen, Nature Mat. **11**, 493 (2012).

[9] E. Y. Vedmedenko , U. Grimm & R. Wiesendanger, Phil. Mag. **86**, 733 (2006).

[10] Y. Shimizu, K. Miyagawa, K. Kanoda, M. Maesato, and G. Saito, Phys. Rev. Lett. **91**, 107001 (2003).

[11] M. Azuma, Z. Hiroi, M. Takano, K. Ishida, and Y. Kitaoka, Phys. Rev. Lett. **73**, 3463 (1994).

[12] G. Chen, L. Balents, and A. P. Schnyder, Phys. Rev. Lett. 102, 096406 (2009).

[13] M. Matsuda, M. Azuma, M. Tokunaga, Y. Shimakawa, and N. Kumada, Phys. Rev. Lett. 105, 187201 (2010).

[14] H. R. von Gaertner, Neues Jahrb. Mineral., Monatsh., Beilage-Bd. Abt. A **61**, 1 (1930).

[15] S Yonezawa, Y Muraoka, Y Matsushita and Z Hiroi, J. Phys.: Cond. Mat. **16**, L9 (2004).

[16] *Introduction to Frustrated Magnetism*, edited by C. Lacroix, F. Mila, P. Mendels, Springer, Berlin (2010).

[17] S.-H. Lee, C. Broholm, T. H. Kim, W. Ratcliff, II, and S-W. Cheong, Phys. Rev. Lett. **84**, 3718 (2000).

[18] K. Penc, N. Shannon, H. Shiba, Phys. Rev. Lett. **93**, 197203 (2004).

[19] I. A. Sergienko and E. Dagotto, Phys. Rev. B **73**, 094434 (2006).

[20] H. Shinaoka, Y. Tomita, and Y. Motome, Phys. Rev. B **90**, 165119 (2014).

[21] G. Mie, Ann. Phys. **11**, 657 (1903); E. Grüneisen, Ann. Phys. **26**, 393 (1908); E. Grüneisen, Ann. Phys. **39**, 257 (1912).

[22] J. Snyder, J. S. Slusky, R. J. Cava and P. Schiffer, Nature (London) **413**, 48 (2001).

Chapter 2
Experimental

2.1 Heat capacity measurement

2.1.1 Introduction

In recent material study, one becomes to investigate a complex system due to its novel properties for fundamental study and also future application. As scientific developments, numerous types of physical property measurement method are innovated to investigate them. Especially, microscopic measurements, such as neutron, μSR, and NMR experiments, are considered to be the most powerful way. Nevertheless, heat capacity has been placed on the most important physical property that should be measured before performing other experiments. It is because heat capacity measurements are principally able to detect any internal energy change in the investigation system.

For heat capacity measurements, several methods have been developed. However, a suitable method is limited to some experimental conditions. In the study of novel materials, one can hardly obtain the large size and large amount sample. The problem on measuring a small sample is that the heat capacity of a measurement cell obscures that of the sample, resulting in low accuracy and precision. In addition, such sample usually shows interesting properties at low temperature, which makes the situation more complicated because the low-temperature measurements require a small experimental cell due to the space limitation in a refrigerator. To overcome these constraints, thermal

relaxation method is often used. In this study, heat capacity has measured mainly by the relaxation technique using a Quantum Design physical property measurement system (PPMS) for the temperature range from 2 to 300 K, and a homemade calorimeter with a ^{3}He/^{4}He dilution refrigerator (Kelvinox 300, Oxford Instruments plc.) for the temperature range below 2 K. In addition, quasi-adiabatic method with a ^{3}He/^{4}He dilution refrigerator was also attempted for low-temperature heat capacity measurements on the terbium titanate $Tb_2Ti_2O_7$.

2.1.2 Thermal relaxation method

Thermal relaxation method was established by Bachmann in 1972 [1]. It allows us to carry out heat capacity measurements on milligram order samples. Furthermore, the measuring apparatus of thermal relaxation method can be so small that it will be installed in most refrigerators with superconducting magnet. Despite these conveniences, one should beware that the thermal relaxation method cannot measure the heat capacity of a first-order phase transition with latent heat and a non-equilibrium system due to its measurement principle.

Here the measurement principle is introduced with using the schematic view of the measurement apparatus. The apparatus consists of the platform with thermometer and heater, and thermal link connecting the platform and the thermal bath. The temperature of the thermal bath is available for precise control. A measurement sample is attached on the platform with Apiezon N grease (M&I Materials Ltd.), which exhibits no craze down to very low temperatures. When the heater power applies to the platform and then turns off, the applied heat will leak to the thermal bath through the thermal link. The decaying of temperature, *i.e.*, thermal relaxation, provides the heat capacity of the

sample through a thermal equation. There are two methods for the analysis of a relaxation curve: 1τ method and 2τ method. The former assume only the relaxation process through the thermal link, which is able to analyze by a single exponential function. The latter takes into account of an extra relaxation process, so called 2τ effect, which originates from the non-negligible heat capacity of components, the poor thermal conductance between the sample and the platform, and so on. If there is no 2τ effect, both analysis leads to the same result. The followings provide the mathematical way to calculate the heat capacity by each method.

2.1.2.1 1τ method

1τ method is based on the following assumptions; i) The heat capacity of a thermal link can be ignored compared to the heat capacity of a sample. ii) Thermal conductivity and heat capacity keep a constant in a measurement. iii) The thermal conductivity between a sample and platform is sufficiently larger than that of a thermal link. iv) The heat leak from a sample is only a thermal link. A toy model of the measurement cell including these assumptions is depicted in Fig. 2.1(a), where the sample with a heat capacity C is attached onto the platform, connecting to the thermal bath with a fixed temperature T_0 by the thermal link with a weak thermal conductivity κ. Figure 2.2 shows the time dependence of a power P and a sample temperature T when a pulse electrical power P is applied to the heater.

A part of a heat generated by P increases the internal energy of the system, and another part flows into the thermal bath through the thermal link. The heat flow can be written as

$$P = \int_{T_0}^{T} \kappa(T')dT' + C\frac{dT}{dt}, \quad (2.1.1)$$

where T is the sample temperature and t is the elapsed time. When the power is continuously applied, the system reaches to a steady state, resulting in zero of the second term in Eq. (2.1.1). The three assumptions that the sample temperature in the steady state is T_1, the temperature difference between T_1 and T_0 is negligible, and the temperature dependence of the C and κ undergoes very little change should be held. Then, the integration of the first term in Eq. (2.1.1) can be replaced by a thermal conductivity κ_{av}. And the P is readily derived as

$$P = \kappa_{\mathrm{av}} \times \Delta T, \quad (2.1.2)$$

where ΔT denotes $T_1 - T_0$.

As the next step, the heater power is turned off. This procedure brings about a decrease in the temperature from T_1 to T_0, which goes on as the red line in the Fig. 2.2. The definite integration from t=0 to the arbitrary point in Eq. (2.1.1) with P=0 and T=T_1 leads to

$$T(t) - T_0 = \Delta T \exp(-\kappa_{\mathrm{av}} t/C). \quad (2.1.3)$$

An exponential decay is generally given as a form exp(-t/τ), where τ is a relaxation time constant. Hence, by defining

$$\tau = C/\kappa_{\mathrm{av}}, \quad (2.1.4)$$

Eq. (2.3) becomes

$$T(t) - T_0 = \Delta T \exp(-t/\tau). \quad (2.1.5)$$

The slope of the single logarithm plot of Eq. (2.1.5) leads to a characteristic relaxation time constant. Therefore, by determining the thermal conductivity κ_{av} and the relaxation time τ from Eqs. (2.1.2) and (2.1.5), we can yield the heat capacity from Eq. (2.1.4). This is 1τ method. It is widely used for the case that the sample and platform have a

good thermal conductivity and no heat gradient. The following section describes 2τ method, which should be employed if a relaxation curve cannot be analyzed by a single exponential function, that is, if there is 2τ effect.

2.1.2.2 2τ method

As mentioned above, 2τ method analyzes a relaxation curve with taking into account the second τ, which is explained by the model illustrated in Fig. 2.1(b). This method allows the presence of a thermal link with a thermal conductivity κ_a between a sample with a heat capacity C_a and a platform with a heat capacity C_b. The time dependence of a sample temperature T will be similar with that of 1τ method before turning off the heater, as shown in Fig. 2.2. The relaxation process, however, is significantly different from 1τ method. The temperature decreases rapidly, followed by a slow decay, which is depicted as the blue dashed line in the Fig. 2.2. The thermal equation for the sample is given as

$$C_a \frac{dT_a}{dt} = -\kappa_a(T_a - T_b), \tag{2.1.6}$$

and for the platform as

$$C_b \frac{dT_b}{dt} = -\kappa_a(T_b - T_a) - \kappa_b(T_a - T_0), \tag{2.1.7}$$

where T_a is the temperature of the sample, T_b is the temperature of the platform, κ_a is the thermal conductivity between the sample and platform, and κ_b is the thermal conductivity between the platform and thermal bath. Here the temperature dependence of C_a, C_b, κ_a, and κ_b is regarded as vanishingly small. Using the following equations

$$\tau_a \equiv C_a/\kappa_a, \quad \tau_b \equiv C_b/\kappa_b, \tau \equiv (C_a + C_b)/\kappa_b, \tag{2.1.8}$$

$$\tau_1 = \left(\frac{\tau+\tau_a}{2}\right)\left(1 + \sqrt{1 - \frac{4\tau_a\tau_b}{(\tau+\tau_a)^2}}\right), \tag{2.2.9}$$

$$\tau_2 = \left(\frac{\tau+\tau_\mathrm{b}}{2}\right)\left(1+\sqrt{1-\frac{4\tau_\mathrm{a}\tau_\mathrm{b}}{(\tau+\tau_\mathrm{b})^2}}\right), \tag{2.1.10}$$

the Eqs. (2.1.6) and (2.1.7) is solved, and then the relaxation curve is obtained as

$$T_b(t) - T_0 = \left(\frac{P_0}{\kappa_b}\right)\left[\left(\frac{\tau-\tau_2}{\tau_1-\tau_2}\right)\exp\left(-\frac{t}{\tau_1}\right) + \left(\frac{\tau_1-\tau}{\tau_1-\tau_2}\right)\exp\left(-\frac{t}{\tau_2}\right)\right]. \tag{2.1.11}$$

By replacing

$$A_1 = \left(\frac{P_0}{\kappa_b}\right)\left(\frac{\tau-\tau_2}{\tau_1-\tau_2}\right),\ \ A_2 = \left(\frac{P_0}{\kappa_b}\right)\left(\frac{\tau_1-\tau}{\tau_1-\tau_2}\right),\ \ A_1 + A_2 = \Delta T\,, \tag{2.1.12}$$

we obtain

$$C_\mathrm{a} + C_\mathrm{b} = \kappa_\mathrm{b}\left(\frac{A_1\tau_1+A_2\tau_2}{A_1+A_2}\right). \tag{2.1.13}$$

In addition, Eqs. (2.1.9), (2.1.10), and (2.1.12) derives

$$A_1 + A_2 = P_0/\kappa_\mathrm{b} = \Delta T, \tag{2.1.14}$$

Substituting Eq. (2.1.14) into Eq. (2.1.13) will result in

$$\frac{C_\mathrm{a}+C_\mathrm{b}}{\kappa_\mathrm{b}} = \frac{A_1\tau_1}{A_1+A_2}\left(1+\frac{A_2\tau_2}{A_1+A_2}\right) \backsimeq \frac{A_1\tau_1}{\Delta T}. \tag{2.1.15}$$

If the platform heat capacity C_b has already known by the preliminarily measurements of the heat capacity without mounting a sample, we can yield A_1 and τ_1 from the non-linear fitting to the relaxation curve, leading to the sample heat capacity C_a. Practically, 2τ analysis is the most commonly used.

2.1.3 Quasi-adiabatic method

Quasi-adiabatic, also referred as semi-adiabatic or isoperibol, method is similar to the adiabatic method [2], which is the most basic method for heat capacity measurements. The definition of the heat capacity of

$$C = \lim_{\Delta T\to 0}\frac{\Delta Q}{\Delta T} \tag{2.1.16}$$

means that under the adiabatic condition the heat capacity is obtained by measuring an

increase in the sample temperature ΔT, caused by a supplied heat ΔQ. Adiabatic method is based on this principle, and it can provide the heat capacity with the highest accuracy. On the other hand, quasi-adiabatic method allows the sample to exchange a heat with surroundings, though a smaller heat exchange is absolutely favorable.

In order to consider a change of the sample temperature with applying a heat, it is better to start from introducing the schematic model presented in Fig. 2.1(b), which is the same setup as used in the thermal relaxation method with 2τ effect. A sample with a heat capacity C_a is attached onto the platform with a thermal conductivity κ_a, and a platform with a heat capacity C_b is connected to the thermal bath with a temperature T_0 by the thermal link with a weak thermal conductivity κ_b. In comparing with 2τ method, the difference is that the temperature of the thermal bath does not need to be fixed. Hence one measurement cell can take a different method depending on the measurement condition and purpose. The model assumes that the thermal conductivity between the sample and platform is much larger than that between the platform and thermal bath, $\kappa_a >> \kappa_b$. When a pulse of electrical power P is applied to the heater, the sample temperature T will change as Fig. 2.3. Just after turning off the heater power, the sample temperature can be considered to relax with a linear temperature dependence when $\kappa_a >> \kappa_b$. Thus, the extrapolation of the temperature before and after heating to the midpoint of the heating period establishes ΔT for the measurement. Substituting the ΔT and the applied power ΔQ into Eq. (2.1.16), the heat capacity of the sample can be obtained. The great advantage of quasi-adiabatic method is shortening the measurement time because it can perform heat capacity measurements with changing temperature. By constructing the measurement cell with an appropriate condition and the measurement system with FPGA hardware, the measurement time can be further shortened. These

attempts result in that a single point measurement only needs several hundred milliseconds, which should be compared with that of relaxation method of tens of seconds. The short measurement time enables the heat capacity measurement with sweeping temperature. Thus, heat capacity measurements for wide temperature range can be accomplished by a significantly short time.

2.2 Thermal expansion measurement

2.2.1 Introduction

Thermal expansion measurement (dilatometry) is the measurement of the change in the sample length with varying temperature. The close relationship between thermal expansion and heat capacity suggests that the thermal expansion also relates to the internal energy of a system. Thus, the knowledge of the thermal expansion is obviously important for the study on solid state physics as well as that of heat capacity. It will provide not only lattice property but also other information, such as electronic, magnetic, and even nuclear properties. Furthermore, the combination of thermal expansion and heat capacity can characterize the phase transition through Clausius-Clapeyron relation or Ehrenfest equation, leading to fruitful insights on the many intriguing states originated found in novel materials.

The measurement method of thermal expansion can be categorized into the absolute measurement that directly measure a sample length (or its correspondent), and relative measurement that utilize a reference material. Typical examples for absolute expansion measurement are optical interferometric method, x-ray diffraction method,

telemicroscope method, and light scan method. Relative expansion measurement is represented by push-rod method, strain gauge method, thermo-mechanical analysis, and capacitance method. Each dilatometry has its own benefits and drawbacks, and hence one should take an appropriate way depending on the investigation sample and conditions. For the crystalline sample, x-ray diffraction method is the most common way to obtain the thermal expansion. This method, however, has a difficulty in investigating the detailed temperature dependence of the thermal expansion due to the inability to measure with temperature scanning and its relative sensitivity of $\Delta L/L \sim 10^{-7}$. The problem results in the insufficient information to a minute lattice change in a narrow temperature range, especially for the phase transition.

In contrast, capacitance method can offer very high relative sensitivity of $\Delta L/L \sim 10^{-10}$, which is a few orders of magnitude better than the sensitivity of not only x-ray method but of all other methods. Despite its outstanding performance, some experimental difficulties had turned away the researchers. The earliest capacitance dilatometer with parallel plates, reported by White in 1961 [3], has the disadvantage on the big size of the dilatometer, which was required to achieve a high resolution. Such big size cell usually mismatch for the limited space in the most of cryostats with magnet coil. In addition, thermal gradient in the cell also becomes a critical problem. A lot of efforts have been devoted to solve these problems with improving its sensitivity. However, there is another problem on sample handling. The parallel-type capacitance dilatometer needs a sample with strictly parallel surfaces.

The capacitance dilatometer used in this thesis research is designed by Rotter *et al*. [4], which is based on the tilted plate principle. This system allows us to use nearly any irregular shape of samples; only the base surface should be flat to give a stable sample

position. And of course, it has most advantages of the existing capacitive dilatometers, avoiding their disadvantages.

2.2.2 Capacitance method

Capacitance method detects a change of a sample length as a change in the gap between a pair of capacitor plates. For an ideal parallel-plate capacitor in vacuum, capacitance C stored between capacitor plates depends on the gap d between and the area A of the capacitor plates:

$$C = \frac{\varepsilon_0 A}{d} \tag{2.2.1}$$

where ε is the permittivity. When a sample is placed between the capacitor plates, varying temperature gives rise to a capacitance change due to thermal expansion. In other words, the measurement of a capacitance change using capacitor plates with a known area leads to the thermal expansion of a sample. This is the basic principle of capacitance dilatometer.

In the case of the tilted capacitance dilatometer, the situation turns to be a complex problem. Before moving onto the derivation of the thermal expansion, it is helpful to confirm the tilted plate construction made of silver. The schematic view of the cross section of the measurement cell is presented in Fig. 2.4. The cell consists mainly of two parts: the lower part, composed by the plate holder and the capacitor plate, which in the center has a depression to hold a sapphire slice used for the sample mounting space, and the upper part, composed by the plate holder and the capacitor plate, which has a center hole to house the sample. They are separated by two needle bearings. Both capacitor

plates as well as the sample place are strictly insulated from the holders. The detailed drawing of the tilted plate capacitance dilatometer is found in Fig. 2 of Ref. [4].

The followings show how to obtain the thermal expansion coefficient from the capacitance measurement [5]. For this tilted dilatometers, the gap $d(T)$ is numerically calculated by

$$C(T) = \frac{2\varepsilon_0}{d(T)}\left[A_{\mathrm{o}}(T)\frac{1-\sqrt{1-\gamma_{\mathrm{o}}^2}}{\gamma_{\mathrm{o}}^2} - A_{\mathrm{i}}(T)\frac{1-\sqrt{1-\gamma_{\mathrm{i}}^2}}{\gamma_{\mathrm{i}}^2}\right], \tag{2.2.2}$$

where ε_0 is the vacuum permittivity, $C(T)$ is the capacitance, A_{o} and A_{i} are the area of the outer and inner capacitor plate, and γ is the quantity determined by the angle of the tilted plates. γ_{o} and γ_{i} given as

$$\gamma_{\mathrm{o}} = \frac{r_{\mathrm{o}}}{b}\left[\frac{k(T)}{d(T)} - 1\right],\ \gamma_{\mathrm{i}} = \frac{r_{\mathrm{i}}}{b}\left[\frac{k(T)}{d(T)} - 1\right], \tag{2.2.3}$$

where r_{o} is the outer plate radius, r_{i} is the inner plate radius, and b is the distance between center of capacitor plate and pivot, which are the characteristic constants of the apparatus. $k(T)$ is height of the cone bearing, which is defined as

$$k(T) = k(T_0) + 2d_S\left[\frac{\Delta l_{\mathrm{Ag-Lit}}}{l}(T) - \frac{\Delta l_{\mathrm{Sapphire-Lit}}}{l}(T)\right], \tag{2.2.4}$$

where $k(T_0)$ is height of the cone bearing as T_0=300 K determined from the corresponding capacitance C_0 keeping the capacitor plates parallel, d_S is the thickness of sapphire washers (0.8 mm), $(\Delta l_{\mathrm{Ag\text{-}Lit}}/l)(T)$ is the thermal expansion of Ag from literature, and $(\Delta l_{\mathrm{Sapphire\text{-}Lit}}/l)(T)$ is the thermal expansion of sapphire from literature. The temperature dependence of the inner plate $A_i = \pi r_i^2$ is given by

$$A_{\mathrm{i}}(T) = A_{\mathrm{i}}(T_0)\left[1 + \frac{\Delta l_{\mathrm{Ag-Lit}}}{l}(T)\right]^2, \tag{2.2.5}$$

and similarly that of the outer plate $A_i = \pi r_i^2$ is given by

$$A_{\mathrm{o}}(T) = A_{\mathrm{o}}(T_0)\left[1 + \frac{\Delta l_{\mathrm{Ag-Lit}}}{l}(T)\right]^2, \tag{2.2.6}$$

where $A_i(T_0)$ and $A_o(T_0)$ are the initial areas calculated from the apparatus constants. Because $d(T)$ is included in $C(T)$ [Eq. (2.2.2)] and γ_o and γ_i [Eq. (2.2.3)], it requires a numerical solution. In order to eliminate all influences of the expansion of silver, Mehboob has modified the above equations by considering the schematic geometry of the measurement cell [5]; the gap $d(T)$ and the area of inner and outer capacitor plates $A_o(T)$ and $A_i(T)$ are normalized as $\hat{d}(T), \hat{A}_o(T),$ and $\hat{A}_i(T)$:

$$\hat{d}(T) \equiv \frac{d(T)}{1+\frac{\Delta l_{\mathrm{Ag-Lit}}}{l}(T)} \tag{2.2.7a}$$

implying $d(T) \equiv \hat{d}(T)\left[1+\frac{\Delta l_{\mathrm{Ag-Lit}}}{l}(T)\right]$.

$$\hat{A}_{\mathrm{o}}(T) \equiv \frac{A_{\mathrm{o}}(T)}{1+\frac{\Delta l_{\mathrm{Ag-Lit}}}{l}(T)} = A_{\mathrm{o}}(T_0)\left[1+\frac{\Delta l_{\mathrm{Ag-Lit}}}{l}(T)\right], \tag{2.2.7b}$$

$$\hat{A}_{\mathrm{i}}(T) \equiv \frac{A_{\mathrm{i}}(T)}{1+\frac{\Delta l_{\mathrm{Ag-Lit}}}{l}(T)} = A_{\mathrm{i}}(T_0)\left[1+\frac{\Delta l_{\mathrm{Ag-Lit}}}{l}(T)\right]. \tag{2.2.7b}$$

Using these new definitions, the thermal expansion the sample is obtained as

$$\frac{\Delta l_{\mathrm{Sample}}}{l}(T) = \frac{\Delta \hat{d}_S(T)}{l_{\mathrm{S}}}\left[1+\frac{\Delta l_{\mathrm{Ag-lit}}}{l}(T)\right] + \frac{\Delta l_{\mathrm{Ag-Lit}}}{l}(T), \tag{2.2.8}$$

where $\Delta \hat{d}_S(T) \equiv \hat{d}(T) - \hat{d}(T_0)$.

If a piece of silver is used as a sample, the thermal expansion obtained must agree with literature data, that is,

$$\frac{\Delta l_{\mathrm{Sample}}}{l}(T) = \frac{\Delta l_{\mathrm{Ag-Lit}}}{l}(T). \tag{2.2.9}$$

Accordingly, Eq. (2.2.13) get converted to

$$\Delta \hat{d}_S(T) = 0, \tag{2.2.10}$$

indicating that the gap between the capacitor plates exhibits no temperature dependence. However, in reality, Eq. (2.2.10) does not hold true. Due to mainly the imperfection and purity of the silver, Ag sample and Ag capacitance plates do not expand or contract with same ratio. Therefore, the resulting change of the gap is not zero. In order to

compensate for these effects, the zero signal should be subtracted from the sample signal through the calculation. Adding the correction term change Eq. (2.2.8) to

$$\frac{\Delta l_{\mathrm{Sample}}}{l}(T) = \left[\frac{\Delta \hat{d}_{\mathrm{Sample}}}{l_{\mathrm{S}}}(T) - \frac{\Delta \hat{d}_{\mathrm{Ag-Sample}}}{l_{\mathrm{S}}}(T)\right]\left[1 + \frac{\Delta l_{\mathrm{Ag-lit}}}{l}(T)\right] + \frac{\Delta l_{\mathrm{Ag-Lit}}}{l}(T), \tag{2.2.11}$$

where $\Delta\hat{d} = \hat{d}(T) - \hat{d}(T_0)$, $\Delta\hat{d}_{\mathrm{Sample}}(T)$ is the measurement of the sample, and $\Delta\hat{d}_{\mathrm{Ag-Sample}}(T)$ is the measurement of an Ag for reference (calibration sample). The pure value of the thermal expansion of the sample is eventually obtained as the left side of Eq. (2.2.11).The thermal expansion coefficient of the sample can then be calculated by differentiating $\Delta l_{\mathrm{Sample}}/l\,(T)$. In other words, the thermal expansivity is divided by the difference between a certain measurement temperature and its next temperature.

In this study, the temperature control has been performed by PPMS as cryostat, the sample temperature has been measured by Cernox resistance thermometer (Model:CX-1050-SD-HT-1.4M, Lake Shore Cryotronics, Inc.) with the resistance bridge (Model 340, Lake Shore Inc.), and the capacitance has been measured by the capacitance bridge (Model 2500A 1 kHz Ultraprecision Capacity Bridge, Andeen-Hagerling, Inc.). The measurement is automatically controlled by Labview program. In a lot of cases, the direct differentiating of the measured thermal expansivity leads to highly scattered thermal expansion coefficient. Hence, the thermal expansivity is smoothed by a Savitzky-Golay filter [6], and then differentiating. The results have been compared with those of point-by-point differentiation to confirm whether the sharp features of the transitions were fully retained through the smoothing.

2.3 Magnetic Measurements

Magnetic measurements are explicitly important for the magnetic materials to investigate their macroscopic magnetic property. The analysis of the magnetic susceptibility can provide the strength of the spin interaction and the effective moment of the component spins through the Curie-Weiss law. Furthermore, *ac* susceptibility measurements, in which an *ac* magnetic field is applied to a sample, provides valuable information about magnetization dynamics, which cannot be obtained in *dc* measurements.

In this study, magnetic measurements have been carried out by a Quantum Design magnetic property measurement system (MPMS-5S), using SQUID magnetometer. SQUID are based on the principle of quantum interference in superconducting loops containing Josephson junctions. Owing to the quantized state of the superconducting loop and the non-linear behavior of the Josephson junction, this device can detect a very low fields as low as 5×10^{-18} T. The measurement sample enclosed in a gelatin capsule was fixed on the straw sample holder made of polypropylene, and installed into the sample chamber in both measurements of the temperature and magnetic field dependence.

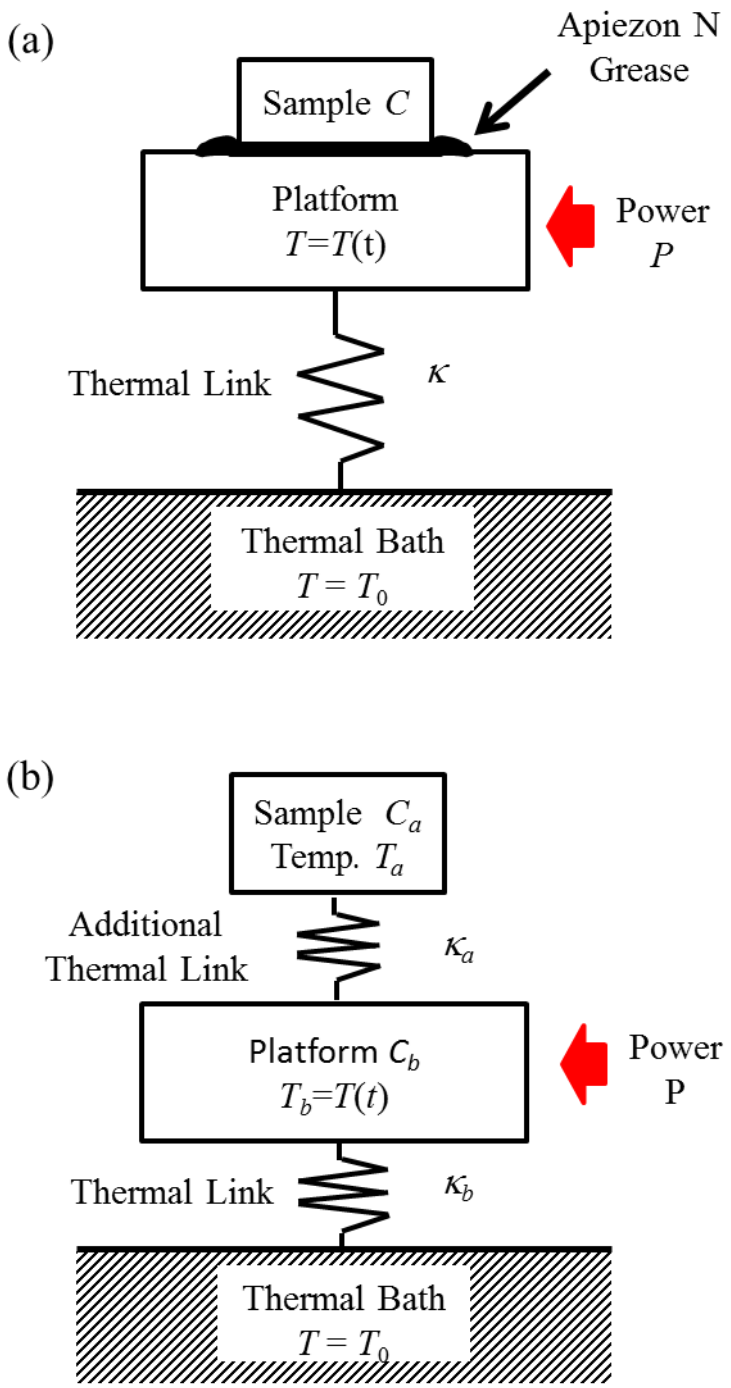

Fig. 2.1. Schematic model of thermal relaxation method with (a) 1τ method and (b) 2τ method. (b) is also used to introduce quasi-adiabatic method.

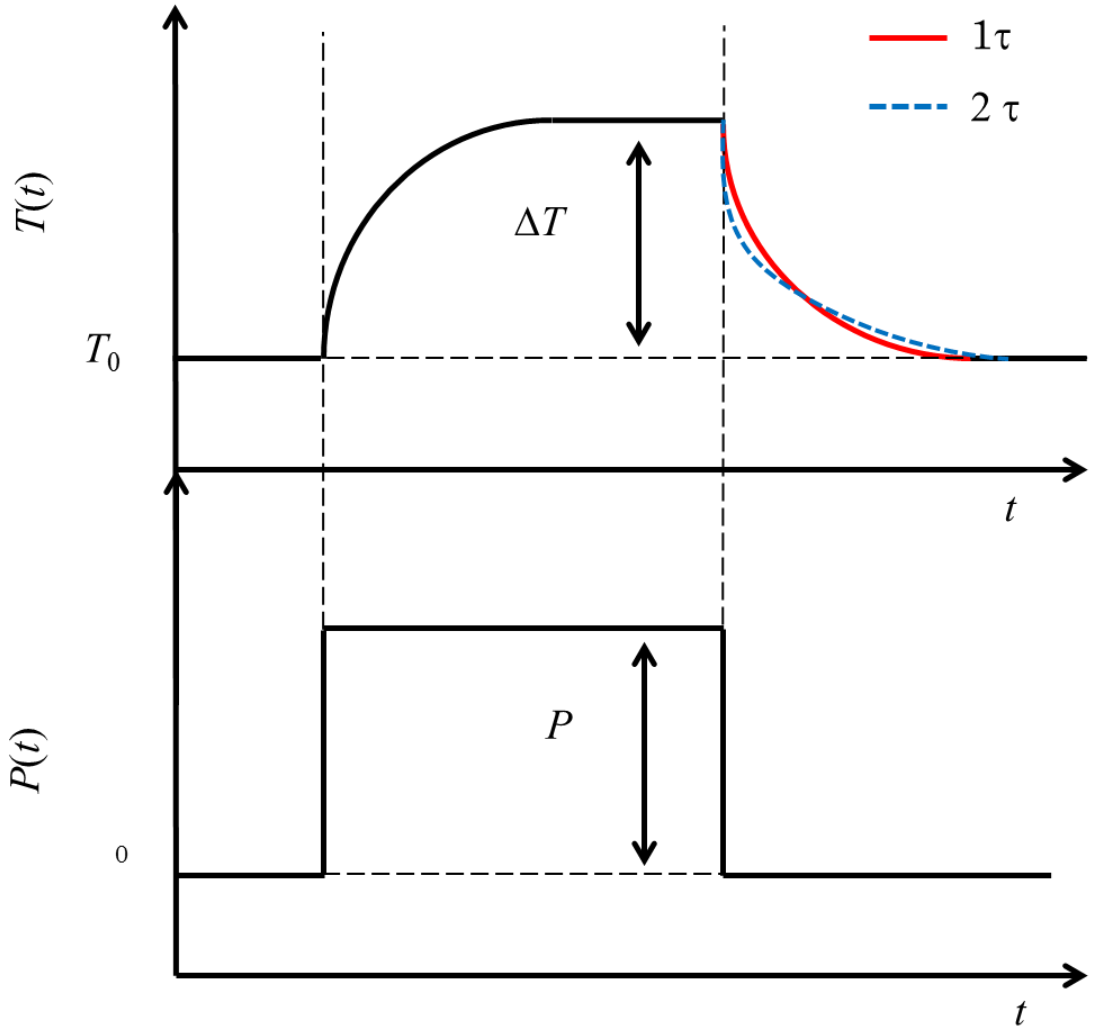

Fig. 2.2. Measurement procedure of the thermal relaxation method, showing the time dependence of a power P and a sample temperature T when a pulse electrical power P is applied to the heater. If there is 2τ effect, the thermal relaxation curve cannot be described by a single exponential function.

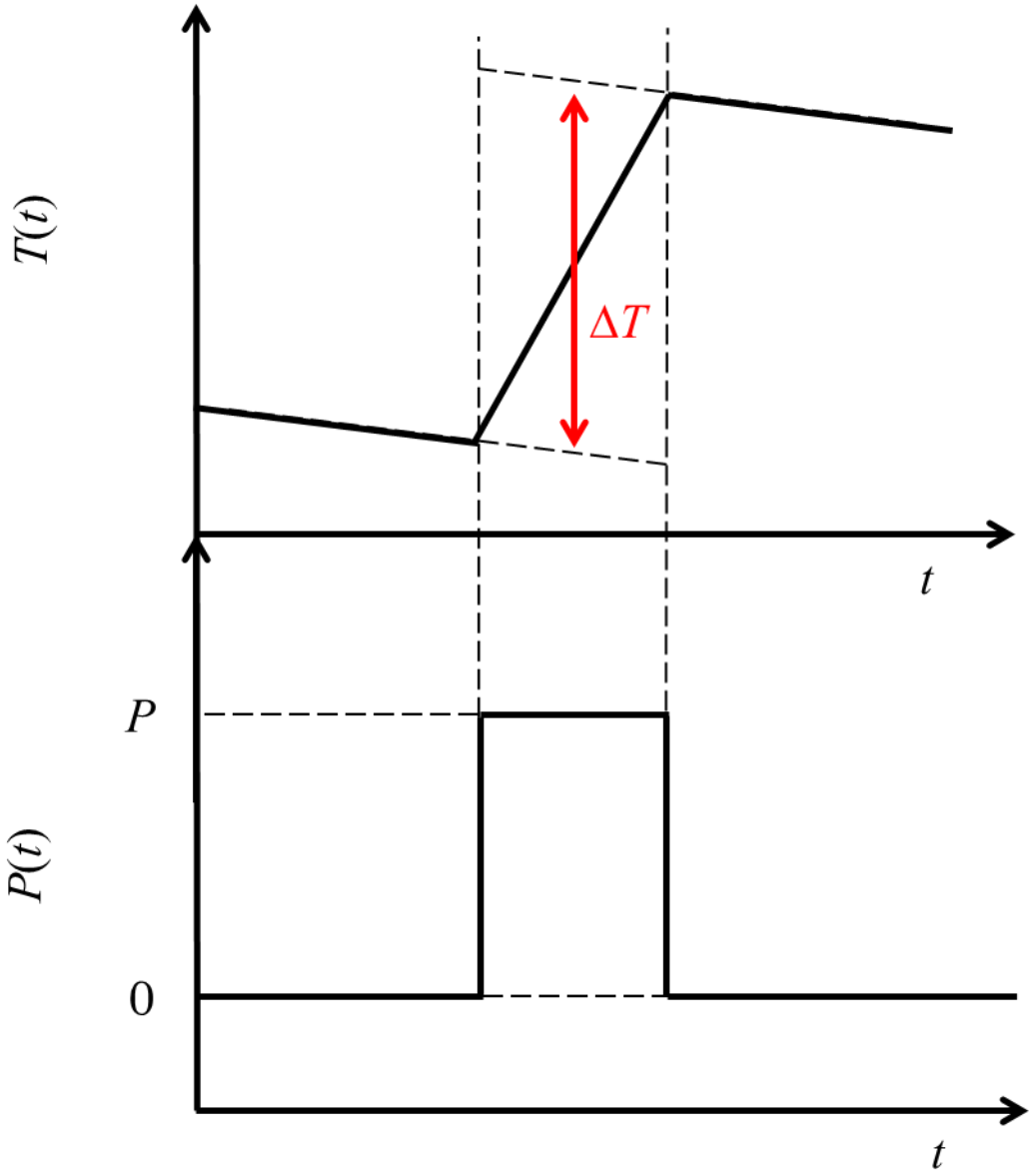

Fig. 2.3. Measurement procedure of the quasi-adiabatic method, showing the time dependence of a power P and a sample temperature T when a pulse electrical power P is applied to the heater. If there is 2τ effect, the thermal relaxation curve cannot be described by a single exponential function.

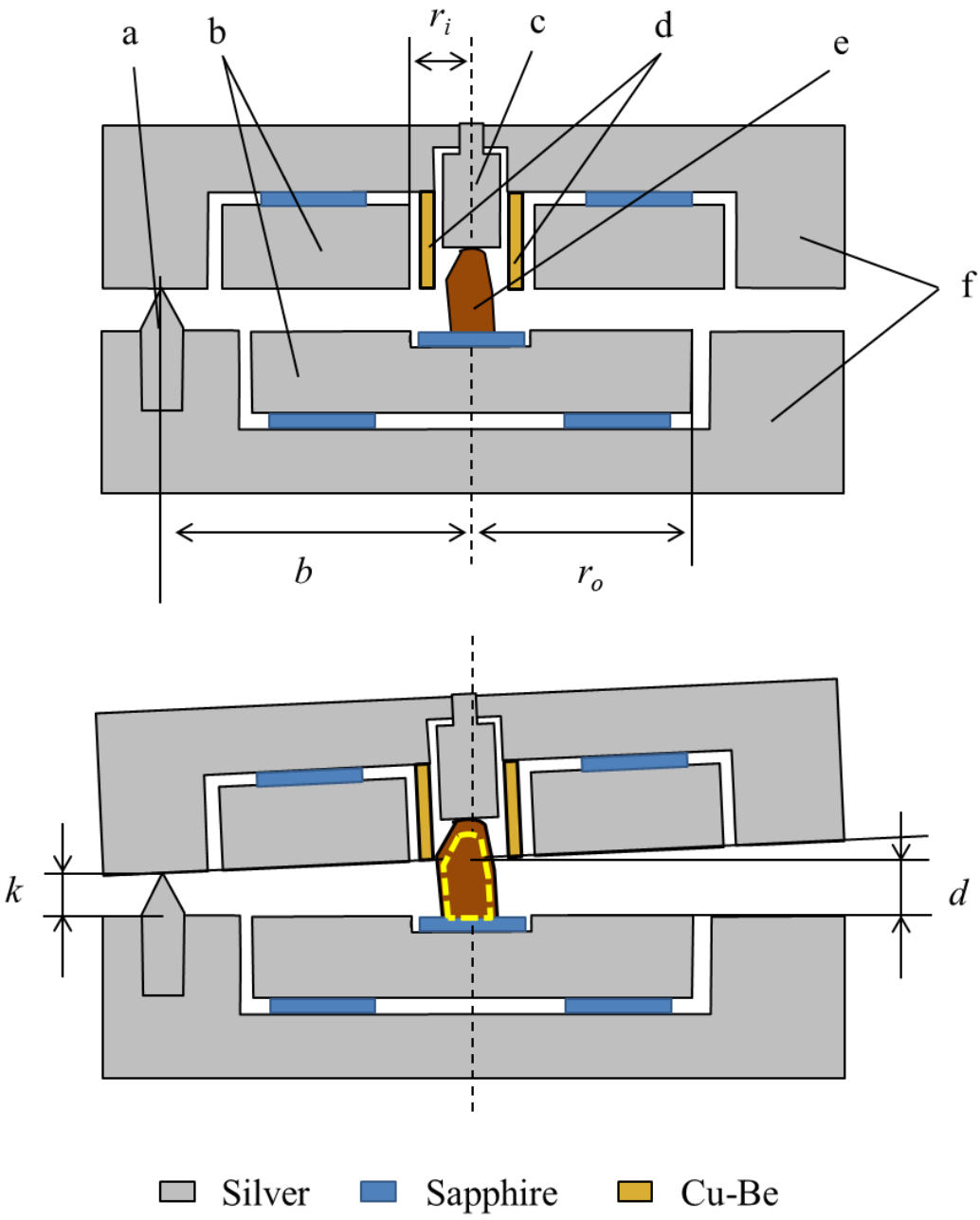

Fig. 2.4. Upper: Schematic model of capacitance dilatometer (a) Cone bearing (b) Capacitor plates (c) Silver spacer (d) Electrical shielding of sample space (e) Sample (f) Capacitor plate holder. Lower: Effect of the expansion of the sample, where the yellow dashed line represents the original sample shape.

References

[1] R. Bachmann, F. J. DiSalvo, Jr., T. H. Geballe, R. L. Greene, R. E. Howard, C. N. King, H. C. Kirsch, K. N. Lee, R. E. Schwall, H. U. Thomas, and R. B. Zubeck, Rev. Sci. Instrum. **43**, 205 (1972).

[2] G. K. White, Experimental Techniques in Low Temperature Physics, 3rd ed. Clarendon, Oxford, 1979, Chap. VII.

[3] G. K. White, Cryogenics **1**, 151 (1961).

[4] M. Rotter, H. Müller, E. Gratz, M. Doerr, and M. Loewenhaupt, Rev. Sci. Instrum. **69**, 2742 (1998).

[5] N. Mehboob, Master Thesis, Vienna University of Technology, (2009).

[6] A. Savitzky and M. J. E. Golay, Anal. Chem. 36, 1627 (1964).

Chapter 3

Spin-glass-like behavior in ferromagnetic phase of $CdCr_2S_4$

3.1 INTRODUCTION

In the sulfide spinel $CdCr_2S_4$, the 90° Cr^{3+}-X^{2-}-Cr^{3+} ferromagnetic superexchange interaction becomes dominant, while the direct Cr-Cr exchange becomes considerably weaker due to increasing the distance between the Cr^{3+} ions. The dominant ferromagnetic superexchange leads to a ferromagnetic ground state (T_C=84.5 K). Since $CdCr_2S_4$ was found in 1960s, much attention has been attracted by the mutual coupling between magnetic and electric properties. The most impressive findings are probably the relaxor ferroelectricity above T_C, and multiferroicity and colossal magnetocapacitance below T_C [1, 2]. Although there has been a dispute whether the multiferroic behavior is intrinsic [3, 4], the possibility of the multiferroicity have been supported by the findings of intrinsic local distortion (off-centering of the Cr ions) [5, 6, 7]. The local distortion leads to a non-centrosymmetric space group, and it provides the explanation for the mechanism of the multiferroic behavior in $CdCr_2S_4$. That distortion may be related to the observations of an unusual thermal expansion behavior [8] and a broadening of x-ray peaks [9]. Another interesting topic is an anomalous temperature dependence of heat capacity below 20 K [8], which contradicts with results of powder inelastic neutron scattering experiments showing a typical spectrum for conventional Heisenberg ferromagnet [10]. This finding is probably related to sharp drop of the

dielectric constant [1], and the emergence of magnetocrystalline anisotropy [6].

Those reports suggest the need to revisit the basic properties of the ferromagnetic phase. In addition, the previous heat capacity measurements between 2 K and 300 K found out two anomalous behaviors [11]. First is the peak of the magnetic heat capacity around 10 K, at where there has been no report of an anomaly in other physical properties. Second is the significant shortfall of the estimated entropy for the ferromagnetic phase transition. Hence, heat capacity, thermal expansion, and magnetic measurements were carried out on the single crystal $CdCr_2S_4$. The heat capacity is able to provide the information of the excitation spectrum and the entropy. Especially, the analysis of low temperature heat capacity let us know what kind of excitations exist as simple temperature dependences; e.g., T^3 for phonons and $T^{3/2}$ for ferromagnetic spin waves. The coefficients of these terms provide the stiffness of each degree of freedom. The thermal expansion is so sensitive for a structural change that some indication of the local lattice distortion would be captured. Several magnetization measurements have been carried out, though there is no detailed consideration of the magnetization behavior under low magnetic field and the *ac* susceptibility measurements in ferromagnetic phase. This study reports that those measurements show the sign of spin-glass-like behaviors in $CdCr_2S_4$, which has been regarded as a conventional ferromagnet.

3.2 EXPERIMENTAL

Single crystals of $CdCr_2S_4$ used for the measurements were from the same batch as in Ref. [8], which were grown by a chemical vapor transport technique with $CrCl_3$ as the transport agent. Heat capacity was measured by the relaxation technique with two calorimeters for different temperature regions: from 0.10 to 2.5 K a homemade

relaxation-type calorimeter with a ^{3}He/^{4}He dilution refrigerator [12], and from 2 to 300 K a Quantum Design PPMS. Thermal expansion measurements were carried out by the capacitance dilatometer made from silver. a capacitance dilatometer constructed from silver. The measurements were performed on the same samples used in the heat capacity measurements with the direction along the cubic <111> and the length of 1.13 mm. The magnetization and *ac* susceptibility measurements were performed on collections of single crystals over the temperature range 2 to 100 K with a Quantum Design MPMS. The magnetization was measured on cooling and heating direction up to the magnetic field of 5 T. The *ac* susceptibility was measured on heating direction in an *ac* field H_{ac}=3.8 Oe with the frequency range 1 to 997 Hz.

3.3 RESULTS AND DISCUSSION

3.3.1 Heat capacity

The heat capacity divided by temperature C_pT^{-1} is shown in Fig. 4.1. The C_pT^{-1} at 0 T showed a sharp peak at T_C=84.5 K. In the magnetic field of 7 T, this peak was broadened and shifted to around 110 K. This magnetic field response is general for a simple Heisenberg ferromagnet. Each heat capacity curve overlapped only above 250 K, which means that the spin fluctuation exists up to approximately 250 K. In order to extract the magnetic contribution to the heat capacity, the lattice contribution was estimated by temperature scaling the heat capacity of the nonmagnetic reference compound $CdSc_2S_4$ by a scaling factor of 1.02 to account for the difference in the molecular weight (solid line in Fig. 4.1). The validity of this estimation is supported from that the estimated lattice heat capacity curve and the measured heat capacity

curves are almost in line above 250 K. By subtracting the lattice heat capacity from the heat capacity, the magnetic heat capacity C_m at 0 and 7 T was obtained as presented in the inset of Fig. 4.1. The interesting thing is the existence of anomalous peaks at around 10 and 35 K besides the peak of the ferromagnetic phase transition. However, the small peak at 35 K did not show the temperature shift or intensity change with applying magnetic field, which indicates that this peak would be resulted from an apparatus problem. Actually, the subtraction of the heat capacity at 7 T from 0 T vanishes the anomaly of the C_m at zero field. Hence, this anomaly will be not touched more in this paper. The peak at 10 K was suppressed by the magnetic field, and, surprisingly, still remained under 7 T. It suggests the development of some kind of magnetic ordering around 10 K. However, the spins must be completely ordered in this temperature region, under the magnetic field of 7 T [1, 10]. Thus, the origin of this anomaly would be considered to be not only an unknown magnetic excitation but also the change of lattice vibrations, suggesting the presence of the spin-lattice coupling. Integrating the C_mT^{-1} gives the ferromagnetic transition entropy S=8.0 J K^{-1} mol^{-1} for either case, which is far from the theoretical value $S=2R\ln 4$~23.1 J K^{-1} mol^{-1} for a spin system with S=3/2. The anomalous excitation at low temperature gives only S=1.9 J K^{-1} mol^{-1}. Accordingly, the shortfall of the transition entropy might also indicate the occurrence of anomalous lattice vibrations over the wide temperature range.

In order to understand the low-temperature anomaly, the low-temperature heat capacity was investigated. Figure 4.2 represents the low-temperature heat capacity C_p in full logarithmic scale. The low-temperature C_p under zero magnetic field was proportional to $T^{1.37}$, which essentially agrees with the previous report [13]. Although the magnetization measurements and powder inelastic neutron scattering experiments

have been verified being a simple Heisenberg ferromagnet [1, 10], this temperature dependence is obviously different from a conventional ferromagnet behavior $C_p = \delta T^{3/2} + \beta T^3$, where the δ and β term corresponds to the contributions from the ferromagnetic spin waves and the phonons. Based on this fact, it can be assumed that the existence of an unknown excitation have a *T*-linear contribution for the C_p besides the ferromagnetic spin wave and phonon excitations. The *T*-linear contribution in non-metallic systems is usually observed in the glass system due to a continuous density of states. For the data below 2 K, a least square fit with the equation, $C_p = \alpha T + \delta T^{3/2} + \beta T^3$, was successfully reproduced the measurement result with the coefficients α=15.1 mJ K^{-2} mol^{-1}, δ=36.7 mJ $K^{-2.5}$ mol^{-1}, β=0.49 mJ K^{-4} mol^{-1}, as shown in the inset of Fig. 2.

The value of the β corresponds to the Debye temperature Θ_D=303 K. On the other hand, the analysis of the far-infrared spectroscopy measurements lead to the Θ_D=372 K by using the data of paramagnetic phase [13]. The present result means the softening of the lattice at low temperature indicating the existence of phonon softening as suggested in Raman scattering experiments [5].

The value of the δ is related to the spin-stiffness constant *D* through δ=0.113$V_m K_B^{2.5}/D^{1.5}$ [14], where V_m is the molar volume and k_B is the Boltzmann constant. Then, the present result leads to *D*=19.6 meV Å^2. The *D* can also be evaluated from the equation $D = (S/3)\sum_n z_n J_n a_n^2$ [15], where *S* is the quantum number, z_n is the number of the *n*th nearest neighbor atom, J_n is the exchange coupling constant between the *n*th nearest neighbor pairs, and a_n is the *n*th nearest neighbor distance. The exchange constants are available from inelastic neutron scattering experiments: the first nearest neighbor J_1/k_B=13.25 K, the third nearest neighbor J_3/k_B=-0.915 K, and other contributions are negligible [10]. The other terms, z_1=6, a_1=3.62 Å, z_3=12, and a_3=7.24

Å, are calculated from the crystal structure of the $Fd\bar{3}m$ space group with the lattice constant 10.24 Å [16]. These values amount to D=20.1 meV Å^2, which is in good agreement with the values estimated from the heat capacity data. This consistency convinces the presence of the ferromagnetic spin waves in the ground state, and hence the existence of an unknown excitation in low-temperature region.

Under 7 T, the C_p below 2 K was well described by only the T^3 term with β=2.55 mJ K^{-4} mol^{-1}. The T^3 dependence means the presence of only the phonon excitations due to the suppression of the ferromagnetic spin wave excitations by the magnetic field. The value of the coefficient β leads to the Debye temperature Θ_D=175 K, which is significantly smaller than its zero field value. This result suggests that the lattice vibrations are highly changed by the magnetic field. Although magnetic field is generally assumed to have little effect on lattice vibrations, the effect of magnetic field on the Θ_D has been observed in some compounds [17]. In $CdCr_2S_4$, magnetic field might affect the lattice vibration due to strong spin-lattice coupling. Indeed, a large magnetostriction has been found in the spin-lattice coupled system [18]. Considering that the change in magnetic field give rise to the huge change in an anomalous peak around 10 K, large magnetostriction might be appeared at low temperature.

3.3.2 Thermal expansion

The thermal expansivity $\Delta L/L_0$ of $CdCr_2S_4$ is shown in Fig. 3(a), which is in good agreement with the report of the x-ray measurements [19], and essentially same with Ref. [8]. With decreasing temperature from room temperature, the lattice contracts down to near T_C. However, from there negative thermal expansion appeared, and it kept down to 2 K. The thermal expansion coefficient α obtained from the $\Delta L/L_0$ is depicted in Fig.

3(b). The α shows the large negative peak at the ferromagnetic transition, followed by the gradual upturn, which tends to converge to zero at $T = 0$.

The pressure dependence of the ferromagnetic transition temperature dT_C/dp was estimated using the baselines shown in Fig. 4. For the second-order ferromagnetic transition, dT_C/dp can be evaluated from the Ehrenfest relation, given as $dT_C/dp = \Delta\beta V_m T_C/\Delta C_p$, where $V_m = 8.1 \times 10^{-5}$ m^3 mol^{-1} is the molar volume [20], $\Delta\beta = 3\Delta\alpha$ is the jump in volume thermal expansion coefficient at T_C, and ΔC_p is the jump in C_p at T_C. The estimation in Fig. 4 leads to $\Delta\alpha = -2.2 \times 10^{-6}$ K^{-1} and $\Delta C_p = 5.9$ J K^{-1} mol^{-1}, resulting in $dT_C/dp = -7.7$ K/GPa, which reasonably agrees with $dT_C/dp = -5.8$ K/GPa of obtained from the magnetic susceptibility measurements under applying pressure [19]. The negative sign of dT_C/dp indicates that the system will be unstable with contracting the lattice. The onset temperature of the negative thermal expansion is fairly close to T_C, which suggests that an unclear interaction competing to ferromagnetic interaction is developed with forming the ferromagnetic ordering.

Negative thermal expansion generally appears to relieve a frustration in the system. In particular, if the frustration stems from the magnetic property, negative thermal expansion implies the presence of spin-lattice coupling. Among chromium chalcogenide spinels, $ZnCr_2S_4$ and $ZnCr_2Se_4$ have exhibited negative thermal expansion [21]. They show positive but rather small Curie-Weiss temperature than $CdCr_2S_4$, which indicates the presence of stronger antiferromagnetic interaction than in $CdCr_2S_4$. Hence, both compounds have the bond frustration between the superexchange interactions of nearest neighbor ferromangetic Cr-S(Se)-Cr and next nearest neighbor antiferromagnetic Cr-S(Se)-Zn-S(Se)-Cr, resulting in the antiferromagnetic state with a complex ordering. This antiferromagnetic transition is accompanied by the structural transition, which has

been attributed to the strong spin-lattice coupling to relieve the frustration. On the other hand, $CdCr_2Se_4$ and $HgCr_2Se_4$, which have a stronger ferromagnetic interaction than $CdCr_2S_4$, do not exhibit any anomalous properties as noted above [22]. Thus, it is speculated that the presence of the bond frustration in $CdCr_2S_4$ leads to negative thermal expansion through the spin-lattice coupling. Indeed, recent far-infrared spectroscopy indicate an evidence of the strong spin-lattice coupling [20]. The strong spin-lattice coupling may be originated from the local lattice distortion. For the nature of the local lattice distortion, a second-order Jahn-Teller effect has been considered [5]. It should be noted that the recent theoretical study on the pyrochlore-based systems reveals that the spin-lattice coupling resulting from a local lattice coupling plays an important role for the spin-glass behavior [23].

3.3.3 Magnetic properties

The magnetic field and temperature dependence of the magnetization are presented in Fig. 3(a) and 3(b), respectively. The *M*-*H* curves exhibit a typical soft magnetic behavior with the coercivity field less than 10 Oe in the whole temperature range in the ferromagnetic phase. At 4.5 K, the magnetization almost saturated with a magnetic field 1 T to 5.8 μ_B/f.u., which is consistent with the expected value 6 μ_B/f.u.. The temperature dependence of the magnetization *M* was obtained on cooling (FC) and heating (FCH) procedure in a field of 30 Oe. Although the overall view of the *M* is quite similar to the previous magnetization measurements [1], a temperature hysteresis was found as the inset of Fig. 4.5. With decreasing temperature, the *M* decreased through a broad maximum around 40 K. In the normal ferromagnet, the *M* should increase with decreasing temperature due to the suppression of thermal fluctuation. It was confirmed

that the decrease of the *M* and the hysteresis were gradually vanished with increasing magnetic field, and could not be observed above 500 Oe. When the magnetic field was increased, the maximum magnetization of the FC curve shifted towards lower temperature, whereas that of the FCH curve stayed around 20 K. These results suggest the occurrence of an irreversible change of the magnetic state below 20 K.

In order to figure out this unusual magnetic property, *ac* susceptibility measurements were performed with frequencies 1 to 997 Hz. The real (χ') and imaginary (χ") components of *ac* susceptibility are shown in Figs. 4(a) and 4(b), respectively. (The χ" is standardized to zero by the value at 80 K.) The χ' sharply increased at T_C, and gradually decreased below T_C, which indicates very soft magnetically. The striking feature of the *ac* susceptibilities are the frequency dispersion below 25 K. As the occurrence of the frequency dispersion in the χ', the χ' decreased and the χ" increased from near temperature. Similar behavior of the χ" was observed in the *ac* susceptibility measurements with the frequency at 0.4 Hz for polycrystalline powders [24]. Because the χ" corresponds to the dissipative processes, the present results imply that an irreversible movement of the spins occurs below 20 K.

The frequency dependence in the χ" appeared below 100 K might be resulted from the short-range magnetic clusters [7]. If the magnetic clusters remain down to the lowest measurement temperature, some influence will be appeared in the frequency dependence in the χ' and the increase of the χ" below 20 K. In addition, the frequency dependence of the peaks was observed in the χ", which follows an Arrhenius law with an activation energy E_a ~ 770 K. The simplest interpretation is that the activation energy relates to the short range magnetic clusters. In that case, the clusters would consist of about 60 spins. However, the nature of the peak shift is unclear so far.

The anomalous excitation was appeared in the magnetic heat capacity below about 20 K, which suggests a correlation to the unusual magnetic behaviors. In addition, either the *T*-linear term in the low-temperature heat capacity and the frequency dependence in the *ac* susceptibilities look like spin-glass-like behavior. Although the formation of spin-glass state seems to be able to explain the current results, this hypothesis is denied by the existence of the ferromagnetic spin wave excitations at low-temperature. Considering that at low temperature the magnetization saturates relatively weak magnetic field with showing very small magnetic hysteresis as seen in Fig. 3(a), the spin-glass-like behavior might be attributed to the realization of a superparamagnetic-like state. Superparamagnetism is generally seen in nanoparticle system, and known to show the frequency dependence in *ac* susceptibility. Similar behavior has been observed in spinel oxides where the magnetic ions are placed on the *A*-site and the *B*-site are replaced by the non-magnetic ion [25]. This superparamagnetism stems from anisotropic magnetic interactions generated by non-magnetic ion substitution. By analogy, it could be expected that the short-range magnetic cluster in $CdCr_2S_4$ behaves as nanoparticles in ferromagnetic phase.

The superparamagnetic-like property in $CdCr_2S_4$ might be induced by a trigonal distortion of the CrS_6 octahedra below 20 K [6]. The trigonal distortion will orient the magnetic moment of a short-range magnetic cluster to a local easy axis. Because the ferromagnetic interaction remains down to zero temperature, other clusters also tend to orient to same direction one after the other, and then a larger size of ferromagnetic spin cluster could assemble with decreasing thermal fluctuations. This process would create many cluster size depending on the condition of the local distortion around a cluster. The strong anisotropy at lower temperature enhances the formation of larger

ferromagnetic spin cluster, which makes the spins less effective for magnetic field. Therefore, with decreasing temperature, the magnetization decrease by trapping the ferromagnetic spin cluster along several directions, and the existence of many cluster size cause the frequency dependence behaviors in the *ac* susceptibility measurements. The anomalous excitation observed in the zero-field low-temperature heat capacity could also be explained as a continuous excitation of large size clusters of the ferromagnetic spins.

3.4 CONCLUSION

The existence of anomalous excitation in $CdCr_2S_4$ at low temperature was confirmed by the magnetic heat capacity and the temperature dependence of the low-temperature heat capacity. The low-temperature heat capacity can be well fitted by the equation, $C_p = \alpha T + \delta T^{3/2} + \beta T^3$, where an unknown excitation is included as a T-linear contribution for the C_p besides the ferromagnetic spin waves and phonons. Because even under high magnetic field the unexpected peak of the magnetic heat capacity was observed at low temperature besides the ferromagnetic transition, the anisotropic distortion might be substantially unaffected by magnetic field and induce low-energy lattice vibrations. The thermal expansion showed negative thermal expansion behavior below 100 K, which indicates the presence of the magnetic frustration. The magnetic susceptibilities exhibit the unusual behavior for a conventional ferromagnet corresponding to the anomalies in the heat capacity. The magnetization decreased below 20 K and showed the hysteresis in the whole temperature range. The frequency dependencies in the *ac* susceptibility suggest that two relaxation processes exist in ferromagnetic phase of $CdCr_2S_4$. These results suggest that

the short-range magnetic clusters gather and form larger spin clusters below 20 K. In order to unveil the unusual properties in low-temperature region, the mesoscopic scale measurements, *e.g.*, small-angle neutron and x-ray scattering experiments, would be desired to be carried out. Furthermore, *ac* susceptibility measurements at lower temperature range might also provide useful insights.

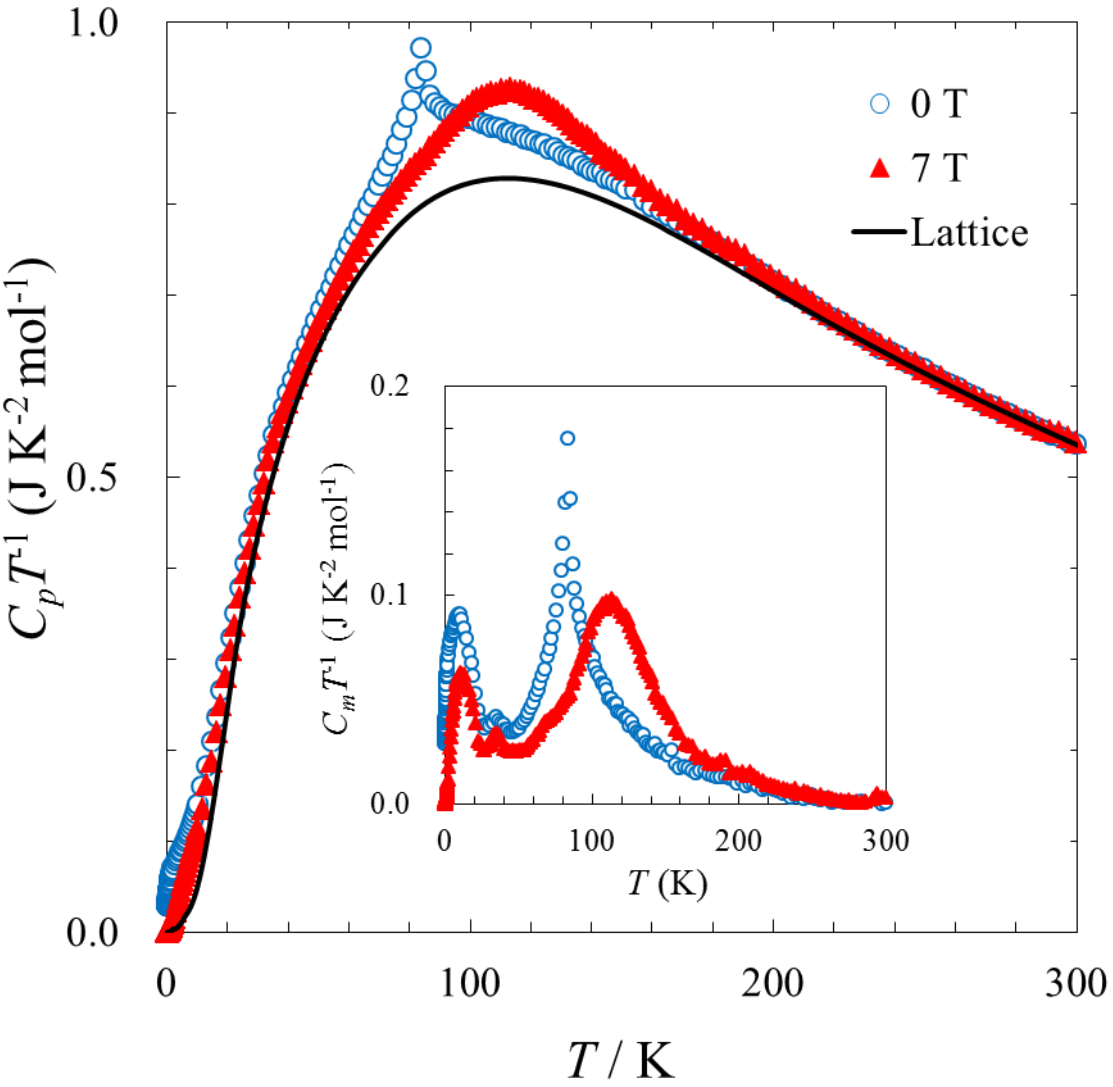

Fig. 4.1. Heat capacity divided by temperature C_pT^{-1} of $CdCr_2S_4$ under 0 T (open blue circles) and 7 T (closed red triangles). The dashed black line shows the lattice heat capacity calculated by scaling C_p of $CdSc_2S_4$. The inset displays the magnetic heat capacity divided by temperature C_mT^{-1} under 0 T (open blue circles) and 7 T (closed red triangles) obtained by subtracting the lattice heat capacity from the C_p.

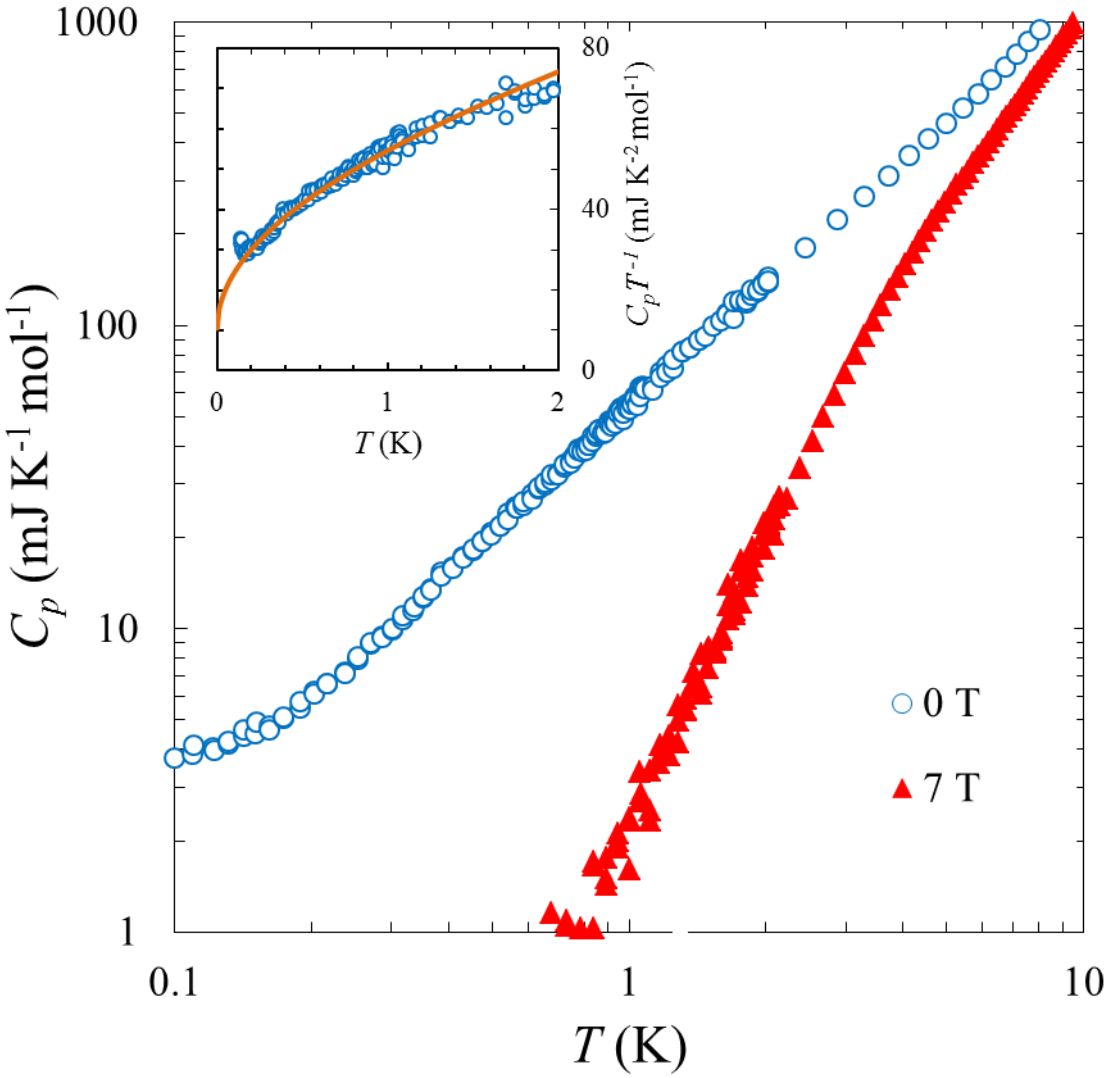

Fig. 4.2. Low-temperature heat capacity C_p of $CdCr_2S_4$ under 0 T (open blue circles) and 7 T (closed red triangles) in full logarithmic scale. The black lines correspond to $C_p \propto T^{1.37}$ for 0 T and $C_p \propto T^3$ for 7 T, respectively. The inset shows the heat capacity divided by temperature C_pT^{-1} below 2 K, where the red solid line represents the best fit of the heat capacity with $C_p = \alpha T + \delta T^{3/2} + \beta T^3$.

-

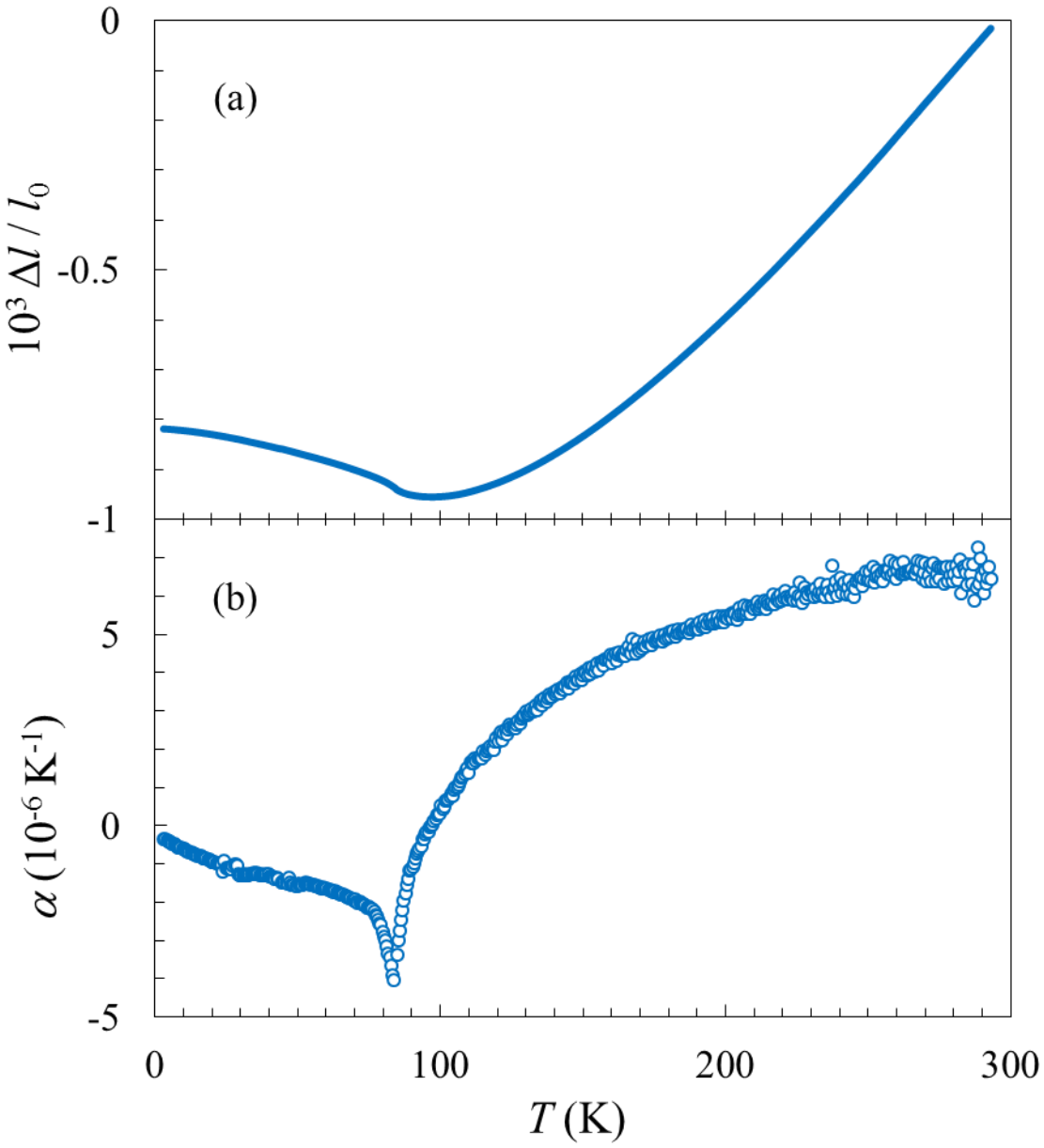

Fig. 4.3. (a) Thermal expansivity $\Delta L/L_0$ and (b) Thermal expansion coefficient α of $CdCr_2S_4$.

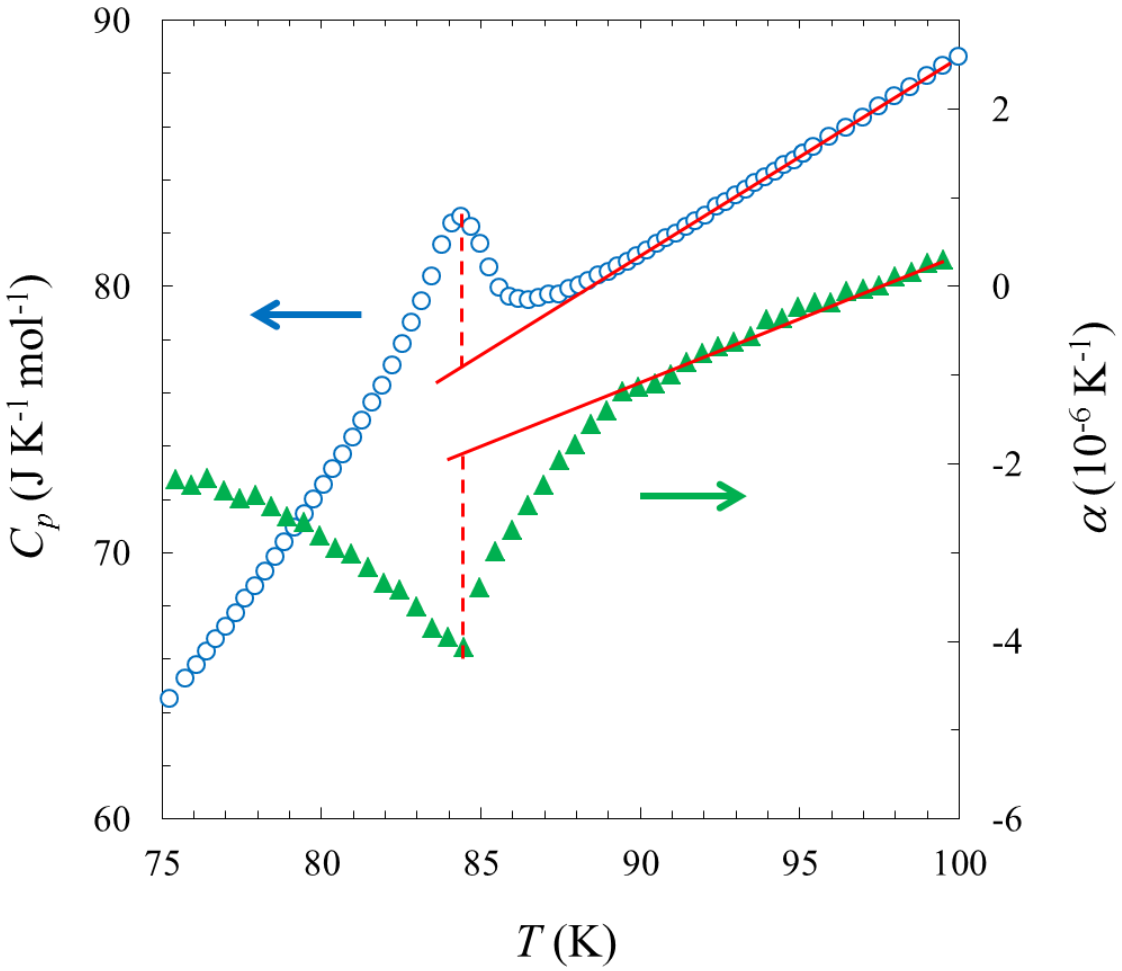

Fig. 4.4. (a) Heat capacity C_p (blue open circles) and thermal expansion coefficient α of $CdCr_2S_4$ of the vicinity of the ferromagnetic transition temperature T_C. The red lines are the baselines used to estimate the jumps in C_p and α.

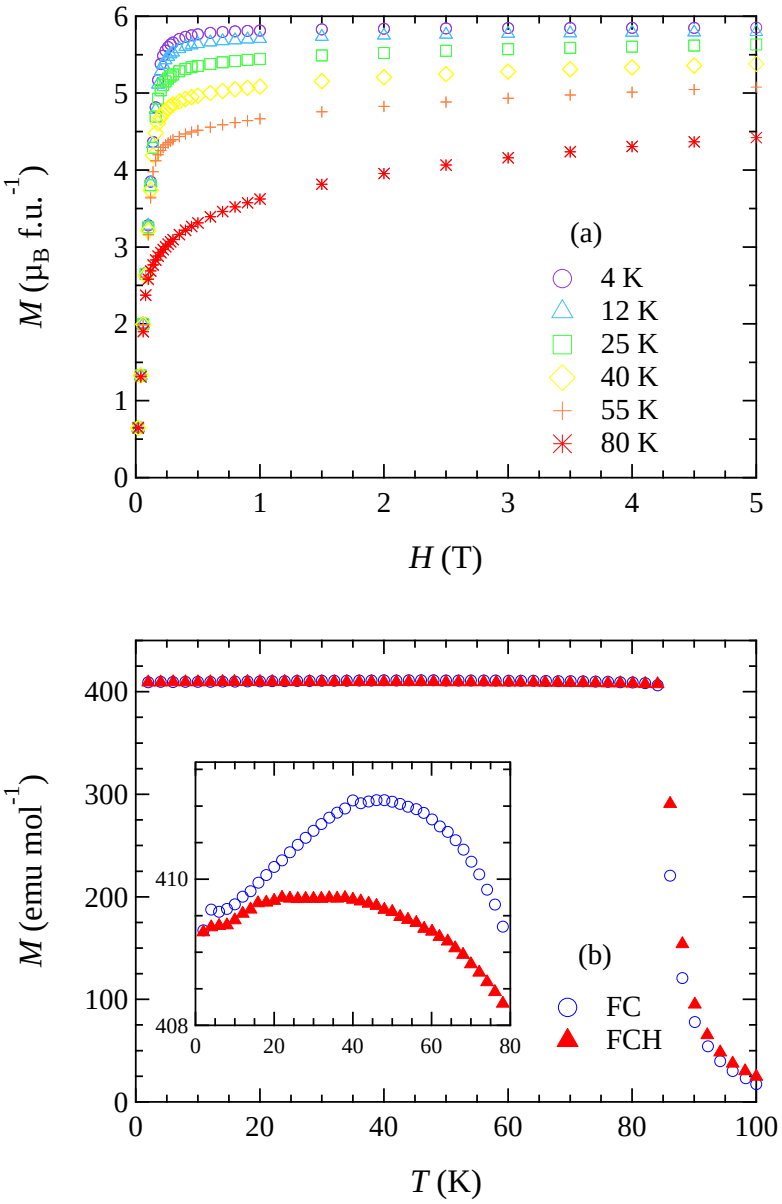

Fig. 4.5. Magnetization of $CdCr_2S_4$ as a function of (a) magnetic field in the ferromagnetic phase, and (b) temperature obtained on cooling (FC) and warming (FCW) procedure in a field of 30 Oe. The inset in (b) shows the enlarged magnetization curve below 80 K.

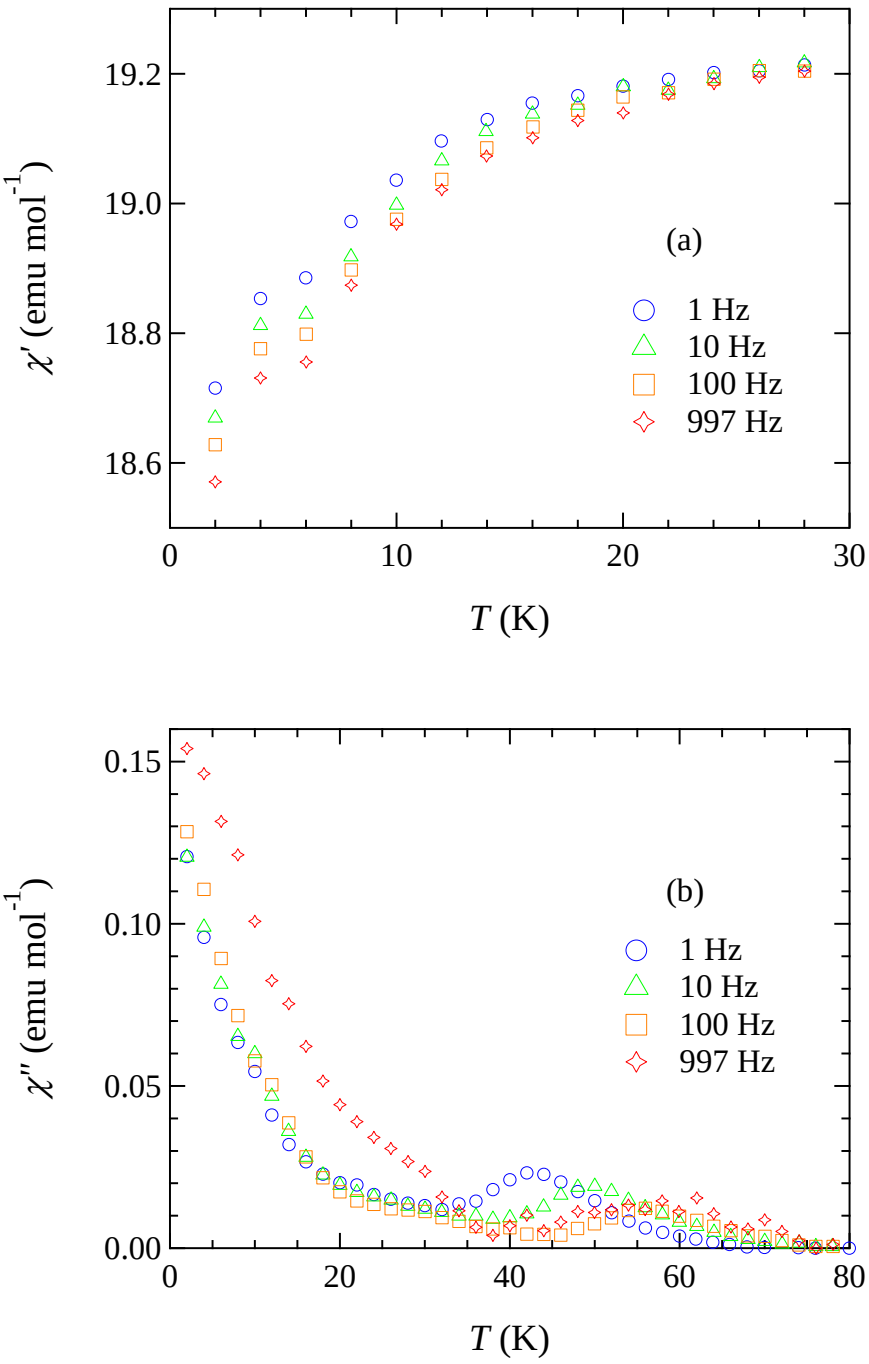

Fig. 4.6. The temperature dependence of (a) the real (χ') and (b) imaginary (χ") components of ac susceptibility with frequencies 1 to 997 Hz. The imaginary part is standardized to zero by the value at 80 K.

References

[1] J. Hemberger, P. Lunkenheimer, R. Fichtl, H.-A. Krug von Nidda, V.Tsurkan, and A. Loidl, Nature (London) **434**, 364 (2005).

[2] P. Lunkenheimer, R. Fichtl, J. Hemberger, V. Tsurkan, and A. Loidl, Phys. Rev. B **72**, 060103(R) (2005).

[3] G. Catalan and J. F. Scott, Nature (London) **448**, E4 (2007).

[4] J. Hemberger, P. Lunkenheimer, R. Fichtl, H.-A. Krug von Nidda, V.Tsurkan, and A. Loidl, Nature (London) **448**, E5 (2007).

[5] V. Gnezdilov, P. Lemmens, yu. G. Pashkevich, Ch. Payen, K. Y. Choi, J. Hemberger, A. Loidle, and V. Tsurkan, Phys. Rev. B **84**, 045106 (2011).

[6] D. Ehlers, V. Tsurkan, H.-A. Krug von Nidda, and A. Loidl, Phys. Rev. B **86**, 174423 (2012).

[7] G. N. P. Oliveira, A. M. Pereira, A. M. L. Lopes, J. S. Amaral, A. M. dos Santos, Y. Ren, T. M. Mendonca, C. T. Sousa, V. S. Amaral, J. G. Correia, and J. P. Araujo, Phys. Rev. B **86**, 224418 (2012).

[8] M. Tachibana, N. Taira, H. Kawaji, Solid State Commun **151**, 1776 (2011).

[9] H. Göbel, J. Magn. Magn. Mater. **3**, 143 (1976).

[10] S. Pouget, M. Alba, N. Fanjat, and M. Nogues, Physica B **180**-**181**, 244 (1992).

[11] K. Mizushima, Master thesis, Tokyo Institute of Technology, (2010).

[12] Y. Kohama, T. Tojo, H. Kawaji, T. Atake, S. Matsuishi, and H. Hosono, Chem. Phys. Lett. **421**, 558 (2006).

[13] T. Rudolf, Ch. Kant, F. Mayr, J. Hemberger, V. Tsurkan, and A. Loidl, Phys. Rev. B **76**, 174307 (2007).

[14] C. Kittel, Quantum Theory of Solids, Wiley, New York, (1963).

[15] S. N. Kaul, Phys. Rev. B **27**, 5761 (1983).

[16] P. K. Baltzer, P. J. Wojtowicz, M. Robbins, and E. Lopatin, Phys. Rev. **151**, 367 (1966).

[17] J. Lopez, O. F. de Lima, P. N. Lisboa-Filho and F. M. Araujo-Moreira, Phys. Rev. B **66**, 214402 (2002).

[18] J. Hemberger, H.-A. Krug von Nidda, V. Tsurkan, and A. Loidl, Phys. Rev. Lett. **98**, 147203 (2007).

[19] V. C. Srivastavat, J. Appl, Phys. **40**, 1017 (1969).

[20] T. Rudolf, Ch. Kant, F. Mayr, J. Hemberger, V. Tsurkan, and A. Loidl, New J. Phys. **9**, 76 (2007).

[21] F. Yokaichiya, A. Krimmel, V. Tsurkan, I. Margiolaki, P. Thompson, H. N. Bordallo, A. Buchsteiner, N. Stüßer, D. N. Argyriou, and A. Loidl, Phys. Rev. B **79**, 064423 (2009).

[22] K. Wakamura, T. Arai, and K. Kudo, J. Phys. Soc. Jpn. **41**, 130 (1976).

[23] H. Shinaoka, Y. Tomita, and Y. Motome, Phys. Rev. B **90**, 165119 (2014).

[24] V. Dupuis, E. Vincent, M. Alba, and J. Hammann, Eur. Phys. J. B **29**, 19 (2002).

[25] Y. Ishikawa, J. Appl. Phys. **35**, 1054 (1964).

Chapter 4

Spin-lattice coupling effect in strongly geometrically frustrated spinel $CdCr_2O_4$

4.1 INTRODUCTION

This chapter focus on the cubic spinel oxide $CdCr_2O_4$, in which the tetrahedral *A* site is occupied by the non-magnetic ion Cd^{2+} ($e^4\ t_2^6$), and the octahedral *B* site by the magnetic ion Cr^{3+} ($t_{2g}^3\ e_g^0$). The dominant exchange interaction is an antiferromagnetic nearest neighbor interaction between Cr^{3+} ions due to the direct overlap of t_{2g} orbitals. Due to Cr^{3+} ions forming the pyrochlore network, $CdCr_2O_4$ becomes a strongly frustrated Heisenberg antiferromagnet. Because of the strong frustration, the paramagnetic phase remains well below the Curie-Weiss temperature $|\Theta_{CW}| = 70$ K. In addition, a spin-liquid like state with the low-energy excitation of an antiferromagnetic hexagonal spin cluster has been observed in the paramagnetic phase, as shown in Fig. 4.1 [1, 2]. At $T_N = 7.8$ K, $CdCr_2O_4$ undergoes a a magnetostructural transition from a cubic paramagnetic phase to a tetragonal antiferromagnetic phase, which is elongated in the *c* axis to relieve the frustration. Neutron scattering studies [1, 3] reveal that the magnetic structure of the antiferromagnetic state has an incommensurate wave vector $\boldsymbol{Q}$~(0,0.09,1). This long-range spiral ordering has been attributed to the weak Dzyaloshinskii-Moriya interactions [4].

The magnetostructural transition indicates the presence of the strong spin-lattice coupling in this system. It is also suggested by far-infrared spectroscopy [5, 6, 7]

because a T_{1u} phonon mode correlated with the modulation of the Cr-Cr distance shows a phonon softening below approximately 130 K. Furthermore, the phonon triplet splits into singlet and doublet at T_N, which indicates a separation of the vibrations along *xy*, *yz*, and *zx* into two groups, corresponding to the tetragonal distortion [5]. For the mechanism of the splitting, Tchernyshyov *et al*. proposed the model including the spin-lattice coupling [8]. This model first assumes Ising spins fixed along *c* axis. Due to the geometrical frustration, spins will align parallelly or antiparallelly to its nearest neighbors. Then, to reduce the magnetic energy between parallel spins, the elastic energy to expand the distance between these spins arises. Thus, the nearest neighbor antiferromagnetic interaction induces the magnetic anisotropy, which related to the phonon mode splitting at the magnetostructural transition. It is noteworthy that a similar mode splitting has been observed in $ZnCr_2O_4$, which has the same crystal structure and stronger antiferromagnetic interaction. However, the splitting occurs in a different manner; the ratio of the intensity between singlet and doublet infrared phonon spectrum is opposite [9], indicating that at T_N the lattice elongates along the *c*-axis in $CdCr_2O_4$ [1], while contracts in $ZnCr_2O_4$ [10]. The nature of the different distortion has remained unclear yet.

In the present study, the effect of the magnetic frustration on the thermal expansion behavior has been investigated. Although several experiments suggest the presence of the spin-lattice coupling in $CdCr_2O_4$, the detailed thermal expansion data have not been reported. The thermal measurements on $CdCr_2O_4$ will be especially valuable in figuring out the lattice behavior in the paramagnetic phase, and how the lattice strains through the magnetostructural transition.

4.2 EXPERIMENTAL

Single crystals of $CdCr_2O_4$ were synthesized by a flux method using PbO as the flux [11]. To estimate the lattice heat capacity of $CdCr_2O_4$, single crystals of $ZnGa_2O_4$ were prepared by a flux method using PbO and B_2O_3 as the flux [12].

Magnetic susceptibility measurements were carried out using Quantum Design MPMS. Heat capacity was measured by the relaxation technique using a Quantum Design physical property measurement system (PPMS) for the temperature range from 2 to 300 K. Thermal expansion measurements were carried out with a capacitance dilatometer constructed from silver [13]. The specimens, which were the same samples used for the heat capacity measurement were measured along the cubic <111> direction with the length of 1.10 mm. Thermal expansivity data $\Delta L/L_0$ ($\Delta L = L - L_0$; L_0 refers to the value at 293 K) were taken on heating direction with a rate of 1 K/min between 2 and 300 K.

4.3 RESULTS AND DISCUSSION

4.3.1 Magnetic Susceptibility

Figure 4.2 shows the magnetic susceptibility χ of $CdCr_2O_4$ under 1000 Oe, which is in good agreement with the previous reports [9]. The susceptibility curve exhibited a broad maximum around 10 K, followed by a sharp jump due to the magnetostructural transition at T_N = 7.8 K, as shown in the inset of Fig. 4.2. The broad maximum can be attributed to the strong spin fluctuation caused by the geometrical frustration. A linear fit to the experimental data between 150 K and 300 K shown in Fig. 4.2 as the solid curve, yields a Curie-Weiss temperature Θ_{CW} = −70 K and an effective magnetic

moment p_{eff} = 3.75 μ_B/Cr. The latter value agrees with the theoretical spin-only value of p = 3.87 μ_B/Cr for Cr^{3+} resulting from a $3d^3$ state, which indicates that the spins behave as the paramagnetic state above 150 K.

4.3.2 Heat capacity

The heat capacity C_p of $CdCr_2O_4$ is presented in Fig. 4.3, which shows a very sharp peak due to the magnetostructural transition at T_N = 7.8 K. The result agrees with the previous experiments, except for a sharper peak [9]. The dashed line in Fig. 4.3 denotes the estimated lattice heat capacity. The lattice heat capacity was determined from the C_p of $ZnGa_2O_4$ with its temperature axis scaled by 1.075 to overlap with the C_p of $CdCr_2O_4$ above 150 K. Figure 4.3 shows The calculated magnetic entropy of 24.0 J K^{-1} mol^{-1} is in good agreement with the theoretical value $2R\ln4$ = 23.1 J K^{-1} mol^{-1}. The large contribution of the magnetic heat capacity above T_N shows that spin fluctuations exist up to approximately 150 K. Because the magnetostructural transition is first-order, the relaxation method could underestimate the latent heat at the transition; the validity of the present result was confirmed by comparing the transition entropy with the result of the adiabatic method [14].

4.3.3 Thermal expansion

Fig. 4.4(a) and 4.4(b) present the thermal expansitvity $\Delta L/L_0$ and thermal expansion coefficient α of $CdCr_2O_4$, respectively. With decreasing temperature from room temperature, $\Delta L/L_0$ first decreases and then increase below 140 K, which results in a broad minimum around 140 K. Such behavior, called negative thermal expansion

(NTE), is occasionally observed in frustrated materials [15, 16]. With further decreasing temperature, positive thermal expansion returns at 45 K. At T_N, there is a large jump in $\Delta L/L_0$ and an extremely sharp peak in α showing a large lattice distortion.

The onset temperature of the NTE coincides with the onset of the magnetic contribution in the C_p. Furthermore, the infrared spectra show softening of the phonon mode corresponding to the modulation of the Cr-Cr distance below the same temperature [5, 6, 7]. These behaviors have been attributed to the spin-lattice coupling [5], and this is also supported by *ab initio* calculation [17]. Thus, the NTE in $CdCr_2O_4$ should be related to the spin-lattice coupling. The mechanism of the NTE can be analogized from the idea that Tchernyshyov *et al.*[8] have proposed for the tetragonal distortion at T_N. When an antiferromagnetic couple of spins are established in a single tetrahedron, two other spins experiences the frustration. To reduce the frustration, the bond distance between the frustrated spins will be expanded. In this temperature range, the spins thermally fluctuate to a large degree. Thus, a bond expansion is dynamically induced in a tetrahedron rather than making a static structural distortion, and hence the volume expansion is occurred.

However, positive thermal expansion returns at 45 K. This behavior is in contrast to NTE observed in other spinel compounds with strong spin-lattice coupling that continues down to the lowest temperature or at least down to the transition temperature [15, 16]. Moreover, this positive thermal expansion has large positive value of $\alpha \sim 4.5 \times 10^{-6}\ \mathrm{K}^{-1}$ at 10 K, which is close to the value of $\alpha \sim 5.0 \times 10^{-6}\ \mathrm{K}^{-1}$ at room temperature. It indicates that the NTE may be correlated with a unique property in $CdCr_2O_4$. For $CdCr_2O_4$, the formation of antiferromagnetic hexagonal Cr cluster has been reported [1]. The formation of the hexagonal Cr clusters at low temperature

implies that the system will be stabilized by contracting the bond distance within the antiferromagnetic interaction to strengthen the hexagonal Cr cluster, which would induce positive thermal expansion. Then, the results of the thermal expansion measurements can be interpreted as the effect of the hexagonal Cr cluster overwhelming the effect of the NTE below 45 K. This idea provides a key to clarifying the formation mechanism of the hexagonal Cr clusters. Since the phonon mode related to the NTE continues to soften below 45 K [5, 6, 7], other perturbations may significantly affect the Cr ions in the hexagonal Cr cluster. Recently, Conlon and Chalker [18] have suggested that further neighbor interactions beside an antiferromagnetic nearest neighbor interaction are important for the formation of spin cluster. However, because the NTE expands the distance between the Cr ions, exchange interactions between the Cr ions may be weaken with the decrease in temperature. It indicates that other perturbations (*e.g.*, quantum fluctuations, Dzyaloshinskii-Moriya interaction, etc.) are also intimately deeply related to the formation of the hexagonal Cr clusters. Thus, this result suggests that other perturbations should be taken into account for future theory of the formation mechanism of the spin cluster.

4.3.4 Pressure dependence of the transition temperature

The magnetostructural transition at T_N induces the large jump in $\Delta L/L_0$, and an extremely sharp peak appears in α. The pressure dependence of T_N is calculated from the Clausius-Clapeyron relation. Taking the baselines as shown in the insets of Figs. 4(a) and 4(b) gives $\Delta V = 2.2 \times 10^{-8}\ \mathrm{m^3\ mol^{-1}}$ and $\Delta S = 3.2\ \mathrm{J\ K^{-1}\ mol^{-1}}$, which lead to $dT_N/dp = 6.9\ \mathrm{K/GPa}$. On the other hand, the result of the susceptibility measurement under pressure shows $dT_N/dp \sim 0.7\ \mathrm{K/GPa}$, which is about a tenth of the

present result [19].

The validity of the present result is confirmed from the following discussion. ΔV can be roughly estimated from the change of the lattice constant. In the cubic phase at $10\ \mathrm{K} > T_\mathrm{N}$, the reported lattice constant is 8.58882 Å [1, 20]. In the tetragonal phase at $6\ \mathrm{K} < T_\mathrm{N}$, no lattice constants have been reported, but Kim *et al.* [20] have reported the nearest neighbor Cr-Cr distances of 3.034 and 3.040 Å for the *ab*-plane and along the *c*-axis, respectively. Assuming that the fractional coordinates of atoms are scarcely changed across the transition [21], ΔV is estimated to be $\sim 3 \times 10^{-8}\ \mathrm{m^3\ mol^{-1}}$, which is close to the present measurements ($\Delta V = 2.2 \times 10^{-8}\ \mathrm{m^3\ mol^{-1}}$). On the other hand, ΔS cannot be 10 times larger than the estimated value because of the limitation of the total entropy change for the transition. These indicate that the discrepancy between the present result and that of Ref. [19] is intrinsic.

The dT_N/dp of $CdCr_2O_4$ derived from thermodynamic relations corresponds to the value at zero magnetic field and ambient pressure, in contrast that the susceptibility measurements in Ref. [19] was carried out under 1 T and at high pressures. Indeed, a complex change of dT_N/dp depending on the magnetic field and pressure is observed in $ZnCr_2O_4$ shown in Fig. 4.5 [22], which has strong spin-lattice coupling and undergoes a similar magnetostructural transition as in $CdCr_2O_4$. In particular, T_N of $ZnCr_2O_4$ is strongly affected by magnetic field at low pressures. The difference in T_N between ambient pressure and 0.35 GPa increases several times with increasing magnetic field from 0 to 1 T. Thus, a similar effect of the magnetic field on T_N is expected in $CdCr_2O_4$ at low pressures.

However, the magnetic field effect shows the opposite tendency between $CdCr_2O_4$ and $ZnCr_2O_4$; with increasing the magnetic field, the dT_N/dp of $CdCr_2O_4$ is reduced,

while the dT_N/dp of $ZnCr_2O_4$ is increased. The difference may be related to the opposite tetragonal distortion of $CdCr_2O_4$ with the elongated *c*-axis [1] compared to $ZnCr_2O_4$ with the contracted *c*-axis [10] at T_N. Further research on the detailed effects of the magnetic field and pressure could help to clarify the reason of the opposite tetragonal distortion.

4.4 CONCLUSION

The effect of the magnetic frustration on the thermal expansion behavior in $CdCr_2O_4$ has been investigated by means of thermal expansion and heat capacity measurements. Magnetic susceptibility and heat capacity measurements confirmed that the antiferromagnetic interaction is developed below 150 K. Below this temperature, the unusual thermal expansion behavior was revealed; with decreasing temperature from 150 K, negative thermal expansion behavior was observed down to 45 K, and then positive thermal expansion returned without a phase transition. This behavior suggests the competition between the bond expansion effect from the geometrical frustration and the bond contraction effect from the hexagonal antiferromagnetic cluster. In addition, this result provided an idea for that a certain perturbation except exchange interactions may be needed to form antiferromagnetic hexagonal spin clusters. The pressure dependence of the magnetostructural transition temperature indicates that the magnetic field and pressure induce the opposite effect from $ZnCr_2O_4$. This difference might be related to the opposite structural distortion at T_N.

(a)

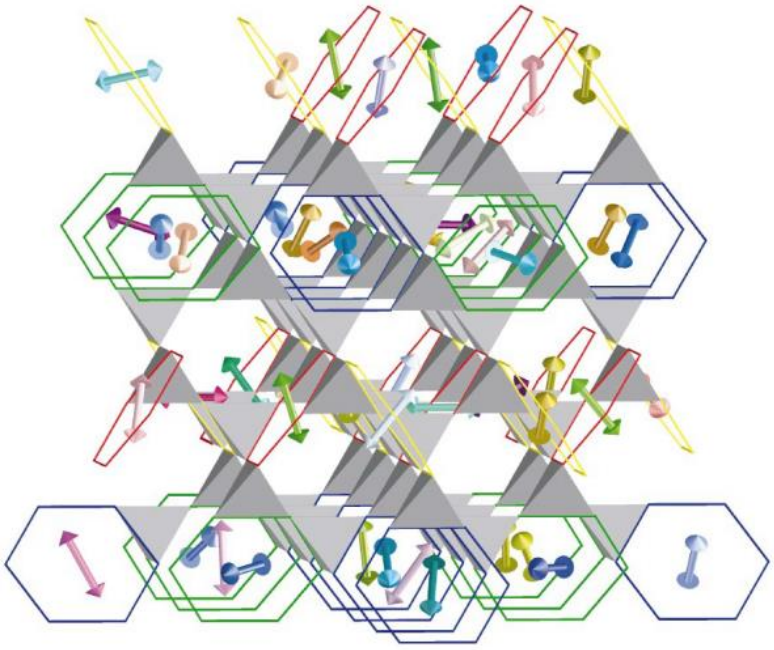

(b)

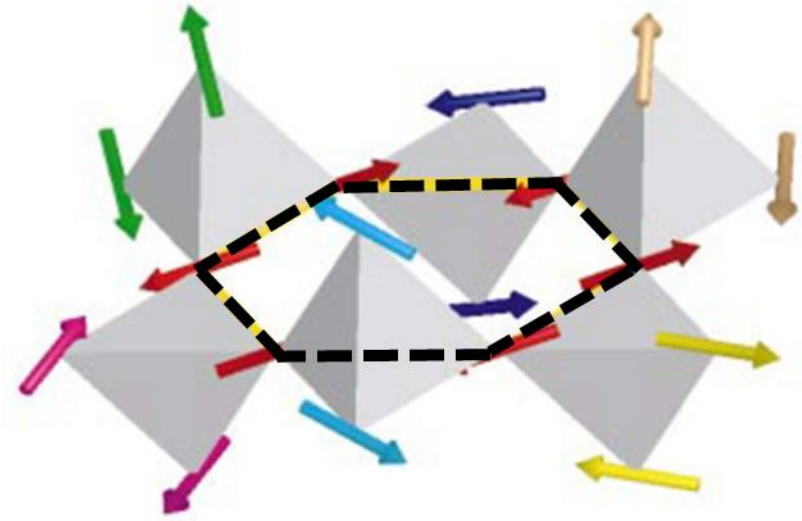

Fig. 4.1. Antiferromagnetic spin cluster formed in the spin-liquid state, taken from Ref. [2].

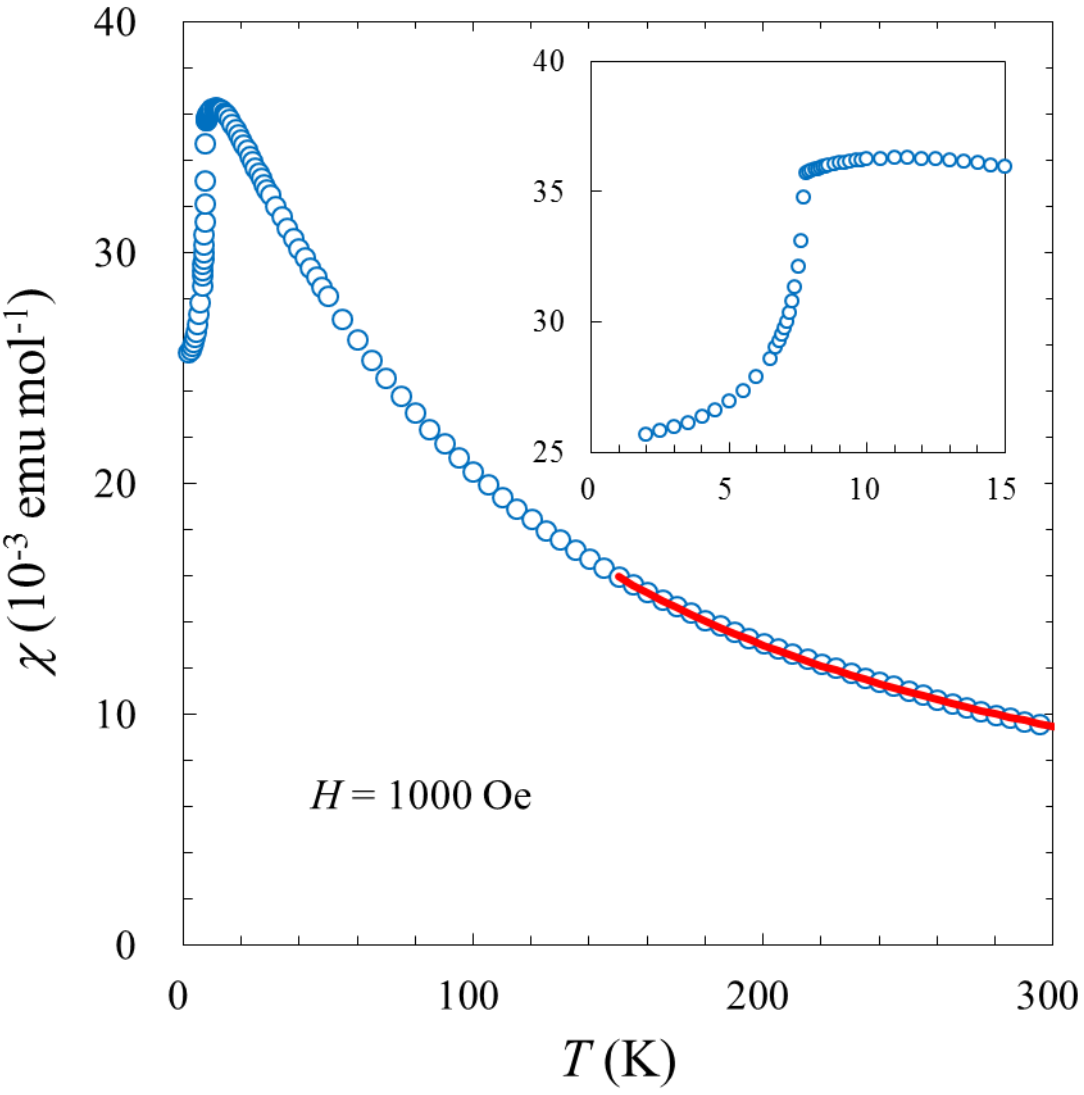

Fig. 4.2. Temperature dependence of the bulk susceptibility χ. The red line shows the result of the Curie-Weiss fit. The inset shows the χ in the vicinity of the magnetostructural transition T_N.

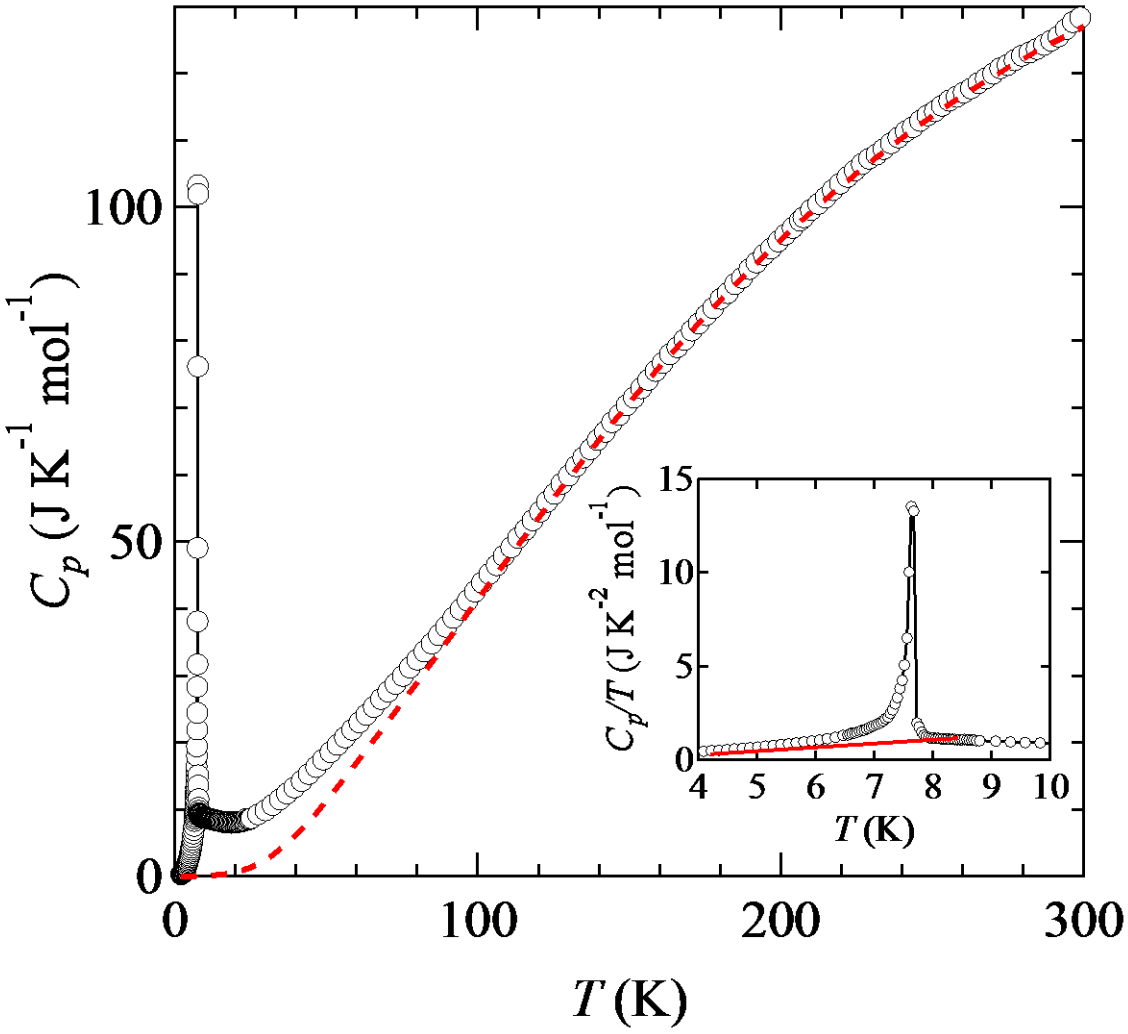

Fig. 4.3. Heat capacity C_p of $CdCr_2O_4$.The dashed line shows the lattice heat capacity calculated by scaling of the heat capacity of $ZnGa_2O_4$. The inset shows the vicinity of the magnetostructural transition at $T_N = 7.8$ K. The line is used to obtain the excess contribution.

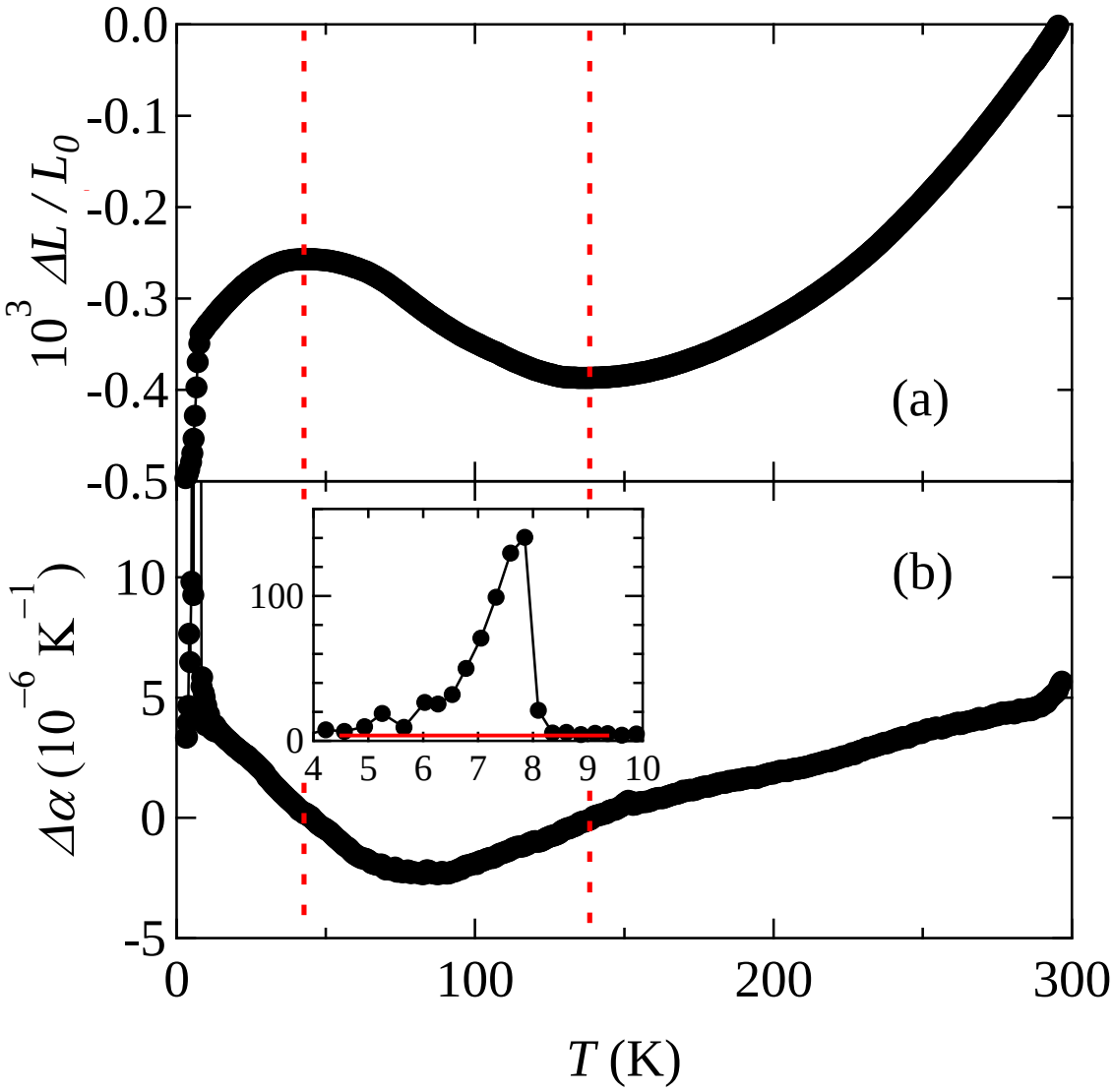

Fig. 4.4. (a) The temperature dependence of the thermal expansivity $\Delta L/L_0$ of $CdCr_2O_4$. Negative thermal expansion is seen in the temperature range from 140 K to 45 K. (b) The thermal expansion coefficient α of $CdCr_2O_4$. The inset in the lower frame shows α of the vicinity of the magnetostructural transition at $T_N = 7.8$ K where the line is used to calculate the excess contribution.

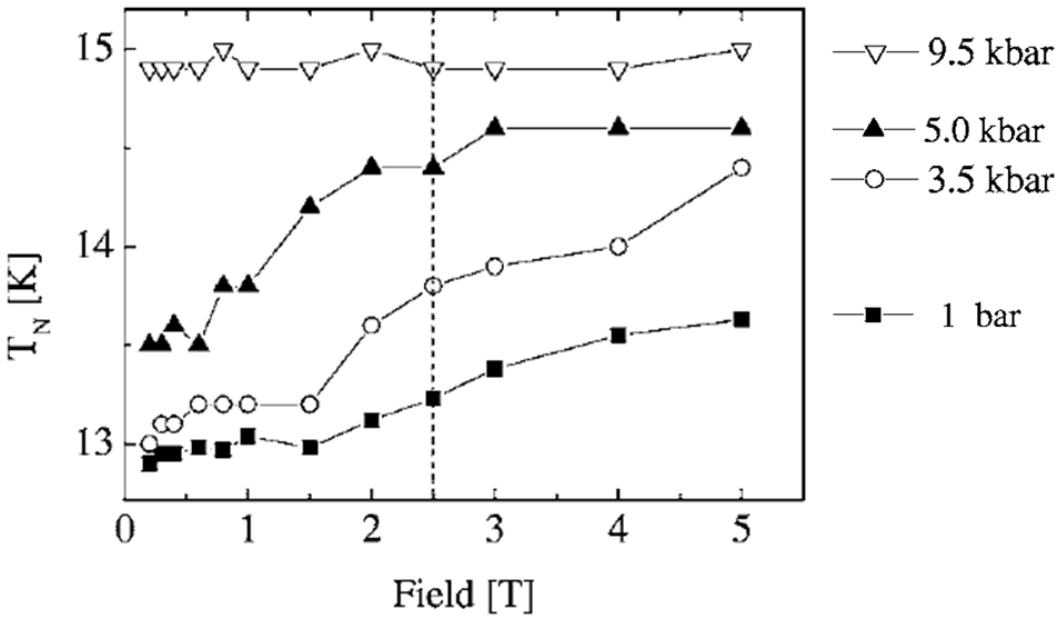

Fig. 4.5. Magnetic field and pressure dependence of the magnetstructural transition temperature TN of $ZnCr_2O_4$, from Ref. [22].

References

[1] J.-H. Chung, M. Matsuda, S.-H. Lee, K. Kakurai, H. Ueda, T. J. Sato, H. Takagi, K.-P. Hong, and S. Park, Phys. Rev. Lett. **95**, 247204 (2005).

[2] S.-H. Lee, C. Broholm, W. Ratcliff, G. Gasparovic, Q. Huang, T. H. Kim, and S.-W. Cheong, Nature (London) **418**, 856 (2002).

[3] A. B. Sushkov, O. Tchernyshyov, W. Ratcliff, II, S. W. Cheong, and H. D. Drew, Phys. Rev. Lett. **94**, 137202 (2005).

[4] R. Valdés Aguilar, A. B. Sushkov, Y. J. Choi, S.-W. Cheong, and H. D. Drew, Phys. Rev. B **77**, 092412 (2008).

[5] T. Rudolf, Ch. Kant, F. Mayr, J. Hemberger, V. Tsurkan, and A. Loidl, New J. Phys. **9**, 76 (2007).

[6] O. Tchernyshyov, R. Moessner, and S. L. Sondhi, *et al*., Phys. Rev. B **66**, 064403 (2002).

[7] Ch. Kant, J. Deisenhofer, T. Rudolf, F. Mayr, F. Schrettle, A. Loidl, V. Gnezdilov, D. Wulferding, P. Lemmens, and V. Tsurkan, Phys. Rev. B **80**, 214417 (2009).

[8] S.-H. Lee, C. Broholm, T. H. Kim, W. Ratcliff, II, and S-W. Cheong, Phys. Rev. Lett. **84**, 3718 (2000).

[9] M. Matsuda, M. Takeda, M. Nakamura, K. Kakurai, A. Oosawa, E. Lelièvre-Berna, J.-H. Chung, H. Ueda, H. Takagi, S.-H. Lee, Phys. Rev. B **75**, 104415 (2007).

[10] G.-W. Chern, C. J. Fennie, and O. Tchernyshyov, Phys. Rev. B **74**, 060405(R) (2006).

[11] H. A. Dabkowska, J. Cryst. Grow. **54**, 607 (1981).

[12] Z. Yan, and H. Takei, J. Cryst. Grow. **171**, 131 (1997).

[13] M. Rotter, H. Müller, E. Gratz, M. Doerr, and M. Loewenhaupt, Rev. Sci. Instrum. **69**, 2742 (1998).

[14] K. Mizushima, *Master Thesis*, Tokyo Institute of Technology (2010).

[15] M. Tachibana, N. Taira, and H. Kawaji, Solid Stat. Commun. **151**, 1776 (2011).

[16] J. Hemberger, H.-A. Krug von Nidda, V. Tsurkan, and A. Loidl, Phys. Rev. Lett. **98**, 147203 (2007).

[17] C. J. Fennie, and K. M. Rabe, Phys. Rev. Lett. **96**, 205505 (2006).

[18] P. H. Conlon, and J. T. Chalker, Phys. Rev. B **81**, 224413 (2010).

[19] H. Ueda, and Y. Ueda, Phys. Rev. B **77**, 224411 (2008).

[20] J.-H. Kim, M. Matsuda, H. Ueda, Y. Ueda, J.-H. Chung, S. Tsutsui, A. Q. R. Baron, and S.-H. Lee, J. Phys. Soc. Jpn. **80**, 073603 (2011).

[21] S.-H. Lee, H. Takagi, D. Louca, M. Matsuda, S. Ji, H. Ueda, Y. Ueda, T. Katsufuji, J.-H. Chung, S. Park, S.-W. Cheong, and C. Broholm, J. Phys. Soc. Jpn. **79**, 011004 (2010).

[22] Y. Jo, J.-G. Park, H. C. Kim, W. Ratcliff, II, and S-W. Cheong, Phys. Rev. B **72**, 184421 (2005).

Chapter 5

Lattice behavior in the conical spin state of $CoCr_2O_4$

5.1 INTRODUCTION

This chapter has treated the cubic spinel oxides $CoCr_2O_4$, in which the tetrahedral *A* site is occupied by the magnetic ion Co^{2+} ($e^4\ t_2^3$) and the octahedral *B* site by the magnetic ion Cr^{3+} ($t_{2g}^3\ e_g^0$). The dominant exchange interaction is an antiferromagnetic nearest neighbor interaction between Cr^{3+} ions due to the direct overlap of t_{2g} orbitals. As opposed to the previous spinels, there are additional nearest neighbor interactions between Co^{2+} ions, and between Co^{2+} and Cr^{3+} ions, which lead to a complex magnetism in $CoCr_2O_4$. The ground-state spin structure of spinels was theoretically analyzed by Lyons, *et al*. in 1962 using the Heisenberg model with the two exchange interactions J_{AB} and J_{BB} [1]. The model, called the "LKDM theory", predicts that the ground state depends on the parameter *u*, defined as $u = 4J_{BB}S_B/3J_{AB}S_A$, where S_A and S_B are the quantum number of the *A* ion and *B* ion, respectively. For $u<8/9$, the *A*-site spins align parallel to each other, and they are antiparallel to the *B*-site spins, resulting in the Néel state. For $8/9<u<1.3$, the ferrimagnetic spiral long-range order arises. For $u<1.3$, the magnetic structure will be locally unstable, and a short-range order will be established. The neutron scattering experiments have found $u=2$ [2], indicating that any magnetic ground state of $CoCr_2O_4$ should be unstable.

Indeed, complex magnetic transitions are observed in $CoCr_2O_4$ [3]. First, a

ferrimagnetic transition occurs at $T_C = 93$ K. With further decreasing temperature, a conical spin state with an incommensurate wave vector $\boldsymbol{Q}$ ~ (0.63, 0.63, 0) is formed at $T_S = 26$ K, which is accompanied by spontaneous electric polarization. Finally, a lock-in transition occurs at $T_L \sim 13$ K with a slight change in $\boldsymbol{Q}$. The magnetic structure in the ground state was determined to be the conical spin structure as shown in Fig. 5.1 [3, 4]. The Co spins on the *A*-site have one magnetic sub-lattice, while the Cr ions on the *B*-site make two magnetic sub-lattice. Each of them forms the conical spin structure with same spiral wave vector $\boldsymbol{Q}$ and different cone angles.

For the conical spin state, some different behaviors have been reported [2, 4, 5, 6, 7]. The strong sample dependent could be attributed to the Cr-site mixing, which is confirmed by Ref. [8], comparing the samples prepared by the chemical vapor method and flux method. The sample grown by a chemical vapor method has no site disorder and exhibits the same behavior as Ref. [3]. Flux grown samples show the incorporation of the Co ion into the Cr site. The ferrimagnetic and conical spin transition temperatures of the samples are decreased and the lock-in transition is faded away. These changes are qualitatively same with the previous reports.

The current interest in $CoCr_2O_4$ has been focused on a "multiferroic" property originated from the conical spin configuration [3, 7, 8]. The multiferroicicty originally refers to the state that possesses more than one ferroic properties, such as ferromagnetism and ferroelectricity, though it includes the state with a magnetic ordering and ferroelectricity. Why the multiferroicity is so attractive is that it can realize the magnetoelectric effect, modulating the magnetization by an electric field and the polarization by a magnetic field. The magnetoelectric effect was first predicted by Pierre Curie in 19th century [9], and a century later, multiferroicity has been attracted renewed

attention due to the discovery of the practicable magnetoelectric effect in the frustrated magnets $TbMnO_3$ [10], $TbMn_2O_5$ [11], and $Ni_3V_2O_8$ [12]. They are, however, antiferromagnet, resulting in no spontaneous magnetization. Then, $CoCr_2O_4$ has been appeared as the first material with spontaneous magnetization and magnetically-induced ferroelectricity. The magnetically-induced ferroelectricity below T_S can be explained by the spin-current model [13] or inverse Dzyaloshinskii-Moriya model [14], where a spiral spin configuration induces an electric polarization.

In the present study, the interplay between spin and lattice degrees of freedom on the $CoCr_2O_4$ was investigated by the heat capacity and the thermal expansion measurements. The mechanism of the multiferroicity is definitely related to both spin and lattice degrees of freedom. Although $CoCr_2O_4$ have been focused on the multiferroic property, detailed thermal expansion data have not been reported. The thermal expansion will provide the insights on the degree of distortion of the lattice through the conical spin transition and lock-in transition. Furthermore, the combination of the thermal expansion and heat capacity data can lead to the useful information in the phase stability.

5.2 EXPERIMENTAL

Single crystals of $CoCr_2O_4$ were grown by a chemical vapor transport technique with $CrCl_3$ as the transport agent. Magnetic susceptibility measurements were carried out by Quantum Design MPMS. Heat capacity was measured by the relaxation technique using a Quantum Design physical property measurement system (PPMS) for the temperature range from 2 to 300 K. Thermal expansion measurements were carried out with a capacitance dilatometer constructed from silver [15]. The specimens, which

were the same samples used for the heat capacity measurement were measured along the cubic <111> direction with the length of 1.05 mm for $CoCr_2O_4$. Thermal expansivity data $\Delta L/L_0$ ($\Delta L = L - L_0$; L_0 refers to the value at 293 K) were taken on heating direction with a rate of 1 K/min between 2 and 300 K. Magnetocaloric effect (MCE) measurements were performed in pulsed high magnetic field with the 55-T magnet (duration: 36 ms) at the Institute for Solid State Physics, the University of Tokyo. To measure accurately the sample temperature, which dynamically varies with changing magnetic field, an Au-Ge thin film was directly deposited on the sample surface and used as the thermometer.

5.3 RESULTS AND DISCUSSION

5.3.1 Magnetic susceptibility

Figure 5.2(a) shows the magnetization below 120 K under 1000 Oe, which exhibits the three distinct transition behavior being consistent with Ref. [3, 7]. The strong upturn at T_C=94 K arises from the ferrimagnetic transition. Two jumps in the lower temperature region are attributed to the formation of the conical spin ordering at T_S=26 K and the lock-in transition at T_L=13 K. A linear fit to the experimental data between 150 K and 300 K yields a Curie-Weiss temperature Θ_{CW} = −575 K, and an effective magnetic moment p_{eff} = 7.43 μ_B/f.u. The obtained p_{eff} is larger than the theoretical spin-only value of p_s = 6.71 μ_B/f.u. Instead, the value is rather close to the value expected for the unquenched orbital contribution from Co^{2+} ion, $p = \sqrt{4S(S+1) + L(L+1)} = 7.55\mu_B/\mathrm{f.u.}$ This is unexpected for the Co^{2+} ion in a tetrahedral coordination, though the low-lying excited state ($e^3\ t_2^4$) could be the origin

for this difference [16]. The magnetic field dependence of the magnetization is presented in Fig. 5.2(b), where the spontaneous magnetization M_S = 0.07 μ_B/f.u. can be confirmed. The magnetization value at 0.5 T is about 0.1 μ_B/f.u., which is consistent with the report of the sample without the site-disorder showing M=0.09 μ_B/f.u. at 0.5 T. Thus, the sample used in this study has little Cr-site mixing, because the Co mixing changes the effective moment due to the non-magnetic Co^{3+} ion at the octahedral site ($t_{2g}^6\ e_g^0$).

5.3.2 Heat capacity

The heat capacity C_p of $CoCr_2O_4$ is presented in Fig. 5.3, which shows good agreement with the results of previous studies [3, 7]. The ferrimagnetic transition at T_C=93 K is found as a λ-like peak. The most striking feature is a very sharp peak at T_S=26 K due to a transition to the conical spin state. The extremely sharp peak may indicate the first-order nature of this transition. The lock-in transition at T_L~13 K shows a small change in C_p, and there is a thermal hysteresis as seen in the inset of Fig. 5.3, suggesting a first-order transition. It should be noted that there is a possibility of the underestimation of the latent heat for a first-order transition by the relaxation method. To exclude the possibility, heat capacity measurements with different thermal pulses were performed. In each measurement, there is no anomaly in the relaxation curve. The obtained heat capacity data shows little difference except for the peak temperature and heat capacity values just around the transition temperature at T_S and T_L. The transition entropies estimated from these data is the same within 10%.

It is interesting that thermal hysteresis could not be observed for the conical spin transition at T_S. In addition, the thermal expansion coefficient discussed later also

showed a second-order-like peak at T_S, as the other experiments show a second-order-like change at the conical spin transition [3, 6]. If the conical spin transition is actually a second-order transition, the critical behavior of the heat capacity near the transition can be written by the commonly used function $C^{\pm} = \left(\frac{A^{\pm}}{\alpha}\right)|t|^{-\alpha} + B + Et$, where $t = (T - T_S)/T_S$ is the reduced temperature and the superscript + (−) corresponds to $t>0$ ($t<0$). However, any fitting parameters could not describe the critical behavior using the same critical exponent α for $t>0$ and $t<0$, because of the sharp rise on the high temperature side $t>0$. Without the consideration of the regular contribution $B+Et$, the least-square fit leads to the critical exponents α^{+}=1.23 and α^{-}=0.57 as shown in Fig. 5.4. These critical exponents are extremely larger than the conventional universality classes having $\alpha = -0.133$ or -0.015 for standard *XY* or Heisenberg models [17]. It is known that the system having the chiral degrees of freedom shows relatively large critical exponents α = 0.34 and 0.24 for the chiral *XY* and Heisenberg universality classes [18], though these values are also much smaller than the present results. A extremely large value was reported for $La_{0.7}Ca_{0.3}MnO_3$ showing α = 0.93 [19], which characterized by a strong charge-lattice-spin coupling. It may suggest the possibility that in $CoCr_2O_4$ spin degrees of freedom couple to not only lattice but other degrees of freedom.

5.3.3 Thermal expansion

Figure 5.5 shows the thermal expansion coefficient α of $CoCr_2O_4$, which is obtained from the high-resolution linear thermal expansivity $\Delta L/L_0$ data shown in the inset. At T_C, α shows a λ-like peak as in C_p. The λ shape of the peak is due to

short-range fluctuations, which is typical for a second-order transition. With further decrease in temperature, an upturn begins below 50 K, and large peaks are found at T_S and T_L. In contrast to the results of C_p, the lock-in transition at T_L exhibits a large peak representing significant lattice distortion.

The upturn below 50 K is considered to be related to the development of spiral short-range order observed in inelastic neutron scattering experiments [4]. The spiral short-range order characterizes the conical spin structure below 26 K, which suggests that the growth of the short-range order should relate to the conical spin transition at 26 K. The spiral short-range order apparently grows below 50 K. Accordingly, some sign of the conical spin transition could be appeared up to 50 K. Indeed, Lawes *et al.* [20] reported anomalous dielectric behavior around 50 K, which was attributed to the development of the spiral short-range order. That is because dielectric properties could be affected by the spiral spin structure breaking spatial inversion symmetry. The spiral spin structure also induces with strong spin-lattice coupling through inverse Dzyaloshinsky-Moriya interaction. Thus, it is natural to consider that the upturn of the thermal expansion coefficient below 50 K correlates to the development of the spiral short-range order. This indicates that the effects of the conical spin transition are over a wide temperature range. Furthermore, the shape of the transition peak seems to be a second-order transition rather than a first-order transition.

5.3.4 Pressure dependence of transition temperatures

The pressure dependence of each transition temperature in $CoCr_2O_4$ was calculated using the baselines shown in Figs. 5.3 and 5.5. For the second-order ferrimagnetic transition at T_C, the pressure dependence of the transition temperature dT_C/dp can be

evaluated from the Ehrenfest relation $dT_C/dp = \Delta\beta V_m T_C/\Delta C_p$, where $V_m = 4.4 \times 10^{-5}$ m^3 mol^{-1} is the molar volume [21], $\Delta\beta = 3\Delta\alpha$ is the jump in volume thermal expansion coefficient at T_C, and ΔC_p is the jump in C_p at T_C. The result $dT_C/dp = 2.6$ K/GPa, estimated from $\Delta C_p = 10.5$ J K^{-1} mol^{-1} and $\Delta\alpha = 2.2 \times 10^{-6}$ K^{-1}, is in good agreement with 2.5 K/GPa obtained from the magnetic induction method measured between 0 and 1.15 GPa [22].

For the transition to the conical spin state at T_S, dT_S/dp can be calculated from the Clausius-Clapeyron relation $dT_S/dp = \Delta V/\Delta S$ with assuming the first-order transition, where ΔV and ΔS denote the change in volume and entropy at the transition. The integration of the anomalies $\Delta V = V_m \int 3\Delta\alpha(T)dT$ and $\Delta S = \int [\Delta C_p(T)/T] dT$ leads to $\Delta V = 3.1 \times 10^{-9}$ m^3 mol^{-1} and $\Delta S = 5.0$ J K^{-1} mol^{-1}, which results in $dT_S/dp = 0.62$ K/GPa. The baselines for the transition at T_S are estimated by drawing a line between 18 K to 40 K considered as clearly appearing the effect of the transition on C_p and α data, which is a method generally used for estimating a baseline of a first-order transition. Although the baselines for the transition at T_S have a little arbitrary, the validity can be supported from the following reasons. Below 40 K, the correlation length of the short-range order apparently increases with decreasing error bar [4]. In addition, the minimum value in C_p/T is approximately 40 K. On the other hand, the correlation length below the conical spin transition temperature 26 K increases with decreasing temperature, and almost saturates at about 15 K. Moreover, the alpha data between $T_L < T < T_S$ show a minimum value at 18 K. In the case of the second-order transition, the dT_S/dp can be evaluated from the Ehrenfest relation. Taking the same baseline in the case of the first-order gives $\Delta C_p = 52.8$ J K^{-1} mol^{-1} and $\Delta\alpha = 6.31 \times 10^{-6}$ K^{-1}, which leads to $dT_S/dp = 0.40$ K/GPa. Both values are quantitatively

equivalent with each other obtained by assuming first-order and second-order.

For the first-order lock-in transition at T_L, dT_L/dp was calculated to be $dT_L/dp = 80$ K/GPa using the Clausius-Clapeyron relation with $\Delta V = 1.3 \times 10^{-9}$ m^3 mol^{-1} and $\Delta S = 1.7 \times 10^{-2}$ J K^{-1} mol^{-1}. There is no published data for the pressure dependence of T_S and T_L.

The positive values for all of the pressure dependence of the transition temperature in $CoCr_2O_4$ indicate that low-temperature phases prefer a smaller volume. The small values of dT_C/dp and dT_S/dp indicate a weak influence of volume change to the phase stability. On the other hand, the large value of dT_L/dp implies that the incommensurate (IC) phase between $T_L < T < T_S$ is highly sensitive for pressure. Thus, a small difference in atomic distances due to a slightly different sample quality may be the origin of confusion in reports such as various spin structures below T_S [2, 4, 5, 6, 7] and the different behavior of the multiferroic property at the lock-in transition [3, 7].

An IC phase is often found in systems with strong competition between exchange interactions as seen in $CoCr_2O_4$. An IC phase due to strong magnetic competition is also observed in multiferroic compounds RMn$_2$O$_5$ (R = Ho, Dy, and Tb) [23] and $MnWO_4$ [24] , which have strong spin-lattice coupling. With decreasing temperature from the IC phase, a lock-in transition is generally found. In RMn$_2$O$_5$ and $MnWO_4$, the linear expansion anomalies at the lock-in transition are highly anisotropic [23, 24]; the axis with the change of a magnetic modulation shows a large expansion anomaly, and the other axis shows a relatively small expansion anomaly. These behaviors have been attributed to the strong spin-lattice coupling. From this point of view, the thermal expansion at the lock-in transition in $CoCr_2O_4$ should correspond to the magnetic modulation characterized by a wave vector $\boldsymbol{Q} \sim (q, q, 0)$ [3], since the large value of

dT_L/dp indicates that the spin couples considerably to the lattice. The present result may imply the possibility of the reduction of lattice symmetry from cubic at the lock-in transition. Although $CoCr_2O_4$ is believed to remain cubic in its ground state [3, 6, 25], a small signature of mode splittings in the infrared spectra has been reported [25].

5.3.5 Magnetocaloric effects under pulsed magnetic field

The representative MCEs for magnetic field along the [111] and [001] axis are displayed in Fig. 5.6(a) and 5.6(b), respectively. Both cases showed roughly similar response for the magnetic field, except for the low temperature and high magnetic field region. The MCE curves at 30 K showed a reversible trace between field-increasing and -decreasing processes, indicating negligible heat exchange to the surroundings and fast response in the thermometer, which supports the validity of the present results. Around T_S = 26 K, the present measurements could not find any sign of magnetic field dependence of the conical spin transition up to 55 T, which means an extremely small dT_S/dH. It is interesting that the combination of two Clausius-Clapeyron relations with dT_S/dp and dT_S/dH leads to a large value of $\Delta V/\Delta M$, and hence a considerable magnetostriction is expected at T_S.

Further decreasing temperature, a small hysteresis was observed at high magnetic fields, which could be attributed to the lock-in transition. This transition is of a first-order, so the trace at zero field exhibited a small discrepancy between the initial and final state. The smallness suggests that a small latent heat is released at the lock-in transition, which is consistent with the tiny peak in the zero field heat capacity shown in the inset of Fig. 5.3. At lower temperature, another transition behavior besides the lock-in transition became to be observable at higher fields. The sample temperature was

considerably increased from the conical spin state to the high field phase (HFP). Below T_L, the transition field gradually increased with decreasing temperature. Once entering the HFP, the HFP continued metastable down to 10 T, and it did not to recover the ground state at zero field due to the strong exotherm. The phase diagrams obtained for H||[111] and H||[001] are shown in Figs. 5.7(a) and 5.7(b), respectively.

The large temperature increase at the HFP transition is related to the significant release of entropy. Because the lattice entropy has almost vanished in this temperature range, the released entropy should be of magnetic origin. In the heat capacity measurements, the significant entropy change could be seen in the conical spin transition, which provides a simple idea that the conical spin configuration is broken at the HFP transition. For the HFP, the results of the ultrasound and magnetization measurements have been reported [26]. At the HFP transition, a step-like anomaly is observed in the ultrasound experiments, while the magnetization did not exhibited any anomaly, which suggests the structural phase transition. With the assumption of a lowering of the lattice symmetry in the conical spin state due to the inverse DM interaction, Ref. [26] speculated on the measurements results that while the longitudinal component of the magnetization keeps a collinear long-range order, the transverse spiral components are broken, leading to the disappearance of the inverse DM interaction and hence a structural distortion into cubic symmetry. Based on this speculation, it is likely to agree with the present observation seen in Fig. 5.7 that the HFP transition temperature is lower in applying field along the [001] axis than along the [111] axis, though a field orientation dependence has not been reported in Ref. [26].

Then, the following question is why the diagram of the HFP has an inverted dome shape. Generally, if a phase transition has a ferromagnetic character, the application of

magnetic field leads to an increase in the transition temperature, and if a antiferromagnetic character, a decrease in the transition temperature. Because the top of the phase dome is located near 10 K, the dominant interaction changes from ferromagnetic in the IC state to antiferromagnetic in the C state. In the MCE curves, the higher initial temperatures above 10 K resulted the higher temperature at 55 T, which indicates that a ferromagnetic component drives the HFP transition. On the other hand, all curves converged to the same temperature of about 12 K for the initial temperature below 10 K, *i.e.*, finally the same magnetic state was established, which suggests that a ferromagnetic component almost independent with respect to magnetic field and a developed antiferromagnetic component is destroyed with accompanying the breakdown of the transverse spiral component. Thus, the crossover of the dominant interaction might be occurred around 10 K. Its nature is considered to be the anisotropic lattice distortion, as proposed in the section 5.3.4. This crossover would be related to the finding of the magnetic irreversibility at low temperatures [27], and the short-range magnetic ordering [7, 6].

It is finally noted that due to the strong exotherm at the HFP transition, it is hard to study physical properties in the HFP below 12 K. Even if the sample is immersed in liquid helium, a strong rise in the sample temperature (over 10 K) was confirmed.

5.4 CONCLUSION

The effect of the interplay between spin and lattice degrees of freedom in $CoCr_2O_4$ has been studied by thermal expansion and heat capacity measurements. The large pressure dependence of the lock-in transition in $CoCr_2O_4$ indicates that the spins are strongly coupled to the lattice in the incommensurate phase. Since the strong spin-lattice

coupling can induce the anisotropic expansion along the magnetic modulation vector, there may be lattice distortion below the lock-in transition. The magnetocaloric effect measurements in pulsed magnetic field up to 55 T reveals the field orientation dependence for the high field phase, which shows that the lowest transition field is of H = 30 T || [001] at 10 K. The obtained phase diagram suggests the crossover of the dominant magnetic interaction at low temperatures, which might be resulted from the anisotropic lattice distortion at the lock-in transition. In order to confirm the presence of the anisotropic lattice distortion, thermal expansion measurements for the [110] and [001] axis should be carried out in future. Furthermore, polarization measurements in pulsed magnetic field will provide a valuable insight for the high field phase because the spiral configuration might be broken and hence the polarization will be faded away.

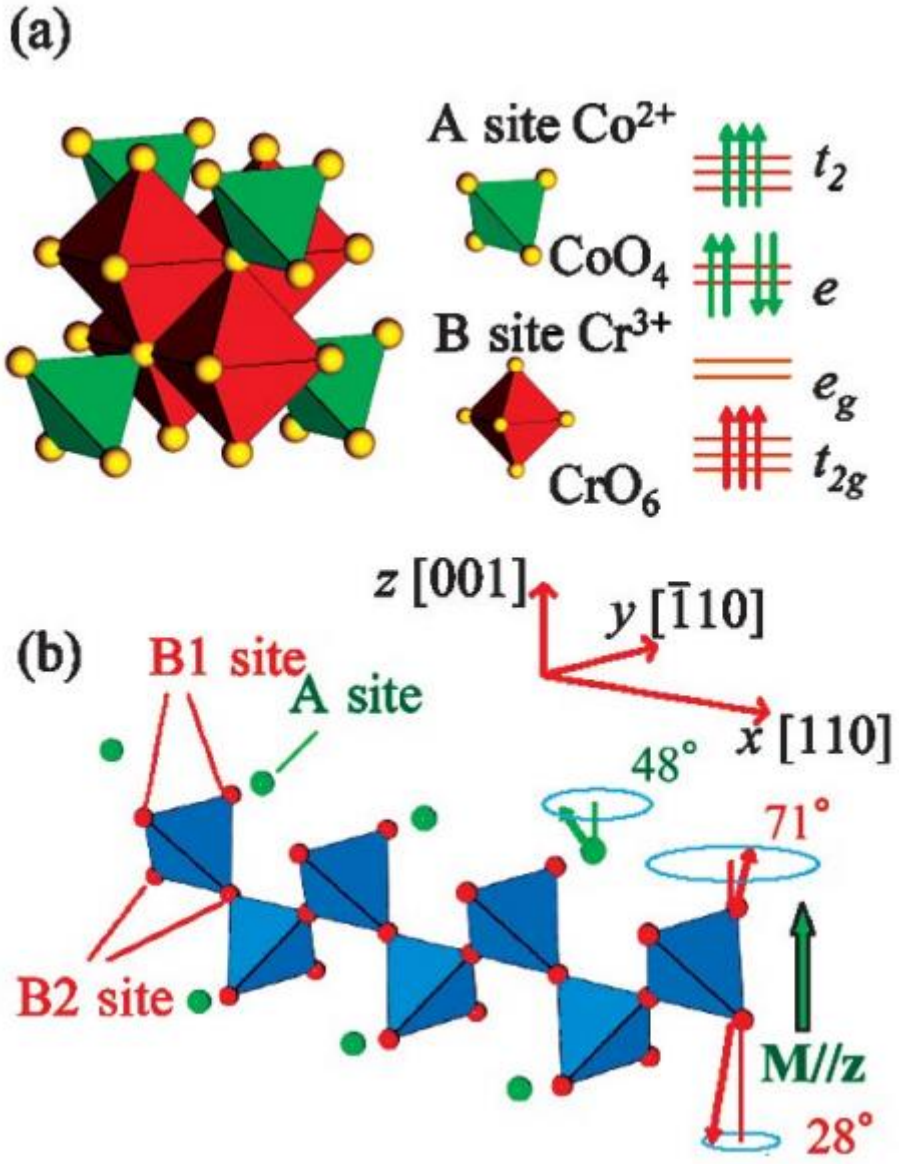

Fig. 5.1. (a) Crystal structure of $CoCr_2O_4$, and the electronic configurations of the *A*-site Co^{2+} ion and *B*-site Cr^{3+} ion. (b) The schematic view of the conical spin configuration, where the spiral wave vector propagates along the [110] direction and the polarization occurs along the [$\bar{1}$10] axis. From Ref. [3, 4].

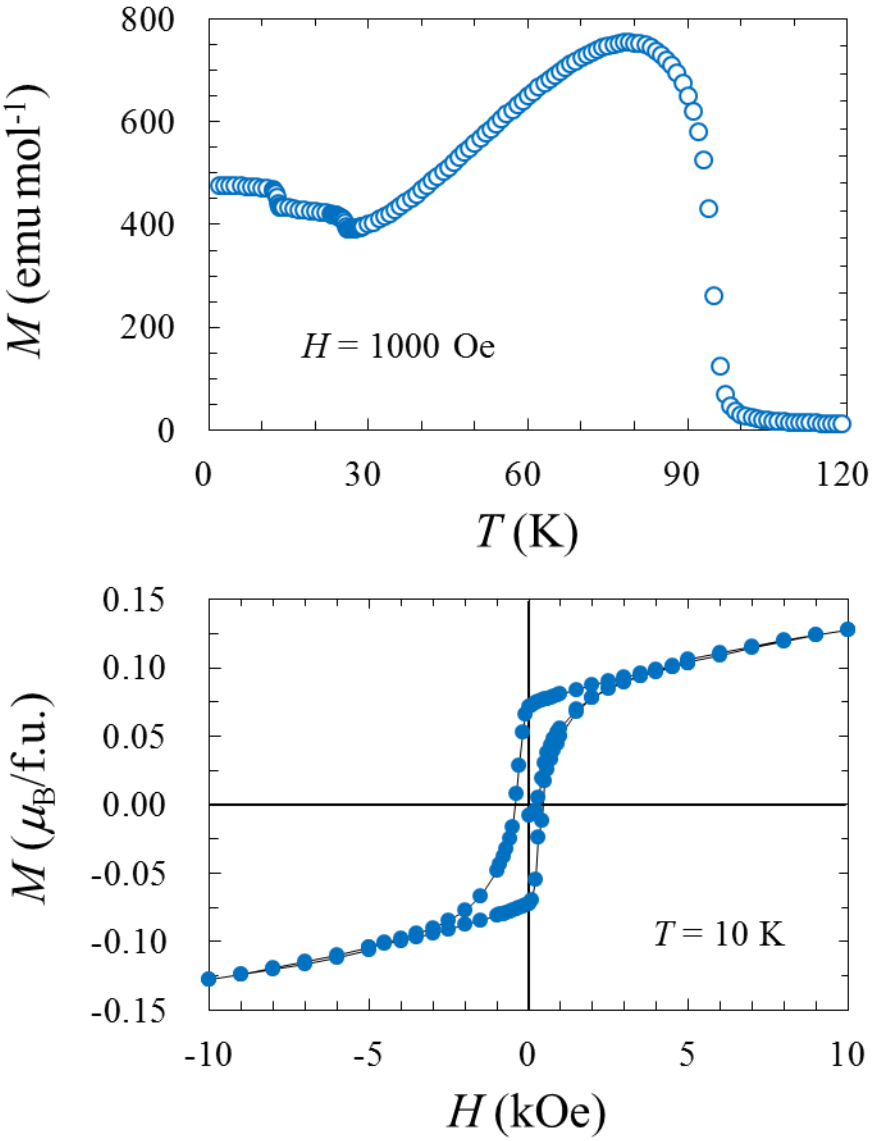

Fig. 5.2. (a) Temperature dependence and (b) field dependence of magnetization of of $CoCr_2O_4$. The black solid line is a guide for the eye.

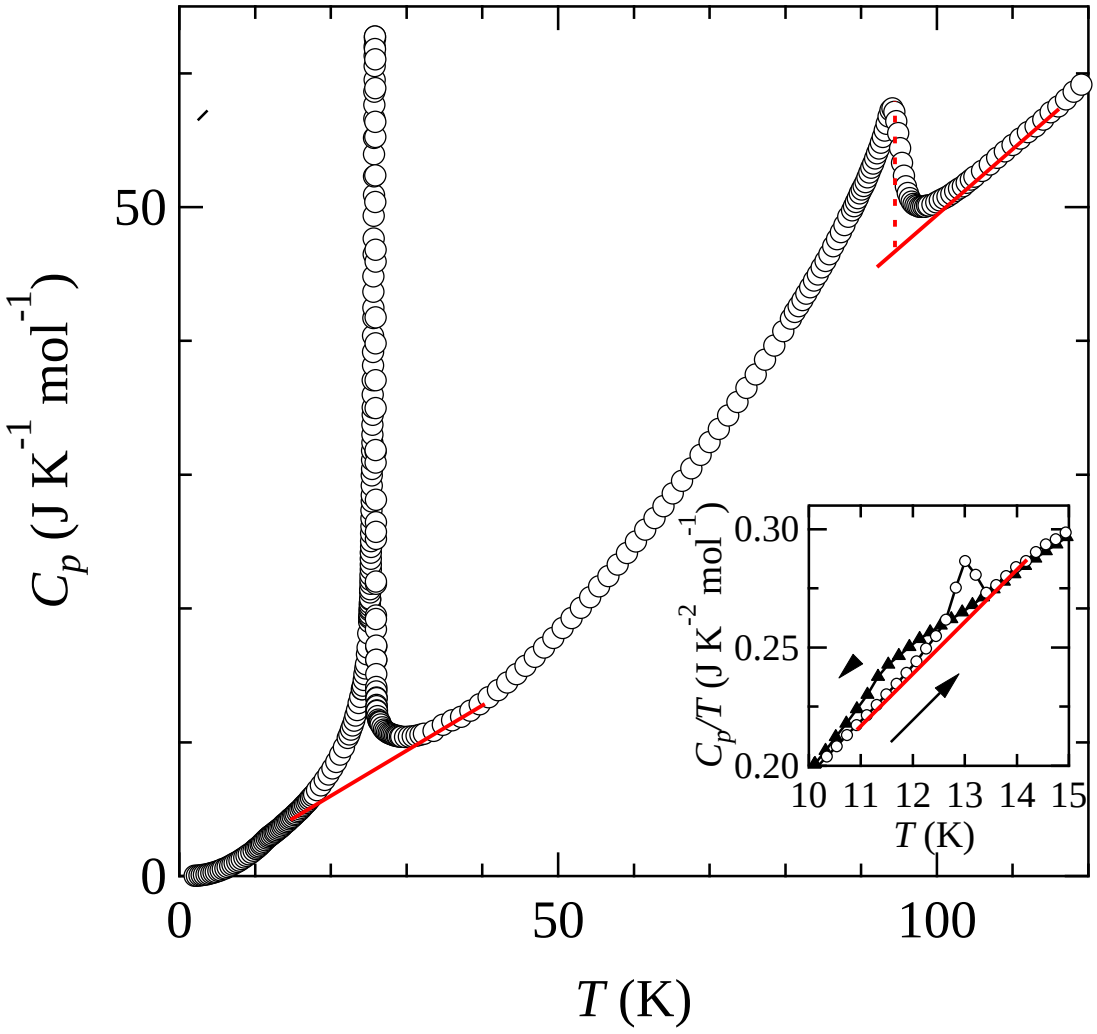

Fig. 5.3. Heat capacity C_p of $CoCr_2O_4$. The inset shows the heat capacity in the vicinity of transition temperature at the lock-in transition at $T_L = 13$ K. The red lines are used to obtain the jumps and the excess contributions in C_p.

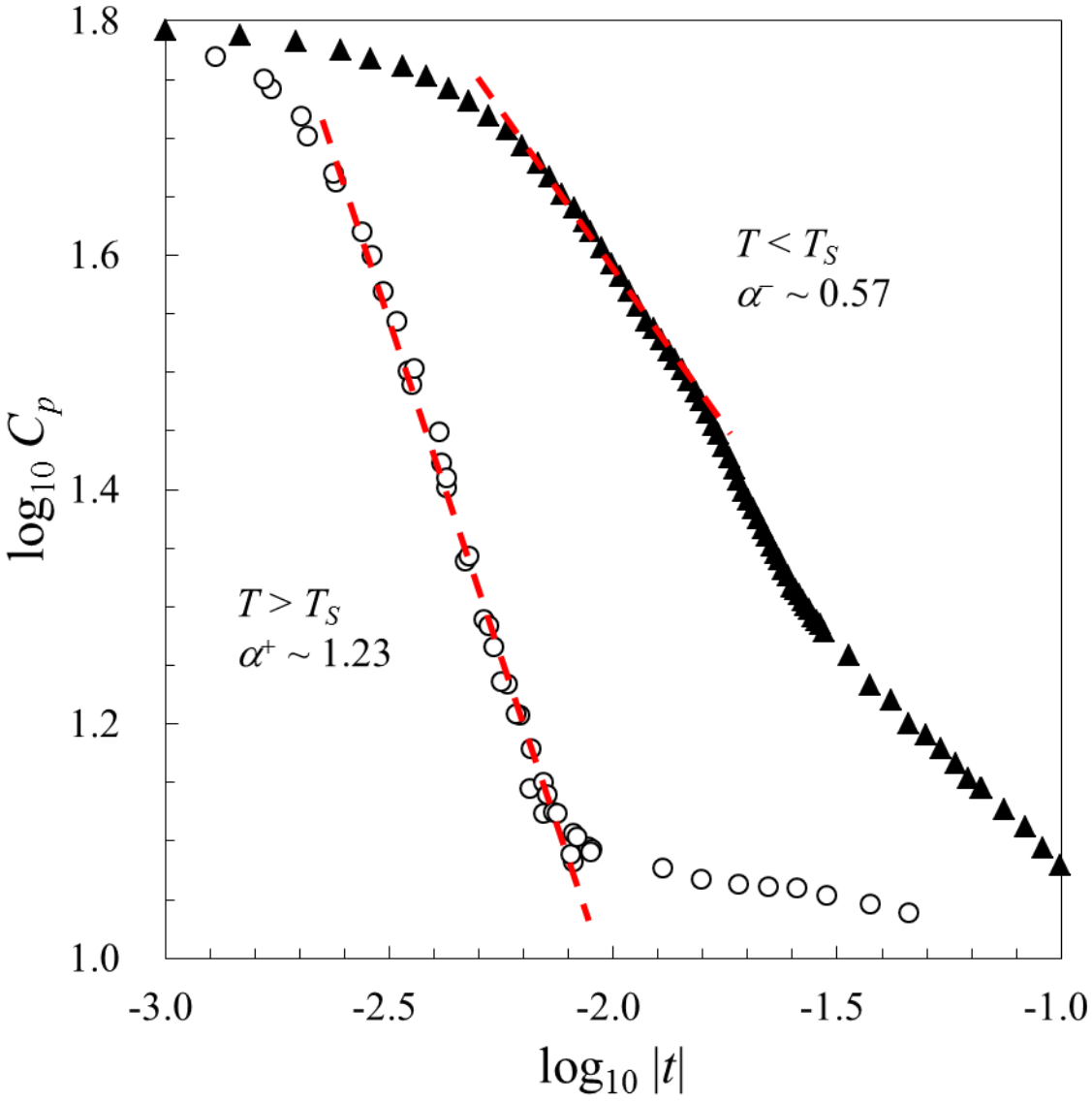

Fig. 5.4. Critical behavior above and below T_S as characterized by linear fits of heat capacity data on a log-log plot.

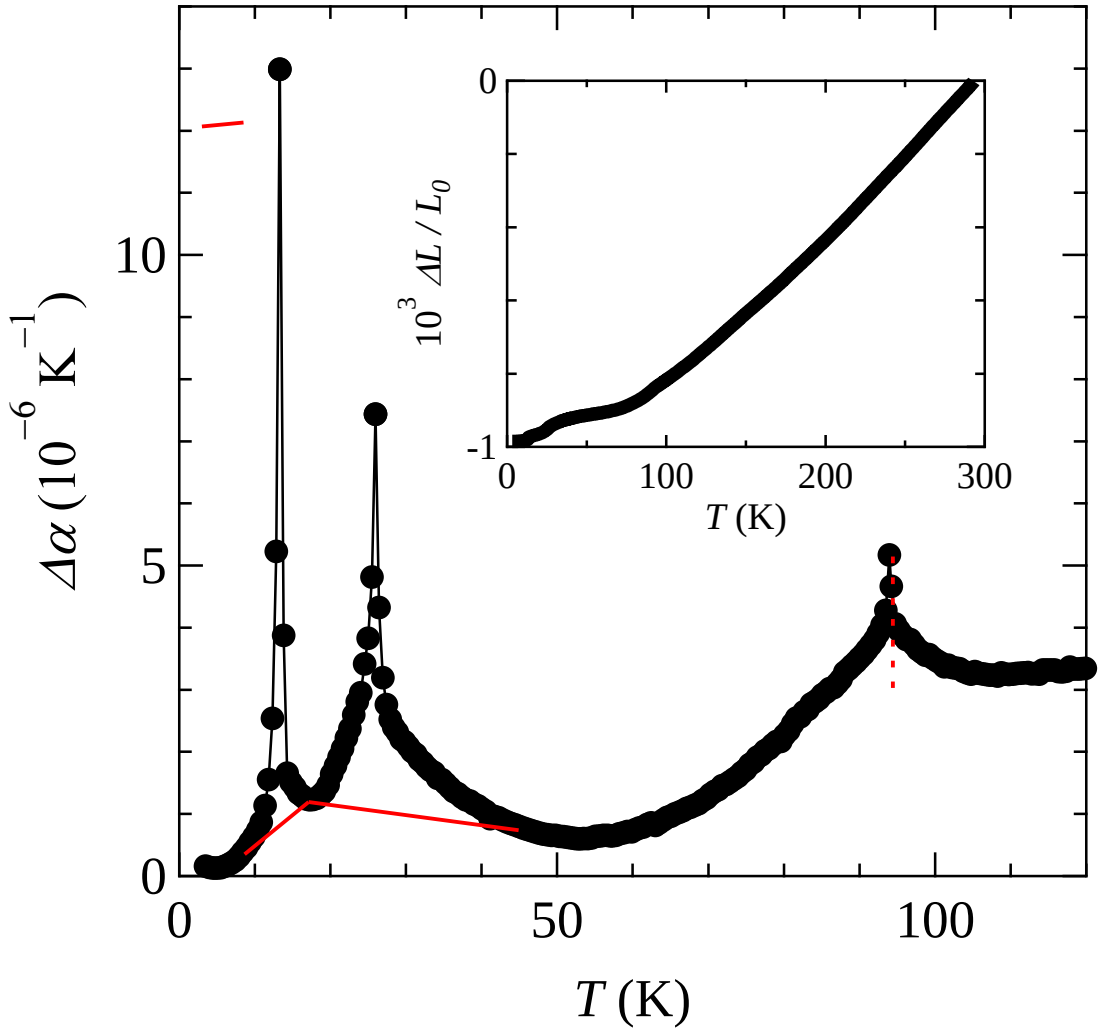

Fig. 5.5. Thermal expansion coefficient α of $CoCr_2O_4$ below 120 K. The lines are the baselines used to obtain the jumps and/or the excess contributions in α. The inset shows the linear thermal expansivity $\Delta L/L_0$ in the entire region.

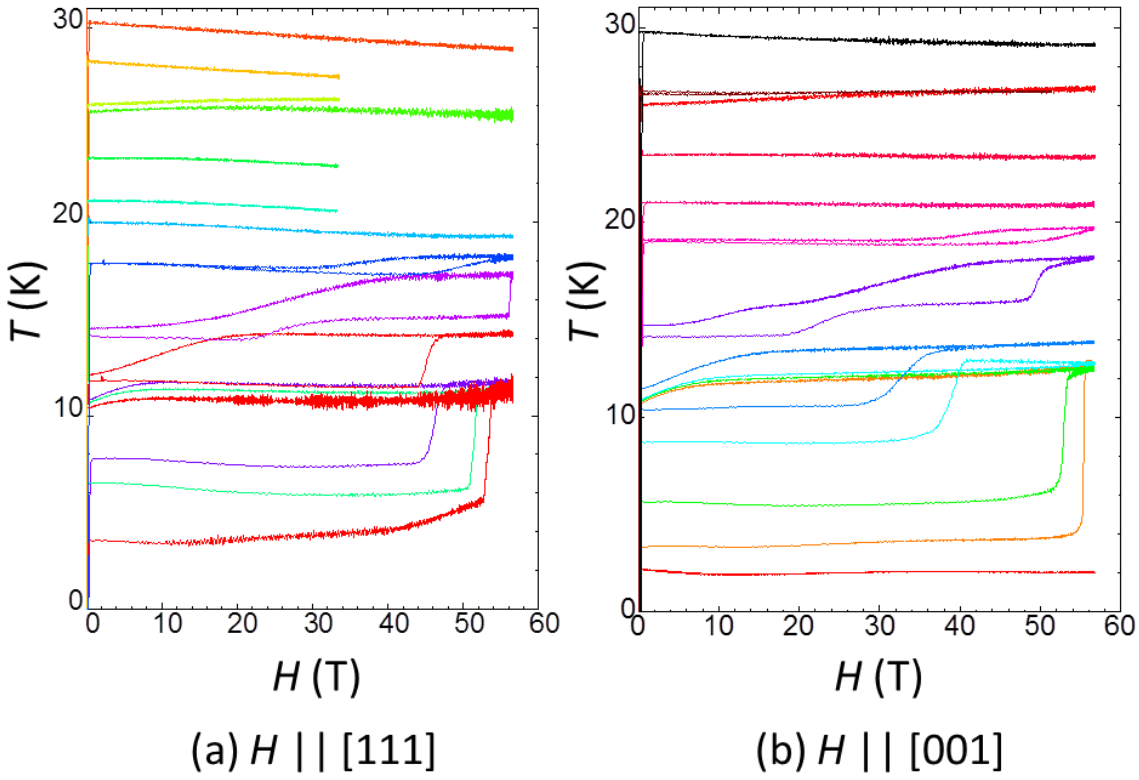

Fig. 5.6. Magnetocaloric effects with the magnetic field along (a) the [111] axis and (b) the [001] axis, respectively. Here the representative curves were drawn.

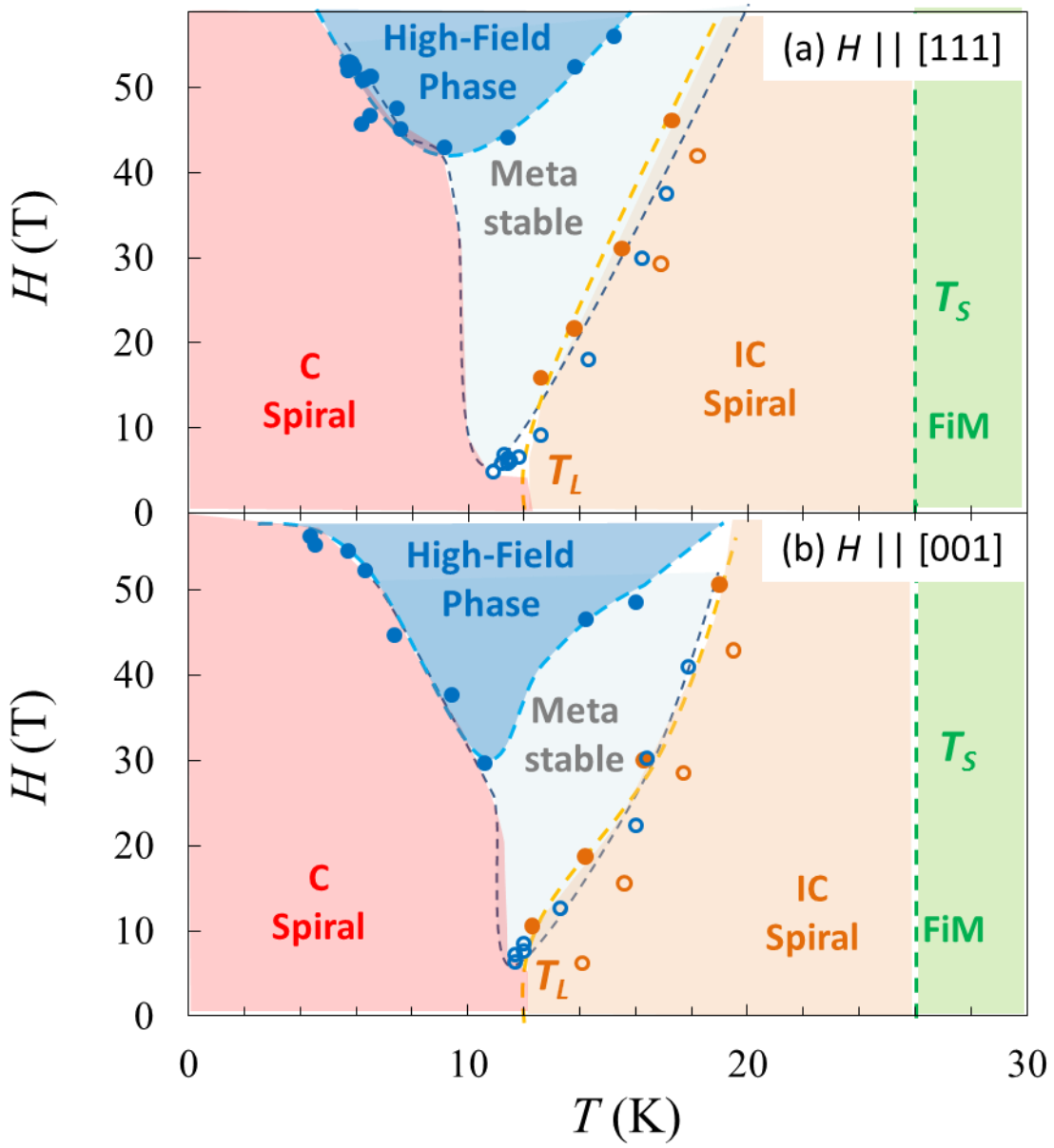

Fig. 5.7. *H-T* phase diagram with the magnetic field along (a) the [111] axis and (b) the [001] axis. The open circles and closed circles the denote field-increasing and -decreasing processes.

References

[1] D. H. Lyons, T. A. Kaplan, K. Dwight, and N. Menyuk, Phys. Rev. **126**, 540 (1962).

[2] N. Menyuk, K. Dwight and A. Wold, J. Phys. (Paris) **25**, 528 (1964).

[3] Y. Yamasaki, S. Miyasaka, Y. Kaneko, J.-P. He, T. Arima, and Y. Tokura, Phys. Rev. Lett. **96**, 207204 (2006).

[4] K. Tomiyasu, H. Suzuki, M. Toki, S. Itoh, M. Matsuura, N. Aso, and K. Yamada, Phys. Rev. Lett. **101**, 177401 (2008).

[5] S. Funahashi, Y. Morii, and H. R. Child, J. Appl. Phys. **61**, 4114 (1987).

[6] L. J. Chang, D. J. Huang, W-H. Li, S-W. Cheong, W. Ratcliff, II, and J. W. Lynn, J. Phys.: Condens. Matter **21**, 456008 (2009).

[7] Y. J. Choi, J. Okamoto, D. J. Huang, K. S. Chao, H. J. Lin, C. T. Chen, M. van Veenendaal, T. A. Kaplan, and S-W. Cheong, Phys. Rev. Lett. **102**, 067601 (2009).

[8] I. Kim, Y. S. Oh, Y. Liu, S. H. Chun, J.-S. Lee, K.-T. Ko, J.-H. Park, J.-H. Chung, and K. H. Kim, Appl. Phys. Lett. **94**, 042505 (2009).

[9] P. Curie, J. Phys. (Paris) **3** (Ser. III), 393 (1894).

[10] T. Kimura, T. Goto, H. Shintani, K. Ishizaka, T. Arima, and Y. Tokura, Nature (London) **426**, 55 (2003).

[11] N. Hur, S. Park, P. A. Sharma, J. S. Ahn, S. Guha, and S-W. Cheong, Nature (London) **429**, 392 (2004).

[12] G. Lawes, A. B. Harris, T. Kimura, N. Rogado, R. J. Cava, A. Aharony, O. Entin-Wohlman, T. Yildirim, M. Kenzelmann, C. Broholm, and A. P. Ramirez, Phys. Rev. Lett. **95**, 087205 (2005).

[13] H. Katsura, N. Nagaosa, and A. V. Balatsky, Phys. Rev. Lett. **95**, 057205 (2005).

[14] I. A. Sergienko, and E. Dagotto, Phys. Rev. B **73**, 094434 (2006).

[15] M. Rotter, H. Müller, E. Gratz, M. Doerr, and M. Loewenhaupt, Rev. Sci. Instrum. **69**, 2742 (1998).

[16] P. Cossee, and A. E. Van Arkel, J. Phys. Chem. Solids **15**, 1 (1960).

[17] A. Pelissetto and E. Vicari, Phys. Rep. **368**, 549 (2002).

[18] H. Kawamura, J. Phys.: Condens. Matter **10**, 4707 (1998).

[19] J. A. Souza, Y.-K. Yu, J. J. Neumeier, H. Terashita, and R. F. Jardim, Phys. Rev. Lett. **94**, 207209 (2005).

[20] G. Lawes, B. Melot, K. Page, C. Ederer, M. A. Hayward, T. Proffen, and R. Seshadri, Phys. Rev. B **74**, 024413 (2006).

[21] K. Ohgushi, Y. Okimoto, T. Ogasawara, S. Miyasaka, and Y. Tokura, J. Phys. Soc. Jpn. **77**, 034713 (2008).

[22] T. Kanomata, T. Tsuda, H. Yasui, and T. Kaneko, Phys. Lett. A **134**, 196 (1988).

[23] C. R. dela Cruz, F. Yen, B. Lorenz, M. M. Gospodinov, C. W. Chu, W. Ratcliff, J. W. Lynn, S. Park, and S.-W. Cheong, Phys. Rev. B **73**, 100406(R) (2006).

[24] R. P. Chaudhury, F. Yen, C. R. dela Cruz, B. Lorenz, Y. Q. Wang, Y. Y. Sun, and C. W. Chu, Physica B **403**, 1428 (2008).

[25] S. Bordács, D. Varjas, I. Kézsmárki, G. Mihály, L. Baldassarre, A. Abouelsayed, C. A. Kuntscher, K. Ohgushi, and Y. Tokura, Phys. Rev. Lett. **103**, 077205 (2009).

[26] V. Tsurkan, S. Zherlitsyn, S. Yasin, V. Felea, Y. Skourski, J. Deisenhofer, H.-A. Krug von Nidda, J. Wosnitza, and A. Loidl, Phys. Rev. Lett. **110**, 115502 (2013).

[27] A. V. Pronin, M. Uhlarz, R. Beyer, T. Fischer, J. Wosnitza, B. P. Gorshunov, G. A. Komandin, A. S. Prokhorov, M. Dressel, A. A. Bush, and V. I. Torgashev, Phys. Rev. B **85**, 012101 (2012).

Chapter 6

Lack of the spin-lattice coupling in spin liquid state of $Tb_2Ti_2O_7$

6.1 INTRODUCTION

$Tb_2Ti_2O_7$ has a strong Ising magnetic anisotropy along the local <111> axes. Tb^{3+} ions has an antiferromagnetic interaction with a Curie-Weiss temperature Θ_{CW} = -19 K [1, 2, 3], which should induce a transition into a long-range ordered state at T_N ~ 1 K [4]. However, $Tb_2Ti_2O_7$ does not show any conventional long-range order down to 20 mK [2, 3]. In addition, the existence of competing reports gives rise to the confusion in the systematic comprehension for the spin liquid state [5]. To elucidate the nature of the ground state, several theoretical models have been proposed [6, 7, 8, 9, 10], though no theory has succeeded in simultaneously accounting for the results of neutron scattering experiments and other macroscopic magnetic properties over a decade. Recently, neutron scattering experiments for single crystalline sample found out the diffuse magnetic scattering at (1/2, 1/2, 1/2) and the pinch-point-like scattering, suggesting the realization of a quantum spin ice state [11, 12, 13].

Through the investigation of $Tb_2Ti_2O_7$, it has been considered that the spin-lattice coupling plays a crucial role as manifested by an anomalous temperature dependence of Young's modulus [14, 15], elastic constants [16], giant magnetostriction [17, 18], and anisotropic structural Bragg-peak broadening [19]. Strong spin-lattice coupling in the frustrated material can lead to an anomalous thermal expansion and finally result in a

phase transition with a structural distortion as reported in the chromium spinel oxides [20, 21]. The spin-lattice effects observed in $Tb_2Ti_2O_7$ have been attributed to a precursor of a cooperative Jahn-Teller transition as firstly suggested by Mamsurova [14]. Such transition and even a static distortion have not been observed [22, 23], though recent x-ray scattering measurements on a single crystalline sample reported dynamic distortion, resulting in negative thermal expansion below 20 K [19].

In this study, the low-temperature lattice behavior of the pyrochlore titanate, $Tb_2Ti_2O_7$, has been investigated by heat capacity and thermal expansion measurements. The initial motivation is to obtain detailed thermal expansion data of $Tb_2Ti_2O_7$ at low temperature using a capacitance dilatometer, because a recent x-ray study on a polycrystalline sample showed only positive thermal expansion [24], which is strikingly conflict with the previous x-ray result on a single crystalline sample [19]. Our results show that $Tb_2Ti_2O_7$ has a normal thermal expansion as interpreted by the lattice vibrations and the crystal field contributions.

6.2 EXPERIMENTAL

Single crystals of $Tb_2Ti_2O_7$, which were from the same batch as in Ref. [25], were grown by a flux method with PbO, PbO_2, PbF_2, and MoO_3 as the flux. Single crystal of non-magnetic $Lu_2Ti_2O_7$ was also prepared by the same method. The sample of $Lu_2Ti_2O_7$ is used to estimate the lattice contribution without magnetic interaction to the heat capacity and thermal expansion coefficient. The obtained single crystals were translucent brown with octahedral shapes, and their crystal structures were confirmed by powder x-ray diffraction within the space group *Fd*-3*m*.

Heat capacity was measured by the relaxation technique with a Quantum Design

PPMS down to 2 K. In order to investigate the heat capacity of $Tb_2Ti_2O_7$ below 2 K, the heat capacity measurements by the quasi-adiabatic technique with a home-made calorimeter in a ^{3}He/^{4}He dilution refrigerator were carried out. Thermal expansion measurements were carried out with a high-resolution capacitance dilatometer made of silver [20, 26]. The measurements were performed on the cubic <111> axis with the length of 3.03 mm.

6.3 RESULTS AND DISCUSSION

6.3.1 Heat capacity

Figure 6.1 shows the heat capacity C_p of $Tb_2Ti_2O_7$. The two shoulders around 8 K and 2 K in the C_p have been observed in the previous heat capacity measurements, though the shapes of the anomalies are considerably different from report to report [27-37]. Most resemble data to our results can be seen in Ref. [30, 32]. The critical difference between the reports is the presence or absence of a sharp peak around 0.5 K. Taniguchi *et al.* [35] figured out that the strong sample dependence is accounted for the non-stoichiometry x of the sample $Tb_{2+x}Ti_{2-x}O_y$. The value of x changes the ground state from a spin liquid state (x<0.05) to an ordered state (x>0.05). Although it is generally difficult to control the non-stoichiometry of single crystal, Helean *et al.* [38] reported that the flux-grown sample has Tb-poor composition (x<0). The negative value of x suggests that the flux grown sample belongs to the spin liquid regime. A pyrochlore sample grown with Pb-flux may have a small impurity of lead [38], which might modulate the low-temperature magnetism. Nevertheless, our sample would belong to a spin liquid compound, because the C_p did not show any indication for the phase

transition down to 0.7 K [29, 35, 37].

The crystal-electric-field (CEF) in $Tb_2Ti_2O_7$ affects the low-temperature C_p. Leaving aside the intriguing possibility of the splitting of the ground state doublet, one can accept the presence of the low-lying excited CEF doublet at around 18 K [1, 3, 28, 39]. When the ground doublet and excited doublet states is separated by an energy Δ, the thermal population of the excited state leads to a contribution to the molar heat capacity, so called Schottky heat capacity with the form

$$C_{\mathrm{Sch}}(T) = k_B N_A \left(\frac{\Delta}{T}\right)^2 \frac{e^{-\Delta/T}}{\left(1+e^{-\Delta/T}\right)^2}, \quad (1)$$

where k_B is the Boltzmann constant and N_A is the Avogadro constant. Because the equation resulted in a poor fit for the experimental data, we considered that the CEF splitting energy Δ has a distribution due to the inhomogeneity. This assumption might be reasonable for the strong sample dependence of the C_p of $Tb_2Ti_2O_7$. Applying a Gaussian distribution to Δ derives a possibility distribution of Δ:

$$P(\Delta') = \frac{1}{\sqrt{2\pi\sigma^2}} \exp\left(-\frac{(\Delta'-\Delta_0)^2}{2\sigma^2}\right), \quad (2)$$

where Δ_0 is the median of the CEF splitting energy, and σ^2 is its variance. The CEF contribution to the heat capacity is then given by

$$C_{\mathrm{CEF}}(T) = \int P(\Delta') C_{\mathrm{Sch}}(T, \Delta') d\Delta'. \quad (3)$$

The experimental data were fitted by numerical integration of this equation and the lattice contribution estimated from scaling of the C_p of $Lu_2Ti_2O_7$. The curve with the parameters $\Delta_0 = 18$ and $\sigma = 7.6$ fits reasonably well above 7 K, as shown in Fig. 6.1. The slight deviation at higher temperature is due to the higher CEF level at around 120 K.

Further insight on the 2 K anomaly is provided from the magnetic field dependence of the C_p below 8 K, as presented in Fig. 6.2. It should be noted that the values of heat

capacity of $Tb_2Ti_2O_7$ obtained by the two calorimeters reasonably agree in the temperature region from 1.8 K to 2.5 K, but their agreements got worse with increasing temperature, and the deviation of their value reaches to ~10% above 4 K. The reason of the deviation has not been figured out at present. Hence, the absolute values of the heat capacity and entropy will not be discussed.

Applying magnetic fields along the <111> direction have induced noticeable effects on the shoulder-like peak around 2 K. The peak was enhanced by magnetic field up to 1 T with a little suppression in the C_p below 1 K. With further increasing field, the shoulder shape gradually collapsed and changed the shape into a broad hump. At 17 T, the hump had faded away and a sharp rise appeared below 1 K, which is attributed to a nuclear Schottky anomaly, resulting from the splitting of the energy levels of the ^{159}Tb nuclear spin (I = 3/2) due to the hyperfine field. As seen in Fig. 6.2, the C_p under high magnetic fields still had much higher values than the lattice heat capacity, which indicates that Tb^{3+} spins has not aligned all along the field direction.

The magnetic field along the [111] axis (threefold axis) breaks down the magnetic structure of the cubic *Fd*-3*m* symmetry and leads to the new magnetic structure of the rhombohedral *R*-3*m* [40]. The symmetry conversion results in a splitting of one Tb position in *Fd*-3*m* into two crystallographically nonequivalent 3*b* and 9*e* Wyckoff positions in *R*-3*m*, which gives rise to symmetry constrains for the Tb magnetic moments. As a results, the magnetic structure under magnetic field along the [111] axis is to be the so-called “3-in, 1-out / 1-in 3-out” structure; in a single tetrahedron, one moment (3*b* position) points along the field direction [111], and the other three moments (9*e* position) point toward the center of the tetrahedron or the reverse depending on the direction of the moment on the 3*b* position. The three moments are hard to rotate their

orientations against the field direction due to the symmetry constrains. Neutron diffraction experiments demonstrate that these moments still deviate from the field direction by about 40^o even at 12 T [40]. Thus, the field dependence of the C_p stems from this spin behavior, and the deviation is arguably not to be resolved yet at 17 T. The temperature dependence of the C_p under 17 T was estimated by subtracting the nuclear Schottky contribution, obtained from fitting the upturn in the C_p below 1 K by the equation AT^{-2}, which resulted in $C_p \sim T^{1.75}$ below 4 K. At low temperature, the strong magnetostriction has been observed [17, 18]. However, the lattice entropy would not be remained at low temperature if a considerable lattice distortion is induced by the magnetic field. Thus, the anomalous temperature dependence might be the characteristic feature of the spin excitation.

Assuming that the C_p linearly decreases down to lowest temperature from the last measurement point, the entropy under various magnetic fields was calculated as shown in Fig. 6.3, where the lattice and nuclear contributions would be partially included. The entropy under 1 T was higher than that of zero field at 8 K. Even if the C_p under 1 T will be decreases with the T^3 manner below 0.7 K, this difference could not be overcome. The contribution of the 2 K anomaly does not persist above 8 K, as seen in the later. Thus, applying magnetic field of 1 T (~1.5 K) is not able to gain additional entropy from above 8 K. The low-lying CEF state at 18 K may be affected by the magnetic field. However, the C_p of the 2 K shoulder had already increased at 0.5 T, while the C_p at 8 K was not changed. Therefore, the low-lying CEF contribution can also be excluded. The 3*b* site moment saturates (~6 μ_B) above 1 T, which indicates the unique configuration of the 3-in, 1-out / 1-in 3-out state [40]. The presence of the saturated 3*b* site moment should lead the entropy loss. If the Tb^{3+} ions under magnetic field still have Ising

character, the entropy loss is to be $0.5R\ln 2$. Thus, the increase in the C_p with applying magnetic field indicates that the ground state of $Tb_2Ti_2O_7$ has higher entropy than the $0.5R\ln 2$.

In the pyrochlore analogue of spin ice $Dy_2Ti_2O_7$, applying magnetic field along the [111] axis induces the kagome ice state, where the "2-in, 1-out / 1-in 2-out" spin structure emerges in the kagome plane piled in the [111] direction [41]. Further applying field leads to the 3-in, 1-out / 1-in 3-out state. Due to the formation of such spin state, the residual entropy in zero field, $1/2R\ln(3/2)$, decreases by 60% in the 2-in, 1-out / 1-in 2-out state, and by 75% in the 3-in, 1-out / 1-in 3-out state. Note that no residual entropy is theoretically expected for the latter state because the spin configuration in the tetrahedron is of the unique 1-in, 3-out state. However, as shown in the above, the entropy of $Tb_2Ti_2O_7$ was nearly constant up to 1 T field that is expected to induce the 3-in, 1-out / 1-in 3-out state. Furthermore, the magnetization plateau, which is considered to be the evidence for the quantum kagome ice state, has not been observed below 1 T. Accordingly, the spins continuously modify the dynamical correlation with increasing magnetic field, and the moments at the 9*e* site might be correlated as strong as in the zero field state even at 1 T.

6.3.2 Thermal expansion

Figure 6.4 provides the thermal expansion coefficient α of $Tb_2Ti_2O_7$, where only positive thermal expansion was observed down to 2 K. Previous x-ray experiments have been provided conflict reports for the low-temperature thermal expansion that a single crystalline sample exhibited negative thermal expansion below 20 K [19], while a powder sample showed only normal positive thermal expansion down to 4 K [24]. Our

results with the single crystalline sample well agree with the powder x-ray results. Note that the C_p of the polycrystalline sample used in Ref. [24] showed a clear peak at 0.5 K, suggesting that the ground state differs from our sample.

Unlike the C_p, the α shows only one shoulder around 7 K, which would be attributed to the effect of the low-lying CEF doublet at around 18 K. Then, we estimated the CEF contribution to the thermal expansion coefficient α_{CEF}. According to the Maxwell's relations, we can obtain the relationship between heat capacity and thermal expansion as

$$\frac{\alpha(T)}{C(T)} = \frac{1}{3V_m}\frac{\partial \ln E}{\partial p}, \qquad (4)$$

where V_m denotes the molar volume, and E is the energy for a relevant system. Thus, the α'_{CEF} can be expressed as

$$\alpha_{\mathrm{CEF}}(T) = \frac{1}{3V_m}\frac{\partial \ln \Delta}{\partial p} C_{\mathrm{CEF}}(T). \qquad (5)$$

When Eq. (5) was used to fit the experimental data, we took the green line in Fig. 6.1 as C_{CEF}(T), and $\partial \ln \Delta / \partial p$ was used as a fitting parameter. The lattice contribution was estimated from scaling of the α of $Lu_2Ti_2O_7$. The fit with $\partial \ln \Delta / \partial p$=0.031/GPa adequately reproduces the α for the whole temperature range below 20 K. Therefore, it indicates that the origin of the C_p anomaly below 7 K has little influence on the thermal expansion.

The combination of $\partial \ln \Delta / \partial p$ and bulk modulus $B = -V\,\partial p/\partial V$ derives the volume dependence of the CEF splitting energy $\gamma_{\mathrm{CEF}} = -\partial \ln \Delta / \partial \ln V$, called Grüneisen parameter. Taking the bulk modulus of 46 GPa at 4.2 K [16], our result leads to γ_{CEF} ~1.4. The γ_{CEF} can also be roughly estimated from the change in Δ with a lattice constant change. From $Tb_2Ti_2O_7$ to $Tb_2Sn_2O_7$, the lattice constant a increases about

2.7% [3, 42], resulting in the decrease of Δ about 9.2%,[IM07] *i.e.*, $\Delta \propto \sim a^{-3.6}$. Because $V = a^3$, we have $\gamma_{\mathrm{CEF}} = -(1/3)(\partial \ln \Delta / \partial \ln a) = 1.2$, being consistent with our estimation. The magnitude of the evaluated γ_{CEF} is comparable to $\gamma_{\mathrm{CEF}} \sim 5/3$, which stems from the point charge model for the cubic CEF field [43]. Similar discussion can be applied for the lattice contribution to the C_p and α. For them, Eq. (5) can be rewritten as

$$\alpha_{\mathrm{lat}}(T) = \frac{1}{3V_m}\frac{\partial \ln \Theta_{\mathrm{D}}}{\partial p} C_{\mathrm{lat}}(T), \qquad (6)$$

where Θ_{D} is the Debye temperature. Using the black lines in Figs. 6.1 and 6.4 as the C_{lat} and α_{lat}, we obtain $\partial \ln \Theta_{\mathrm{D}} / \partial p$=0.030/GPa, which results in $\gamma_{\mathrm{lat}} \sim 1.4$. The lattice Grüneisen parameter is typically of the order of unity for many solids. Thus, the estimated γ_{CEF} and γ_{lat} are both moderate, indicating that a considerable coupling between CEF and lattice as suggested by the previous measurements seems to be absent in the thermal expansion.

6.3.3 Discussion about low temperature anomaly at 2 K

The correspondence of the CEF contribution in the C_p and α allows us to yield the clear component of the low-temperature C_p anomaly below 7 K, which has been debated [28, 32, 44]. The subtraction of the CEF and lattice contribution from the C_p gives the excess heat capacity C_{ex} shown in Fig. 6.5 (Blue circles). It is worth noting that multilevel Schottky models could not adequately describe the C_{ex}. Below 1 K, the C_{ex} is proportional to T. The T-linear dependence of the low-temperature heat capacity has been observed in some spin liquid materials [45]. Assuming that the C_{ex} linearly decreases down to lowest temperature, we evaluated the excess entropy S_{ex} by

integrating C_{ex}/T, which leads to the total excess entropy S_{ex}~7.5 J/Kmol. Although the splitting of the ground state doublet into two singlets gives rise to the entropy of $2R\ln(2)$, the S_{ex} is about 65% of $2R\ln(2)$. Additionally, further decrease in the S_{ex} is expected from the presence of the nuclear contribution, as seen in Fig. 6.2. The shortfall of the entropy is still larger compared with the spin-ice entropy $S=2R[\ln 2-1/2R\ln(3/2)]=8.16$ J/Kmol. Similar shortfall of the entropy can be observed in $Pr_2Sn_2O_7$, a candidate for quantum spin ice materials [46]. Naively, the S_{ex} implies the quantum spin state as suggested in several theories for the ground state of $Tb_2Ti_2O_7$, or at least reflects a strong dynamic nature of the ground state.

The thermodynamic equations lead to further interesting insight on the relevant energy scale of the low temperature anomaly below 7 K. It is obvious that equation (4) results in $\partial \ln E / \partial p \to 0$ with $T \to 0$, and hence $\partial \ln E / \partial V \to 0$ with $T \to 0$, because the α vanishes at low temperature and the C_p remains a significant value. These convergences indicate that the low-temperature C_p anomaly is independent from a pressure and volume. Therefore, the ground state without a long range ordering might be established with little relation to the spin-lattice coupling. We speculate that some samples possibly show a different thermal expansion from our results and Ref. [24]. It is known that the Grüneisen parameter diverges at a quantum critical point, where the characteristic energy scale vanishes [47]. This divergence corresponds to the divergence of the thermal expansion coefficient with decreasing temperature. Hence, a sample located near the quantum critical point between a spin liquid state and an ordered state will exhibit an anomalous thermal expansion. We expect that thermal expansion measurements on well-characterized samples leads to more systematic comprehension on the spin-lattice coupling, and even the enigmatic ground state in $Tb_2Ti_2O_7$.

6.4 CONCLUSION

The present chapter has focused on the lattice behavior in the spin liquid state of the pyrochlore titanate $Tb_2Ti_2O_7$. Spin liquid compound, $Tb_2Ti_2O_7$, showed the shoulder-like anomaly around 8 K in both heat capacity and thermal expansion coefficient, and the anomalous contribution below 7 K could be observed only in the heat capacity. The 8 K anomaly in both heat capacity and thermal expansion coefficient can be accounted for the Shottky effect, which is resulted from the presence of the low-lying first excited CEF state at 18 K for which a Gaussian distribution due to the inhomogeneity was applied. The Grüneisen parameters of the lattice and CEF were the normal value. In addition, the characteristic energy scale of the heat capacity anomaly below 7 K is independent from a pressure and volume. These results indicate the absence of a spin-lattice effect, and the spin-lattice coupling is not need to establish a non-ordered ground state. The combination of our heat capacity and thermal expansion data provided the pure component for the heat capacity anomaly below 7 K. The excess heat capacity led to the excess entropy S_{ex}~7.5 J/Kmol, which is rather small compared to the expected entropy for the ground CEF doublet splitting $S=2R\ln(2)=11.5$ J/Kmol. The large shortfall in entropy indicates the strong fluctuation in the ground state, and possibly relates with a realization of a quantum spin ice state.

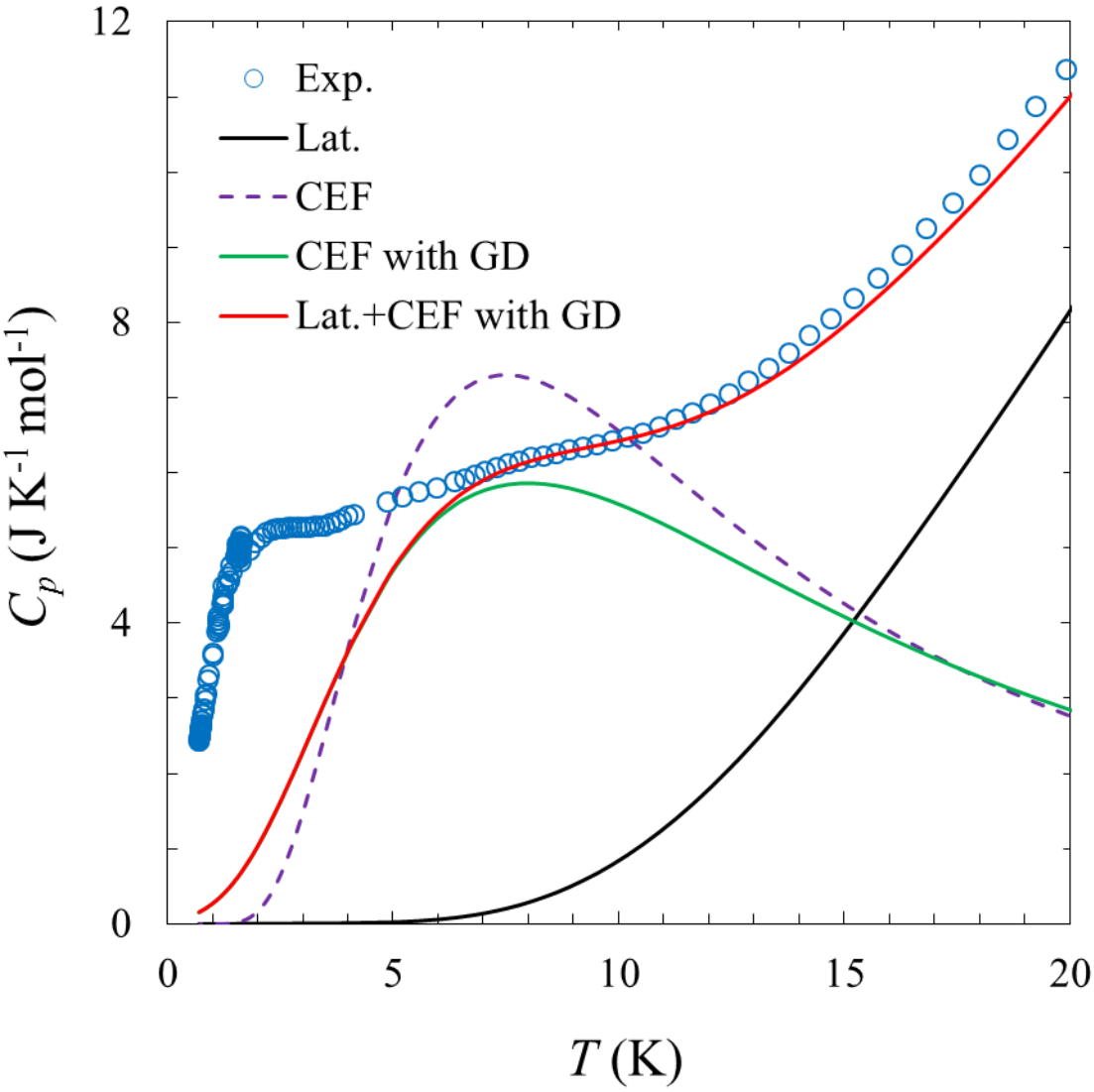

Fig. 6.1. Heat capacity C_p of $Tb_2Ti_2O_7$. The CEF contribution estimated from Δ=18 K with a Gaussian distribution (GD) is indicated by the green line, while that without a GD by the purple dashed line. The lattice contribution estimated by scaling the C_p of non-magnetic $Lu_2Ti_2O_7$ is shown as the black line. Above 10 K, the total heat capacity obtained by the summation of the CEF and lattice contribution is in good agreement with the experimental data, though the lower temperature data considerably depart from the estimated heat capacity.

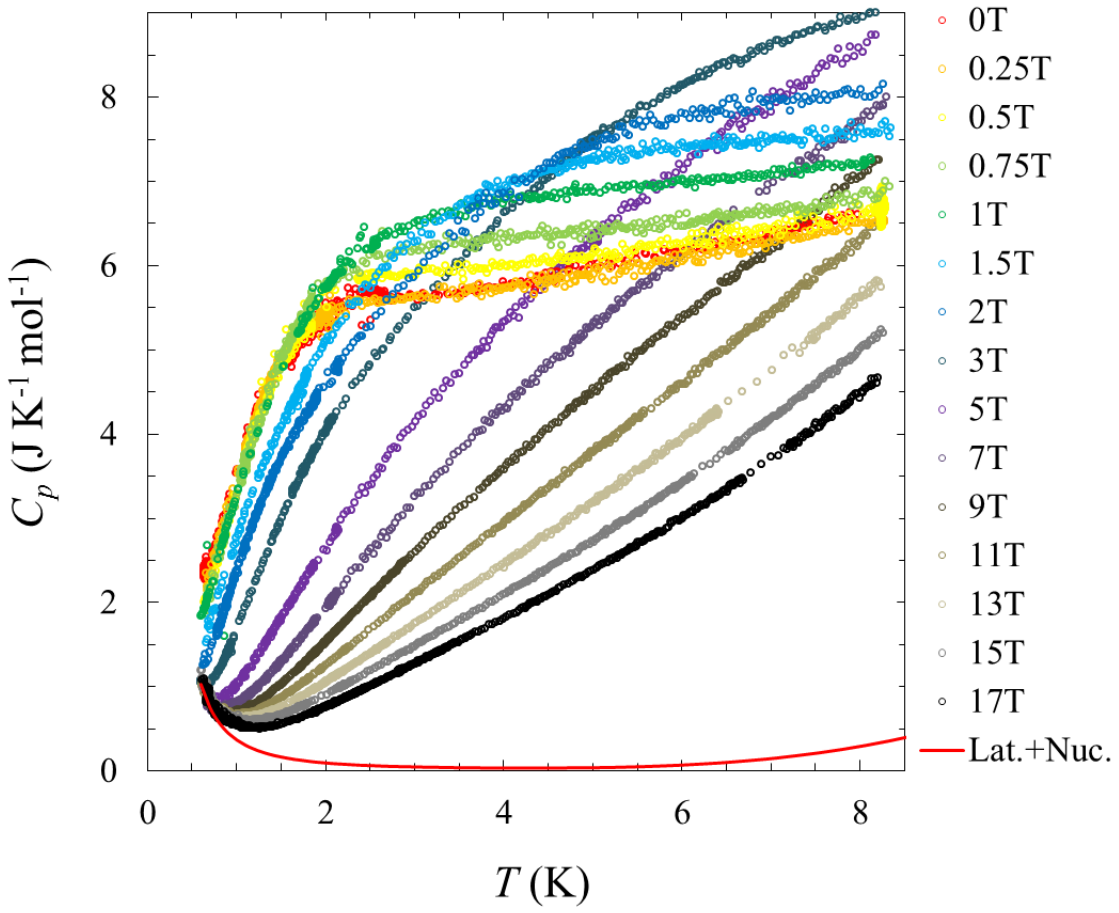

Fig. 6.2. Magnetic field dependence of the heat capacity C_p of $Tb_2Ti_2O_7$. The red line indicates the summation of the lattice contribution being the same with that in Fig. 6.1 and the nuclear contribution, which was estimated by fitting the C_p at 17 T using the equation AT^{-2} with A = 0.38 J K mol^{-1}.

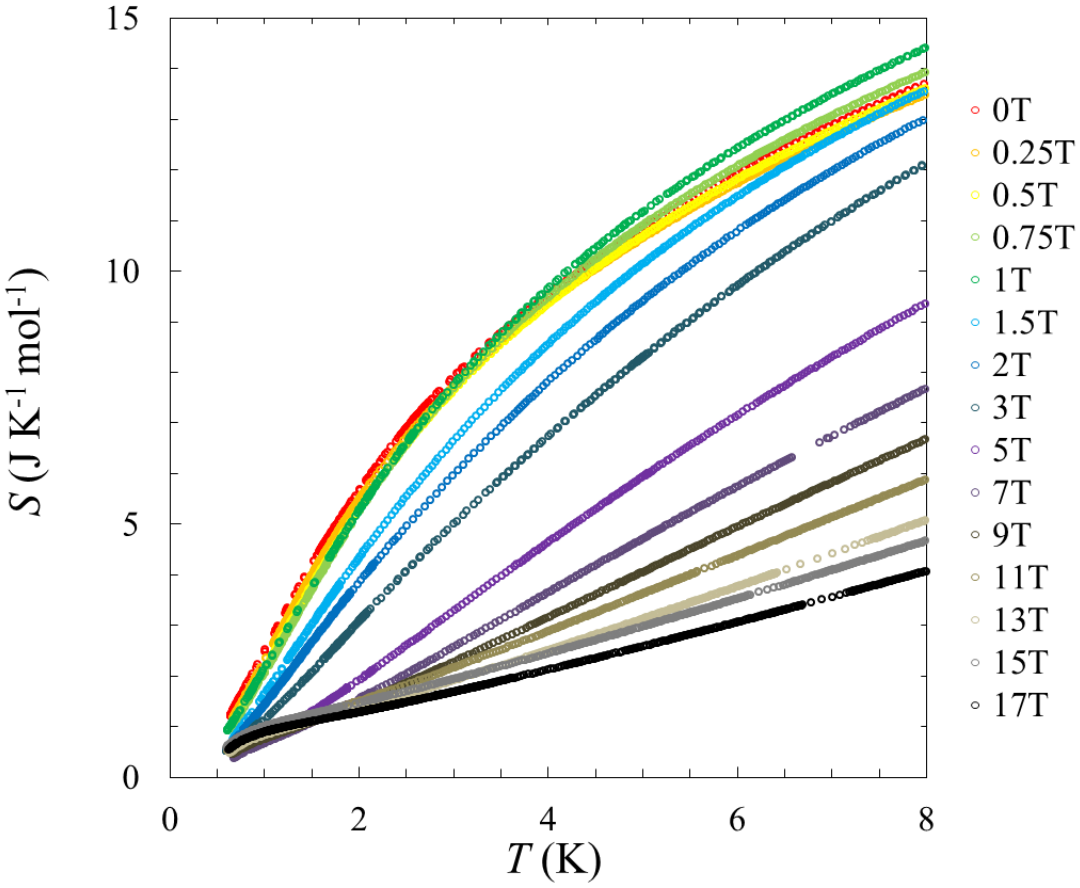

Fig. 6.3. Entropy S under various magnetic fields of $Tb_2Ti_2O_7$, which were obtained by integrating the C_p/T without any subtraction from C_p.

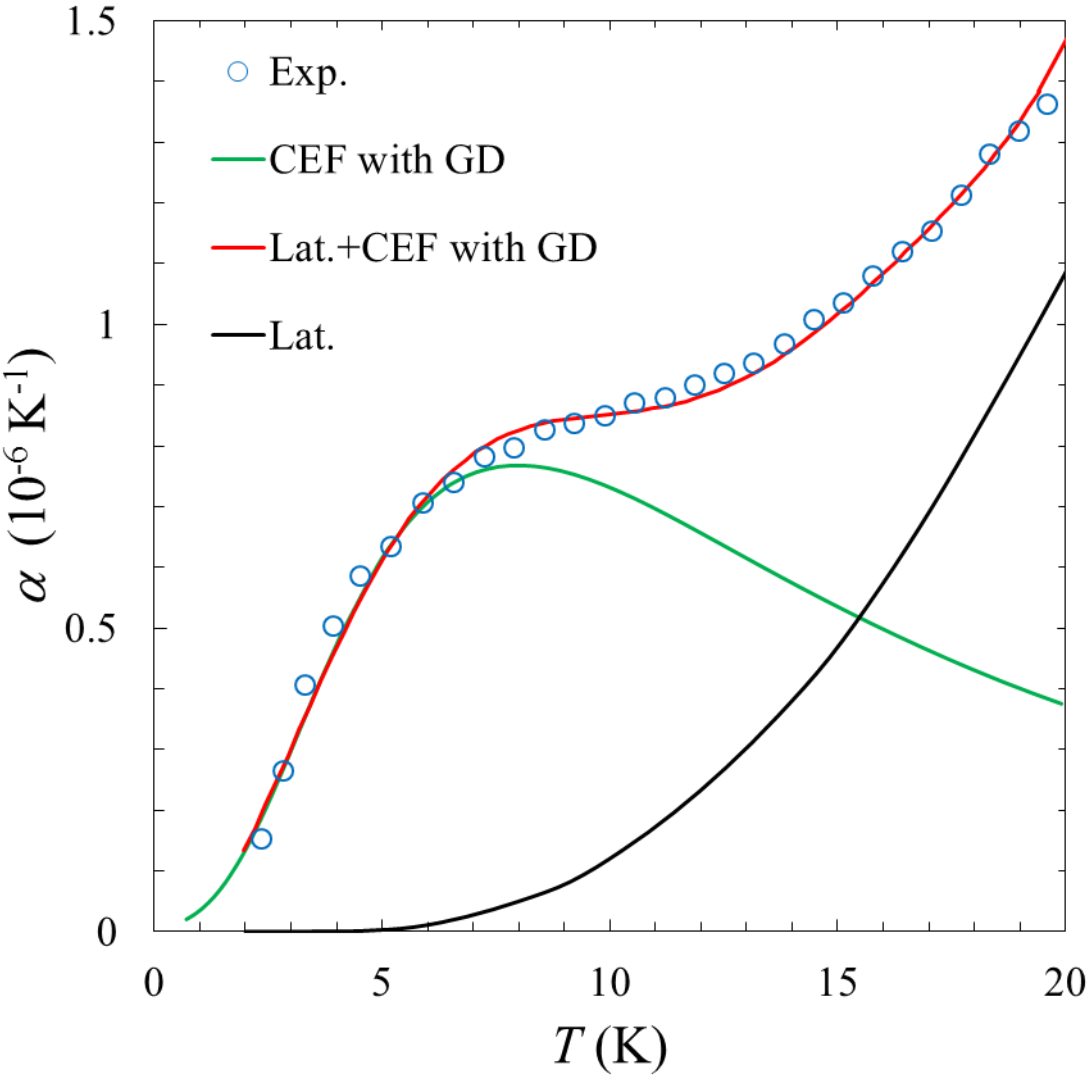

Fig. 6.4. Thermal expansion coefficient α of $Tb_2Ti_2O_7$. The CEF contribution indicated by the green line is obtained from scaling the CEF heat capacity (see text), while the lattice contribution was estimated from the α of $Lu_2Ti_2O_7$ as in the same manner in the C_p. The total thermal expansion coefficient fairly describes the experimental data, which is totally different from the situation in the heat capacity.

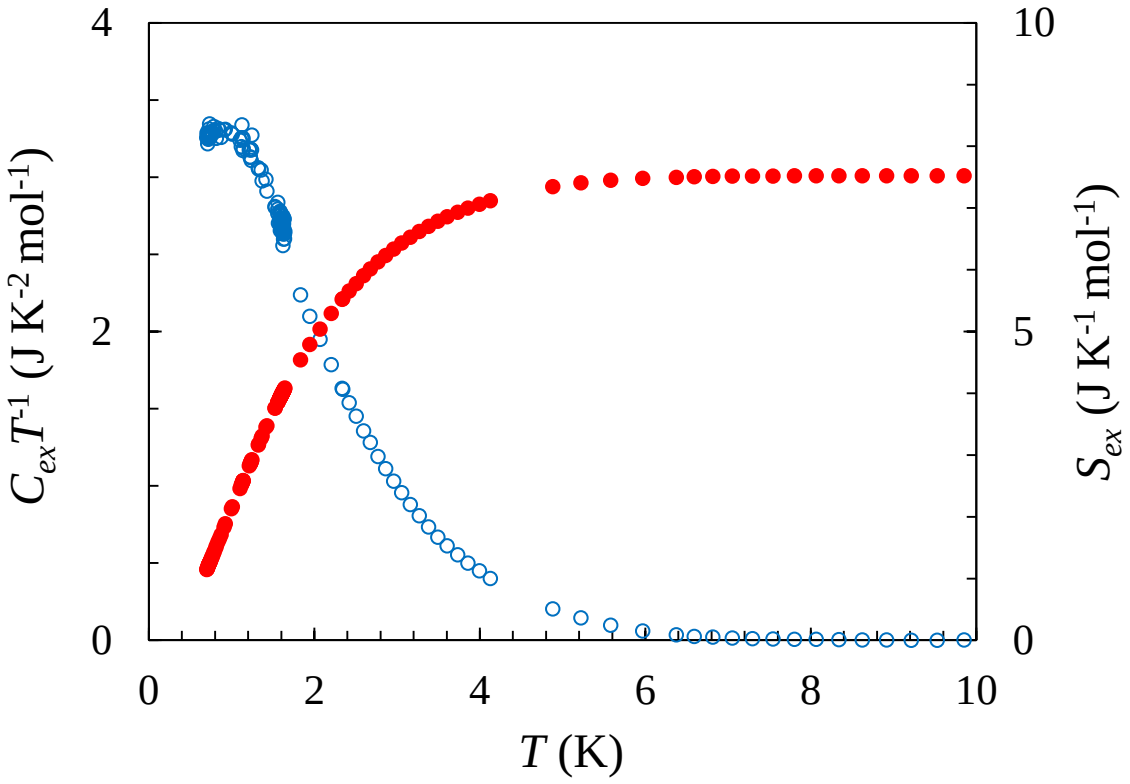

Fig. 6.5. Excess heat capacity divided by temperature $C_{ex}T^{-1}$ (blue open circles) and excess entropy S_{ex} (red closed circles) of $Tb_2Ti_2O_7$. The C_{ex} showed T-linear temperature dependence below 1 K. This curve cannot be reproduced by a multilevel Schottky model. The S_{ex} reached to ~7.5 J K^{-1} mol^{-1}, which is just 2/3 of Rln(2), expected for the ground doublet splitting.

References

[1] I. Mirebeau, P. Bonville, and M. Hennion, Phys. Rev. B **76**, 184436 (2007).

[2] J. S. Gardner, S. R. Dunsiger, B. D. Gaulin, M. J. P. Gingras, J. E. Greedan, R. F. Kiefl, M. D. Lumsden, W. A. MacFarlane, N. P. Raju, J. E. Sonier, I. Swainson, and Z. Tun, Phys. Rev. Lett. **82**, 1012 (1999).

[3] J. S. Gardner, B. D. Gaulin, A. J. Berlinsky, P. Waldron, S. R. Dunsiger, N. P. Raju, and J. E. Greedan, Phys. Rev. B **64**, 224416 (2001).

[4] Y.-J. Kao, M. Enjalran, A. Del Maestro, H. R. Molavian, and M. J. P. Gingras, Phys. Rev. B **68**, 172407 (2003).

[5] J. S. Gardner, M.J.P. Gingras, J.E. Greedan, Rev. Mod. Phys. **82,** 53 (2010).

[6] H. R. Molavian, M. J. P. Gingras, and B. Canals, Phys. Rev. Lett. **98**, 157204 (2007).

[7] S. H. Curnoe, Phys. Rev. B **78**, 094418 (2008).

[8] P. Bonville, I. Mirebeau, A. Gukasov, S. Petit, and J. Robert, Phys. Rev. B **84**, 184409 (2011).

[9] S. H. Curnoe, Phys. Rev. B **88**, 014429 (2013).

[10] P. Bonville, A. Gukasov, I. Mirebeau, and S. Petit, Phys. Rev. B **89**, 085115 (2014).

[11] T. Fennell, M. Kenzelmann, B. Roessli, M. K. Haas, and R. J. Cava, Phys. Rev. Lett. **109**, 017201 (2012).

[12] S. Petit, P. Bonville, J. Robert, C. Decorse, and I. Mirebeau, Phys. Rev. B **86**, 174403 (2012).

[13] K. Fritsch, K. A. Ross, Y. Qiu, J. R. D. Copley, T. Guidi, R. I. Bewley, H. A. Dabkowska, and B. D. Gaulin, Phys. Rev. B **87**, 094410 (2013).

[14] L. G. Mamsurova, K. S. Pigal'skiĭ, and K. K. Pukhov, JETP Lett. **43**, 755 (1986).

[15] L. G. Mamsurova, K. S. Pigal'skiĭ, K. K. Pukhov, N. G. Trusevich, and L. G. Shcherbakova, JETP **67**, 550 (1988).

[16] Y. Nakanishi, T. Kumagai, M. Yoshizawa, K. Matsuhira, S. Takagi, and Z. Hiroi, Phys. Rev. B **83**, 184434 (2011).

[17] I. V. Aleksandrov, B. V. Lidskiĭ, L. G. Mamsurova, M. G. Neygauz, K. S. Pigal'skiĭ, K. K. Pukhov, N. G. Trusevich, and L. G. Shcherbakova, JETP **62**, 1287 (1985).

[18] J. P. C. Ruff, Z. Islam, J. P. Clancy, K. A. Ross, H. Nojiri, Y. H. Matsuda, H. A. Dabkowska, A. D. Dabkowski, and B. D. Gaulin, Phys. Rev. Lett. **105**, 077203 (2010).

[19] J. P. C. Ruff, B. D. Gaulin, J. P. Castellan, K. C. Rule, J. P. Clancy, J. Rodriguez, and H. A. Dabkowska. Phys. Rev. Lett. **99**, 237202 (2007).

[20] S. Kitani, M. Tachibana, N. Taira, and H. Kawaji, Phys. Rev. B **87**, 064402 (2013).

[21] S. H. Lee, C. Broholm, T. H. Kim, W. Ratcliff, II, and S. W. Cheong, Phys. Rev. Lett. **84**, 3718 (2000).

[22] S.-W. Han, J. S. Gardner, and C. H. Booth, Phys. Rev. B **69**, 024416 (2004).

[23] O. Ofer, A. Keren, and C. Baines, J. Phys. Condens. Matter **19**, 145270 (2007).

[24] K. Goto, H. Takatsu, T. Taniguchi, and H. Kadowaki, J. Phys. Soc. Jpn. **81**, 015001 (2012).

[25] M. Tachibana, Solid State Commun. **174**, 16 (2013).

[26] M. Rotter, H. Müller, E. Gratz, M. Doerr, and M. Loewenhaupt, Rev. Sci. Instrum. 69, 2742 (1998).

[27] R. Siddharthan, B. S. Shastry, A. P. Ramirez, A. Hayashi, R. J. Cava, and S. Rosenkranz, Phys. Rev. Lett. **83**, 1854 (1999).

[28] M. J. P. Gingras, B. C. den Hertog, M. Faucher, J. S. Gardner, S. R. Dunsiger, L. J. Chang, B. D. Gaulin, N. P. Raju, and J. E. Greedan, Phys. Rev. B **62**, 6496 (2000).

[29] N. Hamaguchi, T. Matsushita, N. Wada, Y. Yasui, and M. Sato, Phys. Rev. B **69**, 132413 (2004).

[30] A. L. Cornelius, B. E. Light, R. S. Kumar, M. Eichenfielda, T. Duttona, R. Pepina, J. S. Gardner Physica B **359-361**, 1243 (2005).

[31] X. Ke, D. V. West, R. J. Cava, and P. Schiffer, Phys. Rev. B **80**, 144426 (2009).

[32] Y. Chapuis, Ph.D. Thesis, Université Joseph Fourier, (2009); Y. Chapuis, A. Yaouanc, P. Dalmas de Réotier, C. Marin, S. Vanishri, S. H. Curnoe, C. Vâju, and A. Forget, Phys. Rev. B **82**, 100402(R) (2010).

[33] A. Yaouanc, P. Dalmas de Réotier, Y. Chapuis, C. Marin, S. Vanishri, D. Aoki, B. Fåk, L.-P. Regnault, C. Buisson, A. Amato, C. Baines, and A. D. Hillier, Physical Review B **84**, 184403 (2011).

[34] H. Takatsu, H. Kadowaki, T. J Sato2, Jeffrey W Lynn3, Yoshikazu Tabata4, Teruo

Yamazaki5 and Kazuyuki Matsuhira6, J. Phys.: Cond. Matt. **24**, 052201 (2011).

[35] T. Taniguchi, H. Kadowaki, H. Takatsu, B. Fåk, J. Ollivier, T. Yamazaki, T. J. Sato, H. Yoshizawa, Y. Shimura, T. Sakakibara, T. Hong, K. Goto, L. R. Yaraskavitch, and J. B. Kycia, Phys. Rev. B **87**, 060408(R) (2013).

[36] T. Fennell, M. Kenzelmann, B. Roessli, H. Mutka, J. Ollivier, M. Ruminy, U. Stuhr, O. Zaharko, L. Bovo, A. Cervellino, M. K. Haas, and R. J. Cava, Phys. Rev. Lett. **112**, 017203 (2014).

[37] K. Fritsch, E. Kermarrec, K. A. Ross, Y. Qiu, J. R. D. Copley, D. Pomaranski, J. B. Kycia, H. A. Dabkowska, and B. D. Gaulin, Phys. Rev. B **90**, 014429 (2014).

[38] K.B. Helean, S.V. Ushakov, C.E. Brown, A. Navrotsky, J. Lian, R.C. Ewing, J.M. Farmer, and L.A. Boatner, J. Solid State Chem. **177**, 1858 (2004).

[39] J. Zhang, K. Fritsch, Z. Hao, B. V. Bagheri, M. J. P. Gingras, G. E. Granroth, P. Jiramongkolchai, R. J. Cava, and B. D. Gaulin, Phys. Rev B **89**, 134410 (2014).

[40] A. P. Sazonov, A. Gukasov, H. B. Cao, P. Bonville, E. Ressouche, C. Decorse, and I. Mirebeau, Phys. Rev. B **88**, 184428 (2013).

[41] Z. Hiroi, K. Matsuhira, S. Takagi, T. Tayama, T. Sakakibara, J. Phys. Soc. Jpn. **72**, 411 (2003).

[42] I. Mirebeau, A. Apetrei, J. Rodriguez-Carvajal, P. Bonville, A. Forget, D. Colson, V. Glazkov, J. P. Sanchez, O. Isnard, and E. Suard, Phys. Rev. Lett. **94**, 246402 (2005).

[43] F. W. Sheard, AIP Conf. Proc. **3**, 155 (1972); M. T. Hutchings, Solid state Physics, F. Seitz and D. Turnbull Eds., Academic Press, New York, **16**, 227 (1964).

[44] B. D. Gaulin, J. S. Gardner, P. A. McClarty, and M. J. P. Gingras, Phys. Rev. B **84**, 140402(R) (2011)

[45] L. Balents, Nature **464**, 199 (2010).

[46] H. D. Zhou, C. R. Wiebe, J. A. Janik, L. Balicas, Y. J. Yo, Y. Qiu, J. R. D. Copley, and J. S. Gardner, Phys. Rev. Lett. **101**, 227204 (2008).

[47] L. Zhu, M. Garst, A. Rosch, and Q. Si, Phys. Rev. Lett. **91**, 066404 (2003).

Chapter 7

Thermal expansion behavior in spin ice state of $Dy_2Ti_2O_7$ and $Ho_2Ti_2O_7$

7.1 INTRODUCTION

In $Dy_2Ti_2O_7$ and $Ho_2Ti_2O_7$, the strong crystal-field anisotropy makes the rare-earth ion an Ising spin. Because the local Ising spins align with the cubic <111> direction, the spins on the pyrochlore lattice can only point in or out of each tetrahedron. The effective interaction resulted from the balance between the nearest-neighbor exchange interaction and dipole-dipole interaction is weak ferromagnetic, indicating a small positive Curie-Weiss temperature Θ_{CW} ~ 0.5 K and 1.9 K for $Dy_2Ti_2O_7$ and $Ho_2Ti_2O_7$, respectively [1]. In the case of antiferromagnetic Ising spins on a pyrochlore lattice, the ground state will form the "all-in all-out" structure. In contrast, ferromagnetic ones induce highly frustrated ground states with "two-in two-out" spin configuration on each tetrahedron. Because the situation reminds us of the proton positions in water ice, as can be seen in Fig. 7.1, the spin state in $Dy_2Ti_2O_7$ and $Ho_2Ti_2O_7$ are called as "spin ice" state. In addition, both compounds show a zero-point entropy $1/2R\ln(3/2)$ [1, 2, 3, 4], which is consistent with Pauling's entropy of water ice.

In this study, the thermal expansion behavior in the spin ice state of pyrochlore titanates, $Dy_2Ti_2O_7$ and Ho_2Ti_2O, investigated by heat capacity and thermal expansion measurements. Less attention has been paid on the lattice behavior of $Dy_2Ti_2O_7$ and $Ho_2Ti_2O_7$. It is speculated that the lattice will show an anomalous behavior in response

to the spin ice state. $Dy_2Ti_2O_7$ and $Ho_2Ti_2O_7$ exhibit an anomalous thermal expansion corresponding to the formation of the spin ice state.

7.1 EXPERIMENTAL

Single crystals of $Dy_2Ti_2O_7$ and $Ho_2Ti_2O_7$, which were from the same batch as in Ref. [5], were grown by a flux method with PbO, PbO_2, PbF_2, and MoO_3 as the flux. Single crystal of non-magnetic $Lu_2Ti_2O_7$ was also prepared by the same method. The sample of $Lu_2Ti_2O_7$ is used to estimate the lattice contribution without magnetic interaction to the heat capacity and thermal expansion coefficient. The obtained single crystals were translucent brown with octahedral shapes, and their crystal structures were confirmed by powder x-ray diffraction within the space group *Fd*-3*m*.

Heat capacity was measured by the relaxation technique with a Quantum Design PPMS down to 2 K. Thermal expansion measurements were carried out with a high-resolution capacitance dilatometer made of silver [6, 7]. The measurements were performed on the cubic <111> axis with the length of 1.71 mm, and 1.73 mm for $Dy_2Ti_2O_7$, and $Ho_2Ti_2O_7$, respectively.

7.3 RESULTS AND DISCUSSION

7.3.1 Heat capacity

The C_p of $Dy_2Ti_2O_7$ and $Ho_2Ti_2O_7$ is shown in Fig. 7.2, which are in good agreement with the previous studies [1, 4]. Ho ion has a large nuclear moment (I=7/2), and hence a nuclear hyperfine effect becomes considerable below 10 K. Employing the same manner in Ref. [1], the nuclear Schottky contribution from a splitting of the eight

nuclear levels with a level spacing of 0.3 K was estimated. The measured C_p of $Ho_2Ti_2O_7$ and estimated nuclear Schottky heat capacity C_{nuc} of Ho are shown in the inset of Fig. 7.2. The heat capacity subtracted the C_{nuc} from the C_p of $Ho_2Ti_2O_7$ is plotted in the main part of Fig. 7.2, and it exhibits the similar behavior with $Dy_2Ti_2O_7$.

7.3.2 Thermal expansion

Figure 7.3 presents the α of $Dy_2Ti_2O_7$ and $Ho_2Ti_2O_7$. With decreasing temperature, both of the α decreases without any anomaly down to 10 K. It is pointed out that our dilatometer with the high relative resolution $\Delta l/l \sim 10^{-10}$ could not find any evidence of a local distortion around 80 K, which is considered to give rise to the anomaly in the temperature dependencies of the elastic constants [8], permittivities [9], and Raman spectra [10]. The anomalous behavior of the α was found for both compounds below 10 K. Interestingly, they exhibited the opposite thermal expansion; the α of $Dy_2Ti_2O_7$ is negative, while that of $Ho_2Ti_2O_7$ is positive.

7.3.3 Magnetic contributions for C_p and α

In order to extract the magnetic contribution from the C_p, the normal lattice contribution was estimated by the temperature scaling of the C_p of non-magnetic reference compound $Lu_2Ti_2O_7$ (black solid and red dashed line in Fig. 7.2 for $Dy_2Ti_2O_7$ and $Ho_2Ti_2O_7$, respectively). The subtraction of the lattice heat capacity gives the magnetic heat capacity C_m shown in Fig. 7.4(a). In the same manner, the magnetic thermal expansion coefficient α_m was estimated from the subtraction of the lattice contribution obtained from scaling the α of $Lu_2Ti_2O_7$, which is presented in Fig. 7.4(b).

Both compounds showed similar behavior except the opposite sign in the α_m. The broad upturn of the C_m is resulted from the formation of the spin ice state, which has been evidenced from that the magnetic entropy obtained by integrating C_m/T shows a missing entropy close to Pauling's prediction for water ice [4]. On the other hand, the α_m appeared at a lower temperature than the C_m. Near the onset temperature of the α_m, the magnetic correlation length develops [11], and the spin-relaxation time slows down, i.e., spin freezing [12, 13]. Thus, the α_m is probably induced by the spin ice correlation. Similar temperature dependence can be seen in the magnetic thermal conductivity [14]. Although the anomalous thermal conductivity was attributed to the dynamics of magnetic monopole, our results suggest the need to account a contribution from the lattice dynamics originated from the magnetic excitation. It should be noted that the time scale of our thermal expansion measurements (heating rate: 0.3 K/min) is arguably enough to capture this slow dynamics (at 2 K, $\tau \sim 10^{-3}$ s for $Dy_2Ti_2O_7$ [12], and 10^{-8} s for $Ho_2Ti_2O_7$ [13], respectively).

7.3.4 Lattice behavior in spin ice state

In $Dy_2Ti_2O_7$ and $Ho_2Ti_2O_7$, the low-temperature magnetic properties stem from the nearest neighbor exchange interaction J_{nn} and dipole-dipole interaction D_{nn}. The dipolar spin ice model proposed by den Hertog and Gingras [15] indicates that the magnetic state depends on the ratio of the nearest-neighbor exchange and dipole-dipole interactions, J_{nn}/D_{nn}, where the spin-ice phase appears for $J_{nn}/D_{nn} > -0.91$, while the antiferromagnetic phase with all-in/all-out spin configuration emerges for $J_{nn}/D_{nn} < -0.91$. Based on this theory, the heat capacity peak height and temperature at which it occurs provide J_{nn}/D_{nn} as -0.53 for $Dy_2Ti_2O_7$ [15], and $Ho_2Ti_2O_7$ [1], respectively.

Hence, the phase stability of spin-ice state in $Dy_2Ti_2O_7$ is lower than in $Ho_2Ti_2O_7$. This difference in the strength of the exchange interactions is considered to be a reason for the different thermal expansion. As opposed to $Tb_2Ti_2O_7$, the crystal field effect is negligible at low temperature because of the large separation between the ground and lowest excited crystal field state with the energy separation of about 380 K for $Dy_2Ti_2O_7$ and ~230 K for $Ho_2Ti_2O_7$ [16].

Further insight can be obtained from the study of chemical pressure effects on the magnetic properties through the substitution of the *B*-site Ti^{4+} ion with Ge^{4+} ion, as shown in Fig. 7.5 [17]. $Dy_2Ge_2O_7$ and $Ho_2Ge_2O_7$ with pyrochlore structure also show the spin-ice state at low temperature. Due to the smaller ionic radius of Ge^{4+} ion than Ti^{4+} ion, both $Dy_2Ge_2O_7$ and $Ho_2Ge_2O_7$ have the contracted lattice constant compared with $Dy_2Ti_2O_7$ and $Ho_2Ti_2O_7$. The dipole-dipole interaction in the pyrochlore lattice is inversely proportional to the cube of the distance between the nearest neighbor magnetic ions, while the exchange interaction is generally more sensitive to the distance change. Indeed, $Dy_2Ge_2O_7$ and $Ho_2Ge_2O_7$ exhibit the larger negative J_{nn}/D_{nn} than $Dy_2Ti_2O_7$ and $Ho_2Ti_2O_7$, meaning that the ratio J_{nn}/D_{nn} approaches to the phase boundary between spin ice and antiferromagnetic phases. It suggests that the lattice contraction with decreasing temperature destabilizes the spin ice state. Thus, negative thermal expansion may be able to stabilize a spin ice state by weakening the exchange interaction.

The pressure dependence of the magnetic energy scale of the spin ice state $\partial \ln E_m / \partial p$ can also lead to useful information for the phase stability, which is evaluated from the following equation:

$$\frac{\alpha(T)}{C(T)} = \frac{1}{3V_m}\frac{\partial \ln E_{\mathrm{m}}}{\partial p},$$

where V_m denotes the molar volume, E_{m} is the energy for a relevant system, and the C_{m}

and α_m were used for $\alpha(T)$ and $C(T)$, respectively. Here E_m is considered to correspond to J_{nn}/D_{nn}. With decreasing temperature, the value $\partial \ln E_m / \partial p$ for $Dy_2Ti_2O_7$ and $Ho_2Ti_2O_7$ gradually increases with the opposite sign as shown in Fig. 7.4(c). At 2 K, their values reach to -0.034/GPa and 0.009/GPa for $Dy_2Ti_2O_7$ and $Ho_2Ti_2O_7$, respectively. The negative value of $\partial \ln E_m / \partial p$ means that J_{nn}/D_{nn} will shift to negative side by applying pressure. This effect is consistent with the change in J_{nn}/D_{nn} from $Dy_2Ti_2O_7$ to $Dy_2Ge_2O_7$, which is equivalent to applying a pressure to $Dy_2Ti_2O_7$. However, $Ho_2Ti_2O_7$ shows a small but positive value of $\partial \ln E_m / \partial p$, as opposed to the decrease in J_{nn}/D_{nn} from $Ho_2Ti_2O_7$ to $Ho_2Ge_2O_7$. The absolute value of $\partial \ln E_m / \partial p$ for $Ho_2Ti_2O_7$ is rather small than that for $Dy_2Ti_2O_7$. Because the peak temperature of the heat capacity due to the formation of the spin ice state is rather close to 2 K in $Ho_2Ti_2O_7$ than in $Dy_2Ti_2O_7$, $Ho_2Ti_2O_7$ is expected to possess stronger coupling between spin and lattice degrees of freedom at 2 K, resulting in higher $\partial \ln E_m / \partial p$. Hence, there might be some kind of contribution for the thermal expansion coefficient.

Then, two possibilities could be proposed for the absence of negative thermal expansion in $Ho_2Ti_2O_7$. The first hypothesis is that the nuclear hyperfine effect obscures a negative thermal expansion. A nuclear contribution to the thermal expansion has been reported for some rear-earth compounds [18, 19, 20]. Hirschkoff and Wolcott [21] suggested that the nuclear thermal expansion can be emerged at low temperature as in the heat capacity. They estimated the nuclear contribution for the thermal expansion coefficient of holmium metal, $\alpha_{nuc} \sim 0.6 \times 10^{-6}$ K^{-1} at 2 K. The nuclear hyperfine coupling constant of holmium metal a'~0.3 K is nearly equal to with that of $Ho_2Ti_2O_7$, and hence the α of $Ho_2Ti_2O_7$ would include the α_{nuc} with a similar magnitude to holmium metal. If negative contribution to the thermal expansion is induced by the spin

ice state in $Ho_2Ti_2O_7$ and its magnitude is comparable with that of $Dy_2Ti_2O_7$, the α_{nuc} can exceed the negative thermal expansion, providing the positive thermal expansion.

Another possibility is that the lattice contraction has an opposite effect on the internal energy of each compound. The chemical substitution study found out the non-linear effect of the chemical pressure on J_{nn}/D_{nn}, as shown in Fig. 7.5 [17]. In the Dy systems, the substitution of the Ti^{4+} ions with the Ge^{4+} ions increases by 82% and 15% in J_{nn} and D_{nn}, respectively. Meanwhile, in the Ho systems, the same substitution increases by 55% and 15% in J_{nn} and D_{nn}, respectively. This result suggests that the variation of J_{nn} with the volume contraction is grater in $Dy_2Ti_2O_7$ than in $Ho_2Ti_2O_7$. In addition, the J_{nn} of $Dy_2Ti_2O_7$ is more than double for that of $Ho_2Ti_2O_7$. Thus, at low temperature $Dy_2Ti_2O_7$ is rather unstable than $Ho_2Ti_2O_7$. On the other hand, the system has to pay the elastic energy to distort the lattice. This cost is expected to be nearly identical in $Dy_2Ti_2O_7$ and $Ho_2Ti_2O_7$ because the difference in the type of the rare-earth ion leads to subtle influence on the lattice energy. For these reasons, the opposite thermal expansion might be resulted from the balance between the energy gain by weakening the exchange interaction and the elastic energy cost to contract the lattice. Hence, $Dy_2Ti_2O_7$ lower the internal energy by expanding the lattice to avoid strengthening J_{nn}, while $Ho_2Ti_2O_7$ by contracting the lattice due to the insensitivity of J_{nn}. This scenario would be verified by performing thermal expansion measurements on *B*-site substituted systems. Further investigations on this property in spin ice material need to reveal its mechanism. The emergence of negative thermal expansion is reminiscent of the thermal expansion of water just before freezing. Although the different mechanism induces negative thermal expansion, the comparison of two materials might provide an unexpected aspect of “ice state” in spin ice material.

7.4 CONCLUSION

This chapter studied the lattice behavior in the spin ice compounds, $Dy_2Ti_2O_7$ and $Ho_2Ti_2O_7$. Both compounds exhibited the anomalous behavior in both the heat capacity and thermal expansion, which are associated with a spin ice state. While the magnetic heat capacity was observed below 15 K, the magnetic thermal expansion coefficients were appeared below 5 K, indicating the correlation between the lattice degrees of freedom and the development of static spin ice state. The discussion of the stability of spin ice system suggests that negative thermal expansion could be common behavior in spin ice state. The positive thermal expansion at low temperature in $Ho_2Ti_2O_7$ may be due to a large nuclear hyperfine effect of the Ho ion, or the difference of the required energy to expand the lattice between $Ho_2Ti_2O_7$ and $Dy_2Ti_2O_7$.

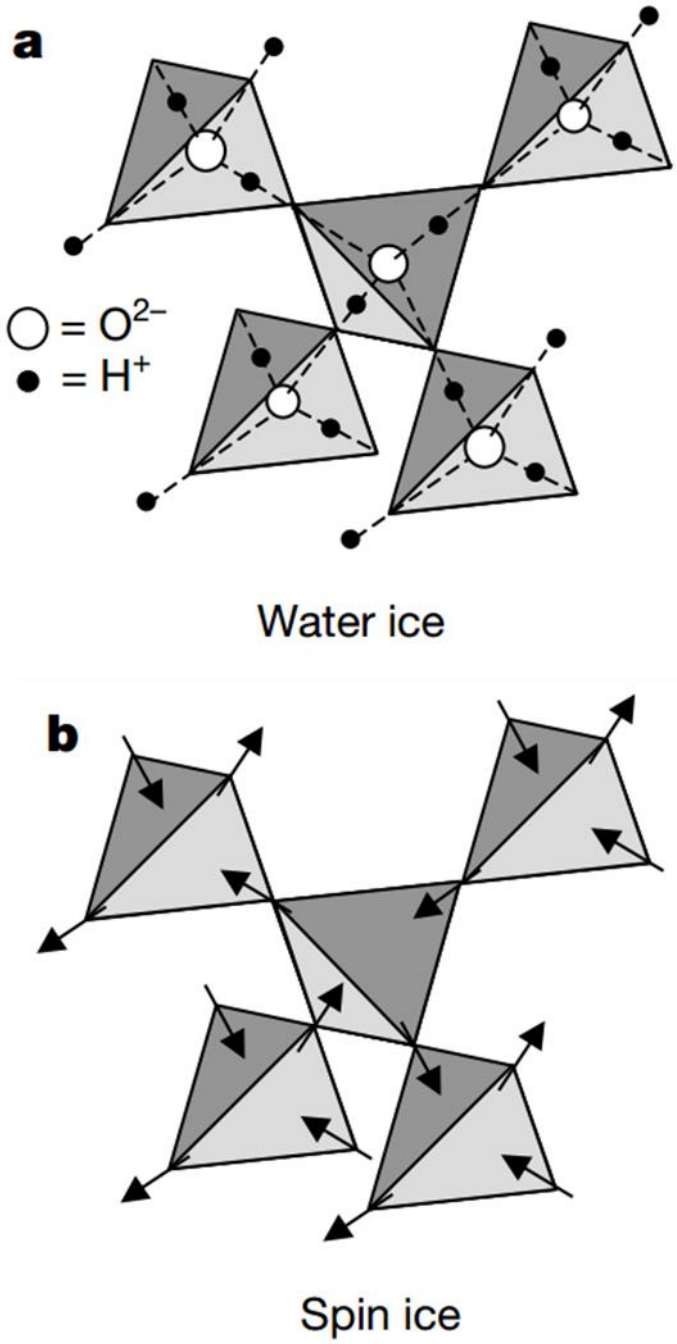

Fig. 7.1. The ordered configuration of (a) water ice and (b) spin ice. From [12].

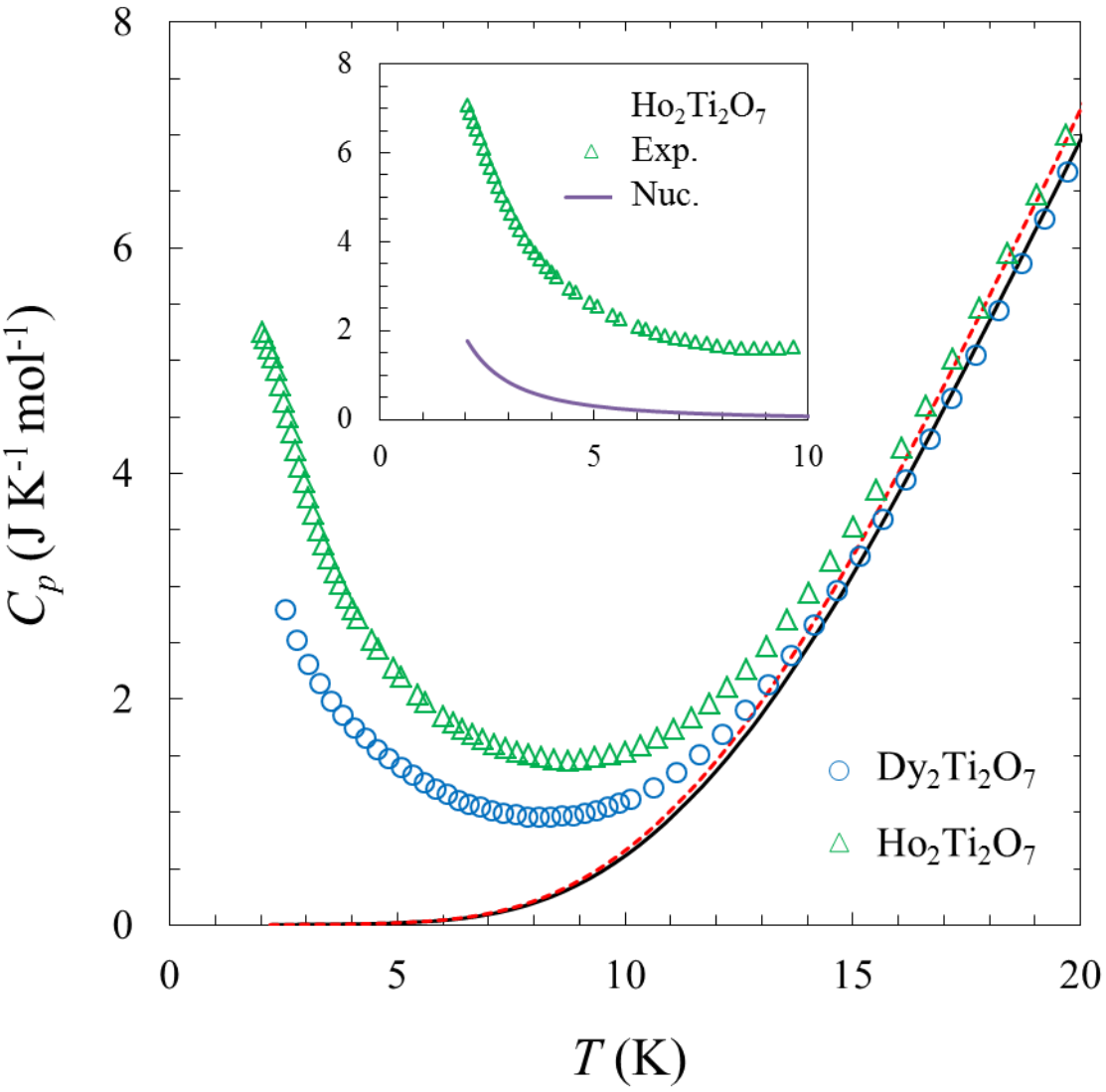

Fig. 7.2. Heat capacity of $Dy_2Ti_2O_7$ (Blue circles) and $Ho_2Ti_2O_7$ (Green triangles). The C_p of $Ho_2Ti_2O_7$ has been subtracted the nuclear hyperfine contribution from the experimental data. The solid black line and dashed red line show the lattice heat capacity estimated by scaling the C_p of $Lu_2Ti_2O_7$. The inset displays the measured heat capacity data (Green triangles) and the nuclear Schottky heat capacity, assuming a splitting of the eight nuclear levels with a level spacing of 0.3 K.

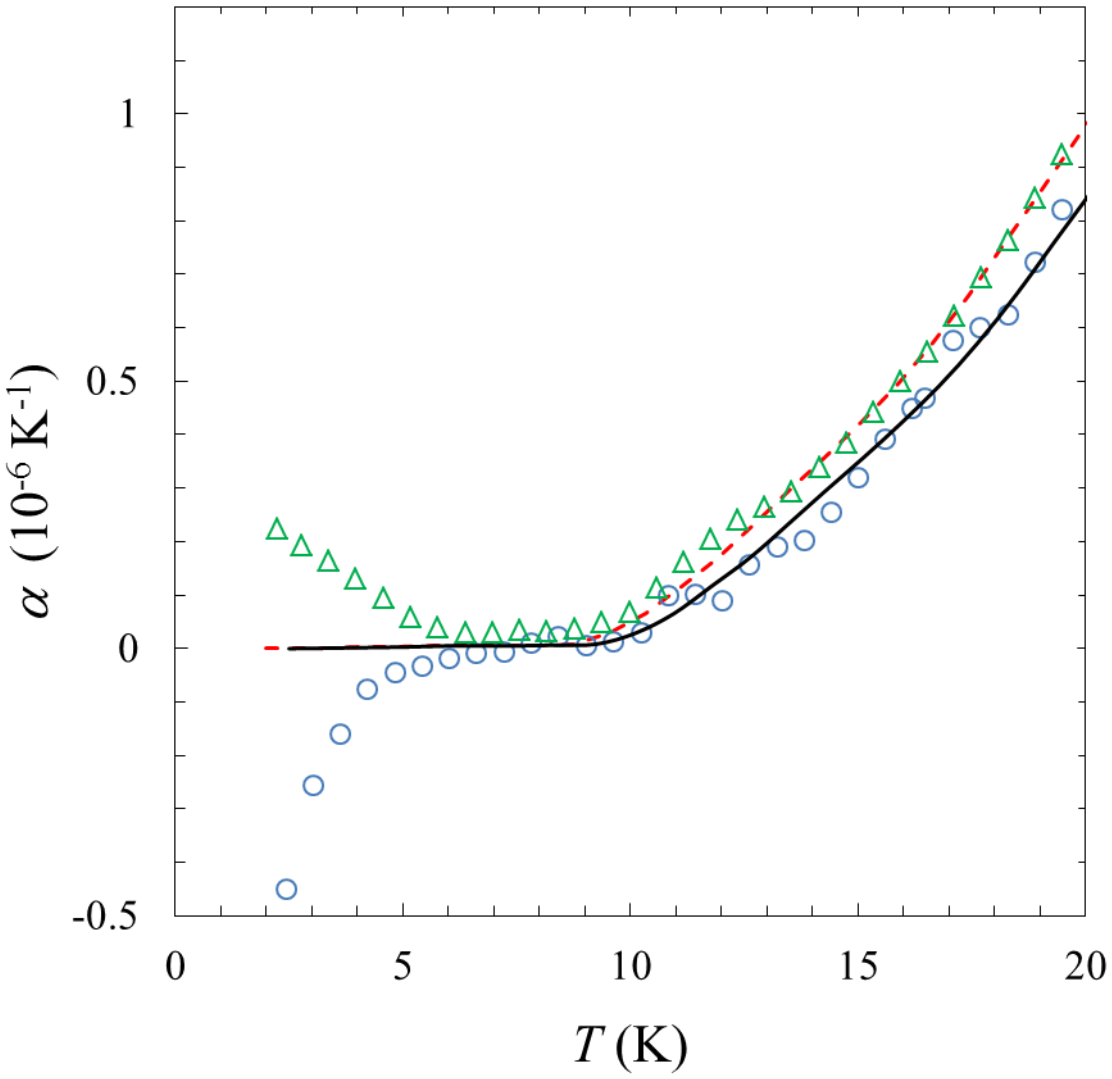

Fig. 7.3. Thermal expansion coefficient α of $Dy_2Ti_2O_7$ and $Ho_2Ti_2O_7$. The solid black line and dashed red line show the lattice heat capacity estimated by scaling the α of $Lu_2Ti_2O_7$.

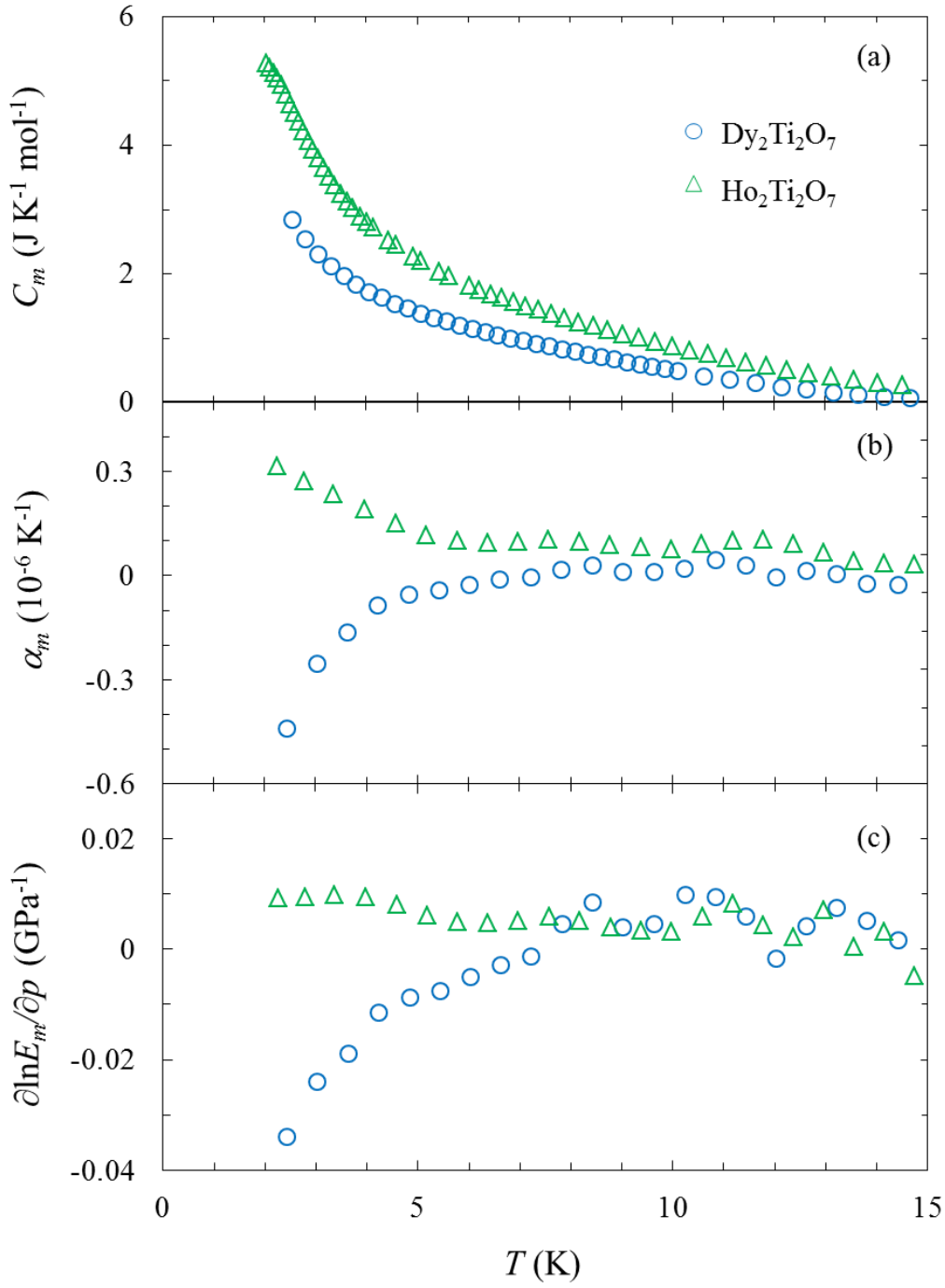

Fig. 7.4. (a) Magnetic heat capacity C_m. (b) Thermal expansion coefficient α_m. They are obtained from the subtraction of the lattice contribution from the experimental data. (c) The pressure dependence of the magnetic energy scale of the spin ice state $\partial \ln E_m / \partial p$ evaluated from Eq. (4) using the C_m and α_m.

Table 7.1. Lattice parameters and selected magnetic parameters for all six pyrochlore spin ices. From [17].

	a (Å)	θ_{CW} (K)	D_{nn} (K)	C_{peak} ($J/mol_{Ho,Dy} \cdot K$)	T_{peak} (K)	J_{nn}/D_{nn} (K)	J_{eff}
$Ho_2Sn_2O_7$	10.37	1.8	2.17	2.41	1.65	−0.26	1.61
$Ho_2Ti_2O_7$	10.10	1.9	2.35	2.61	1.75	−0.27	1.72
$Ho_2Ge_2O_7$	9.90	0.06	2.50	3.04	1.70	−0.35	1.63
$Dy_2Sn_2O_7$	10.40	1.7	2.15	2.65	1.20	−0.46	1.16
$Dy_2Ti_2O_7$	10.10	0.5	2.35	2.72	1.25	−0.49	1.20
$Dy_2Ge_2O_7$	9.93	0.0	2.47	3.17	0.828	−0.73	0.67

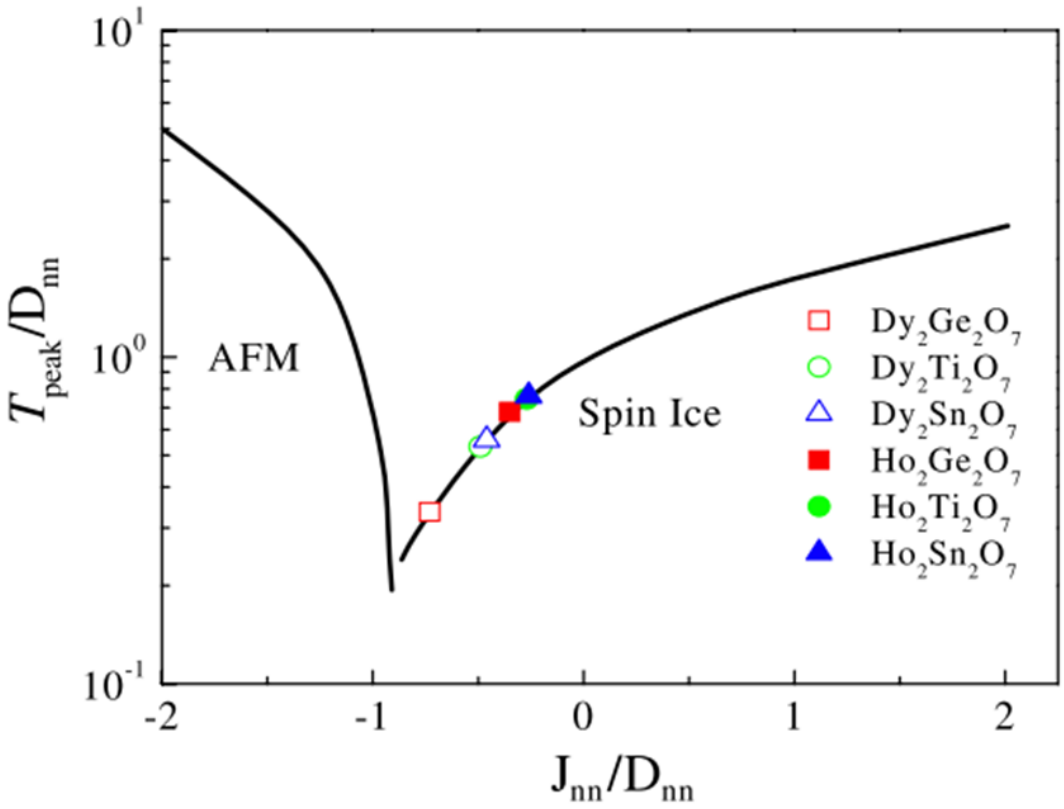

Fig. 7.5. Dependencies of the specific heat peak position T_{peak}/D_{nn} on J_{nn}/D_{nn} ratio. The symbols are experimental results, and the solid lines are the theoretical calculations from the dipolar spin ice model. From [15, 17].

References

[1] S. T. Bramwell and M. J. P. Gingras, Science **294**, 1495 (2001).

[2] M. J. Harris, S. T. Bramwell, D. F. McMorrow, T. Zeiske, and K. W. Godfrey, Phys. Rev. Lett. **79**, 2554 (1997).

[3] M. J. Harris, S. T. Bramwell, T. Zeiske, D. F. McMorrow, and P. J. C. King, J. Magn. Magn. Mater. **177**, 757 (1998).

[4] A. P. Ramirez, A. Hayashi, R. J. Cava, R. Siddharthan, and B. S. Shastry, Nature **399**, 333 (1999).

[5] M. Tachibana, Solid State Commun. **174**, 16 (2013).

[6] M. Rotter, H. Müller, E. Gratz, M. Doerr, and M. Loewenhaupt, Rev. Sci. Instrum. 69, 2742 (1998).

[7] S. Kitani, M. Tachibana, N. Taira, and H. Kawaji, Phys. Rev. B **87**, 064402 (2013).

[8] L. G. Mamsurova, K. S. Pigal'skiĭ, N. G. Trusevich, and L. G. Shcherbakova, Sov. Phys. Solid State **27**, 978 (1985).

[9] T. T. A. Lummen, I. P. Handayani, M. C. Donker, D. Fausti, G. Dhalenne, P. Berthet, A. Revcolevschi, and P. H. M. van Loosdrecht, Phys. Rev. B **77**, 214310 (2008).

[10] T. Fennell, P. P. Deen, A. R. Wildes, K. Schmalzl, D. Prabhakaran, A. T. Boothroyd, R. J. Aldus, D. F. McMorrow, S. T. Bramwell, Science **326**, 415 (2009).

[11] J. Snyder, B. G. Ueland, J. S. Slusky, H. Karunadasa, R. J. Cava, and P. Schiffer, Phys. Rev. B **69**, 064414 (2004).

[12] J. P. Clancy, J. P. C. Ruff, S. R. Dunsiger, Y. Zhao, H. A. Dabkowska, J. S. Gardner, Y. Qiu, J. R. D. Copley, T. Jenkins, and B. D. Gaulin, Phys. Rev. B **79**, 014408 (2009).

[13] G. Kolland, O. Breunig, M. Valldor, M. Hiertz, J. Frielingsdorf, and T. Lorenz, Phys. Rev. B **86**, 060402(R) (2012).

[14] B. C. den Hertog and M. J. P. Gingras, Phys. Rev. Lett. **84**, 3430 (2000).

[15] S. Rosenkranz, A. P. Ramirez, A. Hayashi, R. J. Cava, R. Siddharthan, and B. S. Shastry, J. Appl. Phys. **87**, 5914 (2000).

[16] H. D. Zhou, J. G. Cheng, A. M. Hallas, C. R. Wiebe, G. Li, L. Balicas, J. S. Zhou, J. B. Goodenough, J. S. Gardner, and E. S. Choi, Phys. Rev. Lett. **108**, 207206 (2012).

[17] R. Gonano and E. D. Adams, Bull. Am. Phys, Soc. **13**, 667 (1968)

[18] H. R. Ott, Solid State Commun. **16**, 1355 (1975).

[19] N. Oeschler, P. Gegenwart, F. Weickert, I. Zerec, P. Thalmeier, F. Steglich, E. D. Bauer, N. A. Frederick, and M. B. Maple, Phys. Rev. B **69**, 235018 (2004).

[20] E. C. Hirschkoff and N. M. Wolcott, Proc. Phys. Soc. **86**, 1372 (1965).

Chapter 8

Summary and Conclusion

The concept of “frustration” has been attracted much attention as the playground for novel physical properties. In most cases, the resulting macroscopic degeneracy will be lifted by coupling to other degrees of freedom, leaving peculiar behaviors. In the case of magnetically frustrated materials, as discussed in Chapter 1, the spin degrees of freedom often couple to the lattice degrees of freedom, *i.e.*, spin-lattice coupling. In this doctoral thesis, the spin-lattice effects in systems with the pyrochlore lattice have been investigated by thermodynamic measurements, as introduced in Chapter 2. Their exciting properties have been discussed from the thermodynamic point of view.

Chapter 3. Spin-glass-like behavior in ferromagnetic phase of $CdCr_2S_4$

Spin-glass-like behaviors in the ferromagnetic phase of $CdCr_2S_4$ have investigated. Although the term “ferromagnetic” seems to be out of place in the context of frustration, $CdCr_2S_4$ has exhibited anomalous behaviors, which is not expected for a typical Heisenberg ferromagnet. The anomalous behaviors in the low-temperature heat capacity suggest that a glassy state grows below 20 K, coexisting with the ferromagnetic state. Thermal expansion measurements have shown negative thermal expansion below 100 K, which indicates the presence of the magnetic frustration resulted from the local lattice distortion. Both the *dc* and *ac* susceptibility measurements have exhibited the glass-like behavior. Assuming the presence of a local lattice distortion, arising from a second Jahn-Teller effect, these results have thus been concluded as follows; First, the

short-range magnetic clusters is formed due to the local anisotropic interaction, and it performs as a nanoparticle. With decreasing temperature, some clusters will be trapped into a metastable state. The trapped clusters work as nucleus for nucleation. Finally the clusters will gather and form larger spin clusters below 20 K. The spin configuration of this anomalous ferromagnetic state should be clarified in future. As can be expected from the present results, the search for the low-temperature spin structure will be the central issue for the future works, which might be achieved by the apparatus that can detect mesoscopic scale of about hundreds of nanometer, such as small-angle neutron scattering.

Chapter 4. Spin-lattice coupling effect in strongly geometrically frustrated spinel $CdCr_2O_4$

The spin-lattice coupling in strongly geometrically frustrated spinel $CdCr_2O_4$ has studied. Strong frustration due to Cr^{3+} ions forming the pyrochlore network is known to be relieved by distorting the lattice, and hence the spin-lattice coupling should play an important role in $CdCr_2O_4$. The magnetic susceptibility and heat capacity evidenced that the magnetic interaction is effective below 150 K. The thermal expansion behavior was impressive; it exhibited negative thermal expansion below 150 K, and returned to positive thermal expansion below 45 K without a phase transition. This peculiar behavior was attributed to the competition of the effect between the magnetic frustration and the antiferromagnetic hexagonal spin cluster in the paramagnetic regime. This idea further provided the important clue for the formation of that spin cluster. The heat capacity and thermal expansion data derived the pressure dependence of the

magnetostructural transition temperature. The obtained value contradicted to the previous report, though the difference must not be an experimental error. The contracted results might be resulted from the presence or absence of magnetic field. The comparison of the family compound $ZnCr_2O_4$, which shows a helpful response to pressure and magnetic field, was instructive. Future works need to deal with the detailed pressure and magnetic field dependence of the magnetostructural transition temperature, which might give an important insight on the different structural distortion of $CdCr_2O_4$ and $ZnCr_2O_4$ at the transition. Thermal expansion measurements on $ZnCr_2O_4$ and also $HgCr_2O_4$, which have a weaker antiferromagnetic interaction than $CdCr_2O_4$, are also considered to be important. Because they have the different strength of not only the frustration but also the spin-lattice coupling, thermal expansion behavior will be much different from $CdCr_2O_4$.

Chapter 5. Lattice behavior in the conical spin state of $CoCr_2O_4$

This chapter has focused on the lattice behavior in the conical spin state of the spinel $CoCr_2O_4$. Due to the magnetic Co^{2+} ions in the *A*-site, this compound shows highly complex magnetic orderings. Although $CoCr_2O_4$ has been known to show the strong sample dependent due to the site mixing, the present sample was very pure because each ferrimagnetic, conical spin, lock-in transitions were clearly observed, and the heat capacity at the conical spin transition was significantly sharp. At the conical spin transition, the thermal expansion coefficient was broadened above 20 K higher than the transition temperature, indicating the growth of the short-range ordering. The interesting behavior of the thermal expansion has been observed at the lock-in transition, where the heat capacity peak was very small, while the thermal expansion coefficient

showed the large peak, as opposed to the conical spin transition. The pressure dependence of the transition temperatures calculated from these results led to the intriguing insights. Especially, the considerable pressure dependence of the lock-in transition temperature proposed the possibility of the symmetry reduction from the cubic at the lock-in transition. From the magnetocaloric effect measurements under the pulse magnetic field, the precise *H-T* phase diagram was presented for the <111> and <001> axis. There was a first-order phase transition with huge latent heat at high field, which transition temperature apparently depends on the field direction. As for future works, the crystal orientation dependence of the thermal expansion should be performed to certify the anisotropic lattice distortion at the lock-in transition. To know what happened at the high field phase transition in more detail, it is interested to conduct other experiments under pulsed magnetic field. Heat capacity measurement inevitably has to be carried out to get the information on the entropy of the high field phase. Other promising measurements are the capacitive and thermal expansion measurement; the former will show a sudden drop of the capacitance at the phase transition due to the collapse of the conical spin state, and the latter will confirm the lattice reconstruction to the cubic phase due to lacking the inverse DM interaction.

Chapter 6. Lack of the spin-lattice coupling in spin liquid state of $Tb_2Ti_2O_7$

The effect of the spin-lattice coupling in the spin-liquid compound $Tb_2Ti_2O_7$ has been studied. It has been a long-standing problem in $Tb_2Ti_2O_7$ why it shows the spin-liquid behavior, and what stabilize the spin-liquid state? The spin-lattice coupling has been considered to be one of the key factors for those issues, because anomalous temperature dependences have been found in several lattice properties. The present

study has performed heat capacity and thermal expansion measurements. The heat capacity showed two shoulders at around 8 K and 2 K. With applying magnetic field, the 2 K anomaly was enhanced up to 1 T without large suppression in the heat capacity below 2 K. Although at 1 T, the 3-in, 1-out / 1-in, 3-out spin structure is formed, the magnetic entropy did not show a large change expected for the unique spin state. Thus, the puzzling correlation providing the 2 K anomaly in the ground state at zero field might be rearranged by magnetic field without losing the entropy. Thermal expansion coefficient exhibited only one shoulder-like anomaly around 8 K, as opposed to the heat capacity. This behavior was well reproduced by the lattice contribution and the Schottky anomaly, resulted from the presence of low-lying first excited CEF doublet with the separated energy of 18 K. No anomalous behavior below 7 K indicates the absence of a spin-lattice effect, and the spin-lattice coupling is not need to establish a non-ordered ground state. The combination of our heat capacity and thermal expansion data provided the pure component for the heat capacity anomaly below 7 K. The excess heat capacity led to the excess entropy S_{ex}~7.5 J/Kmol, which is rather small compared to the expected entropy for the ground CEF doublet splitting $S=2R\ln(2)=11.5$ J/Kmol. The large shortfall in entropy indicates the strong fluctuation in the ground state, and possibly relates with a realization of a quantum spin ice state. Future works for the spin liquid state in $Tb_2Ti_2O_7$ need to explain the present results. For the confirmation of the lack of negative thermal expansion, the crystal orientation dependence of the thermal expansion should be confirmed.

Chapter 7. Thermal expansion behavior in spin ice state of $Dy_2Ti_2O_7$ and $Ho_2Ti_2O_7$

This chapter dealt with the lattice behavior of the spin ice compound $Dy_2Ti_2O_7$ and

$Ho_2Ti_2O_7$. They are known to show the "two-in two-out" spin structure, which is reminiscent of the proton positions in water ice. $Dy_2Ti_2O_7$ and $Ho_2Ti_2O_7$ exhibited the anomalous behavior in both the heat capacity and thermal expansion, which are associated with a spin ice state. The interesting findings were negative thermal expansion below 5 K in $Dy_2Ti_2O_7$. The discussion of the stability of spin ice system suggests that negative thermal expansion could be common behavior in spin ice state. However, $Ho_2Ti_2O_7$ exhibited the positive thermal expansion below 5 K, which may be due to a large nuclear hyperfine effect of the Ho ion, or the difference of the required energy to expand the lattice between $Dy_2Ti_2O_7$ and $Ho_2Ti_2O_7$. To determine which ideas make sense, thermal expansion measurements on the other spin ice materials will need to be performed. In addition, it will be needed to make clear whether the nuclear thermal expansion due to ^{165}Ho nuclear spin is appeared or not.

As described above, the present thesis has studied on the frustrated spinel and pyrochlore systems with the spin-lattice coupling. It has demonstrated that the spin-lattice coupled systems exhibit the characteristic lattice behaviors corresponding to their spin behaviors. Furthermore, the combination of the thermodynamic studies provided valuable insights on the spin behavior and phase stability as well as the lattice property. I hope that the present results and suggestions become the cornerstone for developing a comprehensive mechanism of the novel properties in the materials studied in this thesis.

Appendix

List of published articles

1. Suguru Kitani, Makoto Tachibana, Naoya Taira, Hitoshi Kawaji, "*Thermal study of the interplay between spin and lattice in $CoCr_2O_4$ and $CdCr_2O_4$*", Phys. Rev. B **87**, 064402-1 – 064402-6 (2013).

   (Including in chapter 4 and 5)

2. Suguru Kitani, Makoto Tachibana, Hitoshi Kawaji, "*Spin-glass-like behavior in ferromagnetic phase of $CdCr_2S_4$*", Solid State Communications **179**, 16-19 (2014).

   (Including in chapter 3)

3. Suguru Kitani, Makoto Tachibana, Hitoshi Kawaji, "*Low-temperature lattice properties of frustrated pyrochlore magnets $R_2Ti_2O_7$ (R=Tb, Dy, and Ho)*", to be submitted to *Phys. Rev. B.*

   (Including in chapter 6 and 7)

Acknowledgements

This work had accomplished in Kawaji Laboratory, Materials and Structures Laboratory, Tokyo Institute of Technology, Japan, from the April 2010 to the December 2014. First of all, I especially thank Professor Hitoshi Kawaji for invaluable guidance and discussions during the course of this work. I wish to thank the late Professor Tooru Atake for many encouragements. I also want to thank the members of Kawaji Laboratory for their help and discussions, and I am indebted to my senior colleagues, Kyohei Mizushima and Naoya Taira, in this regard.

I have a special thanks to Dr. Makoto Tachibana for fruitful discussions, the dilatometer and the samples through all of this work. I would also like to thank Research Associate Yoshimitsu Kohama for useful advices on the low-temperature measurements and the pulsed magnetic field measurements in the research of $CoCr_2O_4$ (Chapter 5).

I also thank Professor Takeo Ohsaka, Ryoji Kanno, Nobuhiro Matsushita, and Masaaki Hirayama for their review of this thesis.

Finally, I would like to give my greatest appreciation to my family and relative. Without their understanding and support, I could never have completed this work.

December, 2014

Suguru Kitani